Error-Mitigated Quantum Routing on Noisy Intermediate-Scale Quantum Devices

Wenbo Shi

A thesis in fulfilment of the requirements for the degree of

Doctor of Philosophy

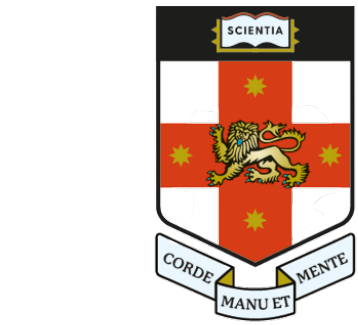

UNSW
SYDNEY

School of Electrical Engineering and Telecommunications

Faculty of Engineering

The University of New South Wales

November 2024

ORIGINALITY STATEMENT

☑ I hereby declare that this submission is my own work and to the best of my knowledge it contains no materials previously published or written by another person, or substantial proportions of material which have been accepted for the award of any other degree or diploma at UNSW or any other educational institution, except where due acknowledgement is made in the thesis. Any contribution made to the research by others, with whom I have worked at UNSW or elsewhere, is explicitly acknowledged in the thesis. I also declare that the intellectual content of this thesis is the product of my own work, except to the extent that assistance from others in the project's design and conception or in style, presentation and linguistic expression is acknowledged.

COPYRIGHT STATEMENT

AUTHENTICITY STATEMENT

☑ I certify that the Library deposit digital copy is a direct equivalent of the final officially approved version of my thesis.

UNSW is supportive of candidates publishing their research results during their candidature as detailed in the UNSW Thesis Examination Procedure.

Publications can be used in the candidate's thesis in lieu of a Chapter provided:

- The candidate contributed **greater than 50%** of the content in the publication and are the "primary author", i.e. they were responsible primarily for the planning, execution and preparation of the work for publication.
- The candidate has obtained approval to include the publication in their thesis in lieu of a Chapter from their Supervisor and Postgraduate Coordinator.
- The publication is not subject to any obligations or contractual agreements with a third party that would constrain its inclusion in the thesis.

☑ The candidate has declared that **some of the work described in their thesis has been published and has been documented in the relevant Chapters with acknowledgement**.

A short statement on where this work appears in the thesis and how this work is acknowledged within chapter/s:

> Chapter 3 is partially based on the following publication: W. Shi and R. Malaney, “Quantum Routing for Emerging Quantum Networks,” IEEE Network, vol. 38, no. 1, pp. 140-146, 2024, doi: 10.1109/MNET.2023.3317821.
>
> Chapter 4 is partially based on the following publication: W. Shi and R. Malaney, “Entanglement of Signal Paths via Noisy Superconducting Quantum Devices,” Entropy, vol. 25, no. 1, 153, 2023, doi: 10.3390/e25010153.
>
> Chapter 5 is partially based on the following publication: W. Shi and R. Malaney, “Error-Mitigated Quantum Routing on Noisy Devices,” in 2023 IEEE Global Communications Conference, 2023, pp. 5475-5480, doi: 10.1109/GLOBECOM54140.2023.10437807.
>
> Chapter 6 is partially based on the following publication: W. Shi, N. K. Kundu, and R. Malaney, “Error-Mitigated Multi-Layer Quantum Routing,” arXiv:2409.14632, 2024, doi: 10.48550/arXiv.2409.14632.
>
> Chapter 7 is partially based on the following publication: W. Shi, N. K. Kundu, M. R. McKay, and R. Malaney, “Error-Mitigated Quantum Random Access Memory,” arXiv:2403.06340, 2024, doi: 10.48550/arXiv.2403.06340.
>
> Appendix A is partially based on the following publication: W. Shi and R. Malaney, “Signal Processing and Quantum State Tomography on Noisy Devices,” in 2023 IEEE International Conference on Acoustics, Speech and Signal Processing (ICASSP), 2023, pp. 1-5, doi: 10.1109/ICASSP49357.2023.10094890.
>
> All of the above is documented in the Introduction chapter of my thesis.

Candidate's Declaration

I declare that I have complied with the Thesis Examination Procedure.

Abstract

This thesis investigates quantum error mitigation methods applied to quantum routing applications with state tomography on Noisy Intermediate-Scale Quantum (NISQ) devices, specifically superconducting quantum devices provided by IBM. Quantum routing is a process that directs a single quantum signal to be simultaneously present in a superposition of multiple output paths and will be a critical component of future quantum networks.

Before the investigation of quantum error mitigation, we first implement quantum error correction with the assumption of statistical knowledge on quantum communication channels and a five-qubit quantum error-correcting code, which permits corrections of generic single-qubit errors via encoding a one-qubit quantum signal to five qubits. Our experimental results demonstrate the limitations of quantum error correction and inspire the utilization of quantum error mitigation for current quantum devices.

We then explore multiple quantum error mitigation methods, including Zero-Noise Extrapolation (ZNE), Probabilistic Error Cancellation (PEC) and Clifford Data Regression (CDR). Beyond exploring the improved performance of quantum routing via ZNE and PEC separately, we also investigate the routing performance provided by the concatenation of these two error-mitigation methods. Such concatenation yields significant performance enhancements, paving the way for practical quantum routing. A new quantum error mitigation method, named extrapolated CDR (eCDR), that builds a conceptual bridge between ZNE and CDR, is proposed to mitigate errors for multi-layer quantum routers on NISQ devices. We also propose a variant of ZNE, which is applied to quantum random access memory, a key application of quantum routing.

Overall, this thesis contributes novel and important insights into the development and implementation of quantum error mitigation as applied to quantum routing, laying the foundation for the realization of near-term quantum communication networks.

Acknowledgement

First and foremost, I sincerely thank my supervisor, Prof. Robert Malaney, for his guidance, encouragement, and patience throughout my PhD journey, as well as for providing me with this cherished opportunity to participate in research on quantum communications and quantum computing. I am sincerely grateful to my secondary supervisor, Dr. Hendra Nurdin, who provided valuable feedback and support for my research.

I extend my gratitude to my collaborators, Dr. Neel Kanth Kundu and Prof. Matthew R. McKay, for sharing valuable quantum resources and offering academic advice and feedback. I am grateful to my lab fellows for answering my research questions and engaging in fruitful discussions: Dr. Ziqing Wang, Dr. Mingjian He, Dr. Xiaoyu Ai, Dr. Eduardo Villaseñor, Ronakraj Gosalia, and Nathan Long. I would like to express my deep gratitude to my family for their encouragement, support, and love, as well as to my wonderful friends, Jiaying Wang, Mengjie Zhao, Miao Jing, Bing Shu, Yingfei Liao, Judy, and Shirley, for accompanying and spiritually supporting me throughout my Ph.D. journey. Finally, I gratefully acknowledge the financial support from UNSW and the China Scholarship Council for the joint scholarship, the Sydney Quantum Academy for the postgraduate top-up scholarship, and UNSW for the completion scholarship.

List of Publications

Journal Articles:

1. **W. Shi** and R. Malaney, "Entanglement of Signal Paths via Noisy Superconducting Quantum Devices," *Entropy*, vol. 25, no. 1, 153, 2023, doi: 10.3390/e25010153.

2. **W. Shi**, N. K. Kundu, and R. Malaney, "Error-Mitigated Multi-Layer Quantum Routing," accepted by *APL Quantum*. (arXiv:2409.14632)

Magazine Article:

3. **W. Shi** and R. Malaney, "Quantum Routing for Emerging Quantum Networks," *IEEE Network*, vol. 38, no. 1, pp. 140-146, 2024, doi: 10.1109/MNET.2023.3317821.

Conference Articles:

4. **W. Shi** and R. Malaney, "Signal Processing and Quantum State Tomography on Noisy Devices," in *2023 IEEE International Conference on Acoustics, Speech and Signal Processing (ICASSP)*, 2023, pp. 1-5, doi: 10.1109/ICASSP49357.2023.10094890.

5. **W. Shi** and R. Malaney, "Error-Mitigated Quantum Routing on Noisy Devices," in *2023 IEEE Global Communications Conference*, 2023, pp. 5475-5480, doi: 10.1109/GLOBECOM54140.2023.10437807.

6. **W. Shi**, N. K. Kundu, M. R. McKay, and R. Malaney, "Error-Mitigated Quantum Random Access Memory," accepted by *QCNC 2025 - International Conference on Quantum Communications, Networking, and Computing*. (arXiv:2403.06340)

Contents

List of Figures

List of Tables

Abbreviations

CX	Controlled-X
CZ	Controlled-Z
CCX	Controlled-Controlled-X
CDR	Clifford Data Regression
CSWAP	Controlled-SWAP
eCDR	extrapolated Clifford Data Regression
GHZ	Greenberger-Horne-Zeilinger
MEM	Measurement Error Mitigation
NISQ	Noisy Intermediate-Scale Quantum
PEC	Probabilistic Error Cancellation
QECC	Quantum Error-Correcting Code
QRAM	Quantum Random Access Memory
QST	Quantum State Tomography
sZNE	selected-Zero-Noise Extrapolation
ZNE	Zero-Noise Extrapolation

Chapter 1

Introduction

1.1 Overview

Current quantum devices are commonly referred to as Noisy Intermediate-Scale Quantum (NISQ) devices due to their high intrinsic error rates [1–5]. Sources of the intrinsic error include quantum gate errors, measurement errors, decoherence errors, and cross-talk errors. Quantum gate errors include 1 and 2-qubit gate errors, accumulating over a long sequence of quantum gates. Measurement errors incorrectly determine a qubit in the $|0\rangle$ state as the $|1\rangle$ state, and vice versa. Decoherence errors are caused by the short thermal relaxation and dephasing times of qubits. Cross-talk errors occur when multiple quantum operations are executed in parallel and corrupt the quantum states of qubits. To eliminate these errors and construct fault-tolerant quantum devices capable of conducting practical large-scale quantum computations, numerous quantum error correction protocols, such as the Shor code [6–8], Quantum Error-Correcting Codes (QECCs) [9–11], and surface codes [12–15], have been proposed.

However, current quantum devices are restricted not only by intrinsic errors but also by limited physical connections between qubits. These restrictions lead to quantum

error correction being typically ineffective on NISQ devices [16–18]. As an alternative, quantum error mitigation is proposed as a potential pathway to near-term quantum advantages on NISQ devices [19–29].

Quantum error mitigation methods aim to reduce the effects of system errors rather than completely eliminate them [21,30]. In general, a quantum error mitigation method generates a number of ancillary quantum circuits and applies classical post-processing to the measurement outcomes of the circuits in an attempt to deduce zero-noise results. The most common methods discussed for quantum error mitigation include Zero-Noise Extrapolation (ZNE) [31, 32], Probabilistic Error Cancellation (PEC) [28, 33], Clifford Data Regression (CDR) [34–36], and Measurement Error Mitigation (MEM) [37–40].

In ZNE, the zero-noise expectation value of an operator is extrapolated from artificially noise-scaled circuits [28, 31, 32, 41, 42]. In PEC, a target (ideal) circuit is approximated by averaging over distinct noisy circuits which consist of noisy, but implementable, quantum gates. The expectation values of the operator for the noisy circuits are combined to approximate the zero-noise expectation value for the target circuit [25,28,33,43]. CDR executes a group of near-Clifford circuits on a simulator and a quantum device, where the near-Clifford circuits are quantum circuits (collectively similar to the target circuit) composed largely of Clifford gates (gates that map Pauli operators to Pauli operators). It then utilizes linear regression or machine-learning methods to infer the zero-noise expectation value for the target circuit via the expectation values obtained from the near-Clifford circuits [34–36]. MEM aims to reduce measurement errors by generating a calibration matrix, whose inverse is utilized to compensate for the measurement errors [21].

Currently, quantum devices can be manufactured with various qubit types: e.g., superconducting [44–47], trapped ions [48–50], photonic [51–53], or silicon-based qubits [54–56]. Of particular interest to the wider community are the superconducting quantum devices developed by IBM [57–65]. Presently, these superconducting quantum devices

are made available to the wider community through a cloud platform called IBM Quantum platform [66]. Quantum Information Science toolKit (Qiskit) [67], an open-source toolbox for quantum computing, was developed alongside the cloud platform, allowing us to directly test the performance of quantum error correction and mitigation on these NISQ devices.

We focus on quantum routers with Quantum State Tomography (QST), a fundamental technology we employed to reconstruct quantum states [68–70], as the specific application to evaluate the performance of quantum error correction and mitigation on superconducting quantum devices. Quantum routers are considered a critical element of quantum networks, playing an essential role in quantum communications and computations [71–74]. A classical router allows multi-directional broadcasting in classical networks, whereas this broadcasting is impossible for quantum signals due to the no-cloning theorem [75]. As a counterpart to the classical router, the quantum router transmits the quantum signal from a singular input path to a coherent superposition of multiple output paths [73, 74, 76]. Note that the quantum router in this thesis indicates a quantum-only phenomenon and is different from the concept of classical-routing decisions for entanglement distribution [77, 78].

Beyond the unique routing functionality, the quantum router also provides the only known technique that enables Quantum Random Access Memory (QRAM) [79–84]. More specifically, the technique of the quantum router provides the foundation of exponential speedup in large data processing [81], such as quantum Fourier transform [85], discrete logarithm [86], and pattern recognition [87] algorithms. The critical advantage of QRAM is that multiple classical and/or quantum data stored in memory cells can be queried in superposition [80], demonstrating competitive strength in quantum searching of classical databases [88]. In addition, when it comes to loading classical data into the quantum Hilbert space, QRAM demonstrates advantages in handling the complexities of a dataset compared to quantum embedding [89].

In this thesis, we investigate various quantum error correction and mitigation methods, including two modified error mitigation methods that we proposed, applied to quantum routing applications with QST on current superconducting quantum devices provided by the IBM Quantum platform. The specific quantum routing applications we considered include single-layer quantum routers, multi-layer quantum routers, and QRAMs. The experimental results presented in this thesis contribute critical insights into the construction of near-term quantum communication networks.

1.2 Thesis Structure

We now summarize the structure of this thesis. In Chapter 2, we present the background knowledge required for the thesis. Chapter 3 investigates how error correction in the context of quantum routing can be fruitful for near-term networks, provided there is sufficient *a priori* statistical knowledge of errors. In this chapter, we introduce the concept of quantum routing to the generic networking community, discussing how its inclusion in near-term quantum networks may be possible even for more general noise conditions. From an experimental perspective, we design a novel quantum circuit for quantum-error-corrected quantum routing, where the circuit is experimentally executed on a 7-qubit superconducting quantum device. We verify the quantum nature of the quantum router by identifying the generation of the path entanglement via QST. The main contents of Chapter 3 have been presented in the following publication:

- **W. Shi** and R. Malaney, "Quantum Routing for Emerging Quantum Networks," *IEEE Network*, vol. 38, no. 1, pp. 140-146, 2024, doi: 10.1109/MNET.2023.3317821.

In Chapter 4, we explore a more general scenario of quantum-error-corrected routing: a 5-qubit QECC that is able to correct any single-qubit error is embedded within the quantum router. The quantum signal is transmitted to the quantum router from a sender via a noisy quantum channel, and during this transmission process, various errors

may be introduced to the signal qubit by the environment. Under this circumstance, we investigate the use of the 5-qubit QECC within the context of quantum routing involving noisy quantum channels. We also explore the performance of error-corrected QRAM on current NISQ devices under such noisy channels. With regard to the quantum error-corrected routing performance of NISQ devices, we experimentally demonstrate the significance of minimizing the number of control gates utilized, and identify the importance of the qubit-coupling map of superconducting quantum devices for realizing a quantum routing process over noisy channels. The results of Chapter 4 have been presented in the following publication:

- **W. Shi** and R. Malaney, "Entanglement of Signal Paths via Noisy Superconducting Quantum Devices," *Entropy*, vol. 25, no. 1, 153, 2023, doi: 10.3390/e25010153.

In Chapter 5, we redirect our study to quantum error mitigation from quantum error correction, in the context of quantum routing, due to the ineffective performance of error correction on current NISQ devices. In this chapter, we apply two quantum error mitigation methods, namely ZNE and PEC, to the quantum routing problem individually, as well as in a concatenated form of these two methods. We find that these error mitigation methods significantly improve the entanglement fidelity of the quantum router - to the point that quantum applications based on quantum routing become effective on current devices. The results of Chapter 5 have been presented in the following publication:

- **W. Shi** and R. Malaney, "Error-Mitigated Quantum Routing on Noisy Devices," in *2023 IEEE Global Communications Conference*, 2023, pp. 5475-5480, doi: 10.1109/GLOBECOM54140.2023.10437807.

In Chapter 6, we extend our study to multi-layer quantum routers from the single-layer quantum router, which is investigated in Chapters 3 to 5. The multi-layer quantum

router allows for further superposition of paths to extend the scalability of quantum networks. Based on this multi-layer routing application, we propose a new method named extrapolated CDR (eCDR). We benchmark the performance of multi-layer quantum routers implemented on current superconducting quantum devices instantiated with the ZNE, CDR, and eCDR methods. Our experimental results show that the new eCDR method improves the fidelity result of the 2-layer quantum router. Our work highlights how new mitigation methods built from different components of pre-existing methods, and designed with a core application in mind, can lead to significant performance enhancements. The results of Chapter 6 have been presented in the following publication:

- **W. Shi**, N. K. Kundu, and R. Malaney, "Error-Mitigated Multi-Layer Quantum Routing," arXiv:2409.14632, 2024, doi: 10.48550/arXiv.2409.14632.

In Chapter 7, we introduce a modified version of ZNE, namely selected-ZNE (sZNE). We allow sZNE to select the optimal extrapolation function for each measurement outcome with the assistance of *estimated* noisy simulation results. We experimentally deploy both methods (ZNE and sZNE) in the context of a specific application, which is QRAM, to investigate the performance of error-mitigated QRAM. We find that an eight-memory-cell QRAM moves from a low-fidelity (non-functional) outcome to a high-fidelity (functional) outcome if the most accurate extrapolation function is chosen for each measurement in sZNE. The results of Chapter 7 have been presented in the following publication:

- **W. Shi**, N. K. Kundu, M. R. McKay, and R. Malaney, "Error-Mitigated Quantum Random Access Memory," arXiv:2403.06340, 2024, doi: 10.48550/arXiv.2403.06340.

Finally, Chapter 8 summarizes the main contributions of this thesis and outlines future work. Additionally, based on a conventional QST method [69], we further present an optimized version of QST aimed at saving time and resources with a marginal expense of accuracy. We experimentally apply the conventional and optimized methods to several

quantum states on a current NISQ device to evaluate the performance of these methods. Our experiments provide additional focus on the actual use of QST as well as additional performance insights. The results of Appendix A have been presented in the following publication:

- **W. Shi** and R. Malaney, "Signal Processing and Quantum State Tomography on Noisy Devices," in *2023 IEEE International Conference on Acoustics, Speech and Signal Processing (ICASSP)*, 2023, pp. 1-5, doi: 10.1109/ICASSP49357.2023.10094890.

Chapter 2

Background

The properties of quantum mechanics, such as superposition and entanglement, promise that quantum computers can overcome challenges that classical computers cannot. In this chapter, we introduce the basic notations with background knowledge of qubits, as well as quantum hardware and software that we will use in the following chapters. We also present basic quantum error correction and mitigation methods in this chapter.

2.1 Quantum States, Operations and State Tomography

2.1.1 Quantum States

One key difference between quantum and classical computers is that quantum computers encode information in qubits, which are two-level quantum systems, while classical computers encode information in classical bits [90]. A classical bit represents one of two binary values (0 and 1), while a qubit represents a superposition of the $|0\rangle$ and $|1\rangle$ states,

which are two orthonormal states in the form of

$$|0\rangle = \begin{pmatrix} 1 \\ 0 \end{pmatrix} \quad \text{and} \quad |1\rangle = \begin{pmatrix} 0 \\ 1 \end{pmatrix}. \tag{2.1}$$

This superposition property leads to an exponential speedup in information processing for the quantum computers compared to the classical computers. The $|0\rangle$ and $|1\rangle$ states are known as the Z-basis states, and the two X-basis states are given by

$$|+\rangle = \frac{1}{\sqrt{2}}\left(|0\rangle + |1\rangle\right) \quad \text{and} \quad |-\rangle = \frac{1}{\sqrt{2}}\left(|0\rangle - |1\rangle\right). \tag{2.2}$$

Moreover, the Y-basis states are expressed as

$$|R\rangle = \frac{1}{\sqrt{2}}\left(|0\rangle + i|1\rangle\right) \quad \text{and} \quad |L\rangle = \frac{1}{\sqrt{2}}\left(|0\rangle - i|1\rangle\right), \tag{2.3}$$

where i is the imaginary unit.

Typically, an arbitrary pure single-qubit state $|\phi\rangle$ is expressed as a linear combination of the two Z-basis states in the form of

$$|\phi\rangle = \alpha|0\rangle + \beta|1\rangle, \tag{2.4}$$

where $\alpha, \beta \in \mathbb{C}$ and $|\alpha|^2 + |\beta|^2 = 1$. If the Z-basis measurement is applied to $|\phi\rangle$, the probabilities of $|\phi\rangle$ collapsing to the states $|0\rangle$ and $|1\rangle$ after the measurement are $|\alpha|^2$ and $|\beta|^2$, respectively. Since $|\phi\rangle$ is a pure state, $|\phi\rangle$ can also be represented as a density matrix ρ_1 in the form of

$$\rho_1 = |\phi\rangle\langle\phi|. \tag{2.5}$$

If ρ_1 is a mixed state, ρ_1 can be expressed as

$$\rho_1 = \sum_l p_l |\phi_l\rangle\langle\phi_l|, \tag{2.6}$$

where each pure state $|\phi_l\rangle$ occurs with probability p_l.

2.1.1.1 Superposition and Entanglement

Superposition and entanglement are two critical quantum properties that form the foundation for the development of quantum computing. Superposition allows n qubits to represent a maximum of 2^n states simultaneously. A 2-qubit quantum state $|\phi_2\rangle$, for example, has the ability to represent four quantum states at the same time. The $|\phi_2\rangle$ state is given by

$$|\phi_2\rangle = \alpha_{00}|00\rangle + \alpha_{01}|01\rangle + \alpha_{10}|10\rangle + \alpha_{11}|11\rangle, \tag{2.7}$$

where α_{00}, α_{01}, α_{10}, and $\alpha_{11} \in \mathbb{C}$ and $|\alpha_{00}|^2 + |\alpha_{01}|^2 + |\alpha_{10}|^2 + |\alpha_{11}|^2 = 1$. If $|\phi_2\rangle$ can be expressed as a tensor product of two single-qubit states, $|\phi_2\rangle$ is a product state; otherwise, $|\phi_2\rangle$ is an entangled state.

The simplest examples of entanglement are the Bell states [91–93], which are given by

$$\begin{aligned} |\Phi^+\rangle &= \frac{1}{\sqrt{2}}\left(|00\rangle + |11\rangle\right), \quad |\Phi^-\rangle = \frac{1}{\sqrt{2}}\left(|00\rangle - |11\rangle\right), \\ |\Psi^+\rangle &= \frac{1}{\sqrt{2}}\left(|01\rangle + |10\rangle\right), \quad \text{and } |\Psi^-\rangle = \frac{1}{\sqrt{2}}\left(|01\rangle - |10\rangle\right). \end{aligned} \tag{2.8}$$

For a n-qubit system, the maximally entangled state is the Greenberger-Horne-Zeilinger (GHZ) state [94], which is in the form of

$$|\text{GHZ}\rangle = \frac{1}{\sqrt{2}}\left(|0\rangle^{\otimes n} + |1\rangle^{\otimes n}\right). \tag{2.9}$$

With entanglement, secure communications, such as quantum key distribution [95, 96], and various quantum protocols, including quantum dense coding [97, 98] and quantum teleportation [99, 100], become possible.

2.1.2 Quantum Operations

2.1.2.1 Single-Qubit Operations

Quantum gates are unitary operators, which are reversible, and can be represented by unitary matrices. Since a single qubit is a two-level quantum system, a single-qubit gate is a 2×2 unitary matrix. The most commonly used single-qubit gates include the Hadamard gate, identity gate, Pauli gates (X, Y, and Z gates), and phase gates.

The Hadamard gate H is generally utilized for generating a superposition, since it converts the states $|0\rangle$ and $|1\rangle$ to the states $|+\rangle$ and $|-\rangle$, respectively. The matrix representation of H is given by

$$H = \frac{1}{\sqrt{2}} \begin{bmatrix} 1 & 1 \\ 1 & -1 \end{bmatrix}. \tag{2.10}$$

The identity gate is the identity matrix, *i.e.*,

$$I = \begin{bmatrix} 1 & 0 \\ 0 & 1 \end{bmatrix}, \tag{2.11}$$

and I applies no effect to a qubit. The Pauli gates conducts π rotations along axes, and their matrix representations are

$$X = \begin{bmatrix} 0 & 1 \\ 1 & 0 \end{bmatrix}, \quad Y = \begin{bmatrix} 0 & -i \\ i & 0 \end{bmatrix}, \quad \text{and } Z = \begin{bmatrix} 1 & 0 \\ 0 & -1 \end{bmatrix}. \tag{2.12}$$

The commonly used phase gates include S, $S^\dagger$, T, and $T^\dagger$ gates, which introduce phases of $\pi/2$, $-\pi/2$, $\pi/4$, and $-\pi/4$, respectively, to single qubits, *i.e.*, they conduct rotations along the z-axis. Their matrix representations are

$$S = \begin{bmatrix} 1 & 0 \\ 0 & i \end{bmatrix}, \quad S^\dagger = \begin{bmatrix} 1 & 0 \\ 0 & -i \end{bmatrix}, \quad T = \begin{bmatrix} 1 & 0 \\ 0 & e^{i\pi/4} \end{bmatrix}, \quad \text{and } T^\dagger = \begin{bmatrix} 1 & 0 \\ 0 & -e^{i\pi/4} \end{bmatrix}. \tag{2.13}$$

Beyond quantum gates, another commonly used quantum operation is measurement. Measurement is necessary for obtaining quantum computing results and is not a unitary operation, meaning it cannot be reversed once performed. In this thesis, we conduct

experiments on superconducting quantum devices, which only supports the Z-basis measurement. To implement the X-basis measurement, we should perform a Hadamard gate before the Z-basis measurement. The Y-basis measurement requires an $S^\dagger$ gate and a Hadamard gate sequentially before the Z-basis measurement. Note that the Z-basis measurements are single-qubit operations and can be applied in parallel to multiple qubits.

2.1.2.2 Multi-Qubit Gates

Multi-qubit gates are essential for realizing effective quantum commuting tasks, since they are required for generating entanglement. The most important 2-qubit gate is the Controlled-X (CX) gate, which converts the $|10\rangle$ state to the $|11\rangle$ state (or vice versa) and leaves the states $|00\rangle$ and $|01\rangle$ unchanged. Typically, the first and second qubits (e.g., the first and second qubits in the $|10\rangle$ state are $|1\rangle$ and $|0\rangle$, respectively) applied by the CX gate are referred to as the control and target qubits, respectively. Therefore, it can be summarized that CX gate actually applies a X gate to the target qubit if the control qubit is in the $|1\rangle$ state. When the control qubit is in a superposition, applying a CX gate to the control and target qubits generates an entangled state. The matrix representation of the CX gate is

$$\mathrm{C}X = \begin{bmatrix} 1 & 0 & 0 & 0 \\ 0 & 1 & 0 & 0 \\ 0 & 0 & 0 & 1 \\ 0 & 0 & 1 & 0 \end{bmatrix}. \tag{2.14}$$

Similar to the CX gate, the Controlled-Z (CZ) gate applies a Z gate to the target qubit when the control qubit is in the state $|1\rangle$. The matrix representation of the CZ

gate is

$$\mathrm{C}Z = \begin{bmatrix} 1 & 0 & 0 & 0 \\ 0 & 1 & 0 & 0 \\ 0 & 0 & 1 & 0 \\ 0 & 0 & 0 & -1 \end{bmatrix}. \tag{2.15}$$

Moreover, the SWAP gate has the ability to swap the states of the two qubits applied by it, where its matrix representation is

$$\mathrm{SWAP} = \begin{bmatrix} 1 & 0 & 0 & 0 \\ 0 & 0 & 1 & 0 \\ 0 & 1 & 0 & 0 \\ 0 & 0 & 0 & 1 \end{bmatrix}. \tag{2.16}$$

There are two frequently used 3-qubit gates, which are the Controlled-Controlled-X (CCX) and Controlled-SWAP (CSWAP) gates. For the three qubits applied by the CCX gate, the third qubit (regarded as the target qubit) is applied by a X gate when the first two qubits (regarded as the control qubits) are in the state $|11\rangle$. For the three qubits applied by the CSWAP gate, the last two qubits (regarded as the target qubits) are applied by a SWAP gate when the first qubit (regarded as the control qubit) is in the state $|1\rangle$.

Quantum gates and measurements are essential components for a quantum circuit, which is a model for quantum computing [101]. Typically, all qubits in the quantum circuit are initialized to the $|0\rangle$ state, followed by quantum gates and measurements on some or all of the qubits. An important metric to calculate the complexity of the quantum circuit is circuit depth, which counts the time steps required to perform all operations in the quantum circuit. Although the execution time of quantum gates may vary, each quantum gate is counted as one time step. If quantum gates are performed in parallel, only one time step is counted. In the NISQ era, circuit depth serves as an indicator of whether current quantum devices can output effective results after executing a quantum circuit.

2.1.3 Quantum State Tomography

QST is a fundamental tool to reconstruct quantum states [69, 102], and in this thesis, QST is realized via Qiskit [67]. Three projective measurements are required to reconstruct ρ_1, a single-qubit density matrix, where the three projective measurements are the X, Y, and Z-basis measurements, which are the measurements with the Pauli operators. Note that projective measurements are quantum measurements whose measurement operators are all Hermitian, orthogonal projectors [101]. The single-qubit density matrix, ρ_1, can be expressed as

$$\rho_1 = \frac{1}{2}\sum_{j=0}^{3} S_j \hat{\sigma}_j = \frac{1}{2}\left(\hat{\sigma}_0 + S_1\hat{\sigma}_1 + S_2\hat{\sigma}_2 + S_3\hat{\sigma}_3\right), \tag{2.17}$$

where $\hat{\sigma}_0 = I$, $\hat{\sigma}_1 = X$, $\hat{\sigma}_2 = Y$, and $\hat{\sigma}_3 = Z$. Note that $S_j = \mathrm{Tr}\left[\hat{\sigma}_j \rho_1\right]$ is a real value with $S_0 = 1$ due to normalization (Tr stands for the trace operation). If ρ_1 represents a pure state, then $\sum_{j=1}^{3} S_j^2 = 1$. However, if $\sum_{j=1}^{3} S_j^2 < 1$, then ρ_1 is a mixed state. From the operational perspective, the values of $\{S_j\}_{j=0}^{3}$ are determined by the results of the three projective measurements, and the relations are given as

$$\begin{aligned} &S_0 = P_{Z^{+1}} + P_{Z^{-1}} = 1, \quad S_1 = P_{X^{+1}} - P_{X^{-1}}, \\ &S_2 = P_{Y^{+1}} - P_{Y^{-1}}, \quad \text{and } S_3 = P_{Z^{+1}} - P_{Z^{-1}}, \end{aligned} \tag{2.18}$$

where $P_{Z^{+1}}$ and $P_{Z^{-1}}$ represent the probabilities of obtaining the eigenvalues $+1$ (the $|0\rangle$ state) and -1 (the $|1\rangle$ state) in the Z-basis measurement, respectively. Similarly, $P_{X^{+1}}$, $P_{X^{-1}}$, $P_{Y^{+1}}$, and $P_{Y^{-1}}$ represent similar probabilities in the X and Y-basis measurements [69]. Once S_i are determined, ρ_1 is reconstructed. Clearly, QST is a state-estimation process in nature.

The quantum state of a n-qubit state can be expressed by a density matrix ρ_n in the form of

$$\rho_n = \frac{1}{2^n}\sum_{j_1, j_2, \cdots, j_n = 0}^{3} S_{j_1, j_2, \cdots, j_n}\left(\hat{\sigma}_{j_1} \otimes \hat{\sigma}_{j_2} \otimes \cdots \otimes \hat{\sigma}_{j_n}\right), \tag{2.19}$$

where $S_{j_1,j_2,\cdots,j_n} = \mathrm{Tr}\left[(\hat{\sigma}_{j_1} \otimes \hat{\sigma}_{j_2} \otimes \cdots \otimes \hat{\sigma}_{j_n})\,\rho_n\right]$ is a real value and $j_\nu \in \{0,1,2,3\}$ is an index ($\nu = 1,2,\cdots,n$) [69]. Normalization requires that $S_{0,0,\cdots,0} = 1$, leaving $4^n - 1$ unknowns $S_{j_1,j_2,\cdots,j_n}$, which are determined by projective measurements (tensor products of n Pauli operators). However, due to some redundancy, only 3^n different projective measurements are needed for the n-qubit state's reconstruction. In a 2-qubit state's reconstruction, for example, the results of the $\{X\otimes X, X\otimes Y, X\otimes Z, Y\otimes X, Y\otimes Y, Y\otimes Z, Z\otimes X, Z\otimes Y, Z\otimes Z\}$ projective measurements are sufficient to determine the values of the 4^2-1 unknown values since any S_{j_1,j_2} with $j_1 = 0$ and/or $j_2 = 0$ is determined by the same projective measurements results. The redundancy can also be verified in Eq. (2.18), where S_0 and S_3 are both determined by the Z-basis measurement results. In a 4-qubit state's reconstruction, for example,

$$S_{0,1,2,3} = \left(P_{Z_1^{+1}} + P_{Z_1^{-1}}\right)\cdot\left(P_{X_2^{+1}} - P_{X_2^{-1}}\right)\cdot\left(P_{Y_3^{+1}} - P_{Y_3^{-1}}\right)\cdot\left(P_{Z_4^{+1}} - P_{Z_4^{-1}}\right), \quad (2.20)$$

where $P_{Z_1^{+1}}$ and $P_{Z_1^{-1}}$ are the probabilities of obtaining the $+1$ and -1 eigenvalues, respectively, when the Z-basis measurement is applied to the qubit labeled by 1. Other symbols representing probabilities have similar meanings. Based on the expression of $S_{0,1,2,3}$, it can be found that the parameters $S_{0,1,2,3}$, $S_{0,1,2,0}$, $S_{3,1,2,0}$, and $S_{3,1,2,3}$ are all determined by the results of the projective measurement with the operator $Z\otimes X\otimes Y\otimes Z$.

2.2 Quantum Hardware and Software

2.2.1 Superconducting Qubits

Among various types of qubits, superconducting qubits are leading candidates to construct the first fault-tolerant quantum computer in the future [45, 103]. Multiple world-leading quantum computing companies, such as IBM and Google, have constructed quantum devices with hundreds of superconducting qubits [103].

Josephson junctions form the foundation of superconducting quantum devices. The

Josephson junction is constructed by two superconducting electrodes separated by an insulating barrier, allowing the tunneling of Cooper pairs. The Cooper pairs are two electrons bonded together and can tunnel across the barrier without resistance at low temperatures, an effect called quantum tunneling [104]. The Josephson junction is non-dissipative and non-linear, and when shunted with a capacitor, the Josephson junction is functioned as a non-linear inductor and forms an anharmonic oscillator. The anharmonic oscillator provides quantized energy levels with different gaps between each other, where the ground state of the energy spectrum corresponds to the $|0\rangle$ state and the excited state is regarded as the $|1\rangle$ sate. With superconducting qubits, microwave pulses are utilized to implement quantum operations, including measurements [105, 106].

Compared to other types of quantum devices, superconducting qubits exhibit short coherence times and require to be operated at extremely low temperatures. However, superconducting qubits also have remarkable advantages, including short operation times and compatibility with existing semiconductor manufacturing technologies. Moreover, a superconducting qubit is easier to couple with other superconducting qubits, enabling higher scalability. With these advantages, superconducting quantum devices are regarded leading candidates for practical and scalable quantum computing [44].

In this thesis, multiple superconducting quantum devices are utilized, including a 7-qubit device named *ibmq_jakarta*, a 27-qubit device named *ibm_cairo*, and a 127-qubit device named *ibm_sherbrooke*. Note that currently, the smallest superconducting quantum devices have 127 qubits. Although the number of available qubits in the quantum devices has increased with the development of IBM hardware, the transpilation process (see Section 2.2.2.2) is always required to execute quantum circuits. Moreover, mid-circuit measurements and applying quantum gates based on these mid-circuit measurement results were not possible for low-complexity devices.

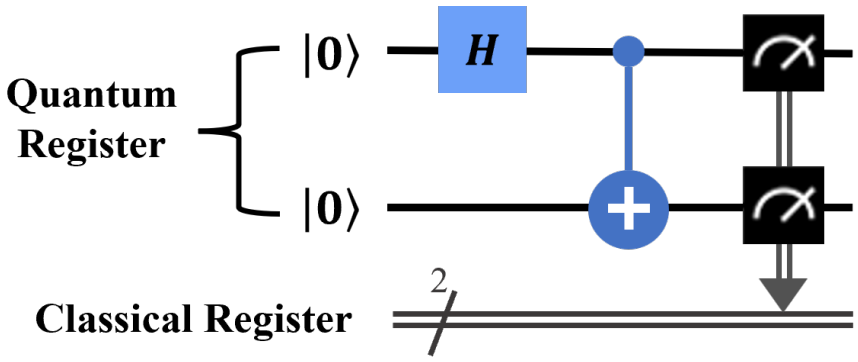

Figure 2.1: Quantum circuit with measurements generated via Qiskit. This quantum circuit has a quantum register containing two qubits and a classical register, which can store two classical bits. Note that H stands for the Hadamard gate, and the 2-qubit gate is the CX gate, which is applied to a control (denoted by the solid circle) and a target qubit (denoted by the larger circle with a plus sign). The quantum circuit prepares the $|\Phi^+\rangle$ state, one of the Bell states, followed by the Z-basis measurements, denoted by the black boxes at the end of the circuit.

2.2.2 Qiskit Software

Qiskit is software that provides access to utilize the IBM quantum devices at the levels of pulses, quantum circuits, and algorithms. Qiskit allows for manipulating qubits and construing quantum circuits, as well as calculating on quantum simulators [67]. Users of Qiskit can construct and send a quantum circuit for executions on a specific quantum device provided by the IBM Quantum platform. After the executions, the measurement outcomes of the circuit will return back to the users. In summary, Qiskit and the IBM Quantum platform together allow users to remotely access and execute quantum circuits on superconducting quantum devices.

2.2.2.1 Quantum Circuits

Via Qiskit, a quantum circuit is constructed in three main steps: (i) Firstly, generate a quantum register with n' qubits, which are all initialized in the $|0\rangle$ state, and a classical register with $n \leq n'$ bits. (ii) Apply a sequence of quantum gates to some or all of

the qubits in the quantum register. (iii) The Z-basis measurements are applied to n qubits in the quantum register, whose measurement outcomes are stored in the classical register. Generally, measurements are conducted at the end of the quantum circuit. An example quantum circuit generated via Qiskit is demonstrated in Fig. 2.1.

After an execution of the quantum circuit on a quantum device, the measurement outcome should be one of the 2^n possible states. However, if the quantum circuit is executed again, a different outcome might occur due to the superposition property of quantum mechanics. Suppose the quantum circuit is executed on the quantum device thousands of times. After the executions, the frequency (or probability) of each possible state occurring becomes the corresponding performance metric, rather than the specific measurement outcome.

In Qiskit, the measurement outcome is printed in little endian order, meaning that the classical register stores the measurement outcomes of the n qubits sequentially from right to left. The matrix representations of quantum gates are also in little endian order in Qiskit. Note that the typical convention is to use big-endian order, and, except where specified, this thesis follows big-endian order.

2.2.2.2 Transpilation Process

Any quantum circuit should be transpiled via Qiskit before being executed on a specific IBM quantum device. Transpilation is a process that maps all qubits in the quantum register to physical qubits of the quantum device and optimize all operations in the quantum circuit for execution. The significance of the transpilation process is also emphasized by the fact that not all quantum gates can be conducted directly on the IBM quantum devices, which supports only specific 1-qubit and 2-qubit gates, referred to as basis gates. Transpilation guarantees that the transpiled quantum circuit only includes basis gates before execution.

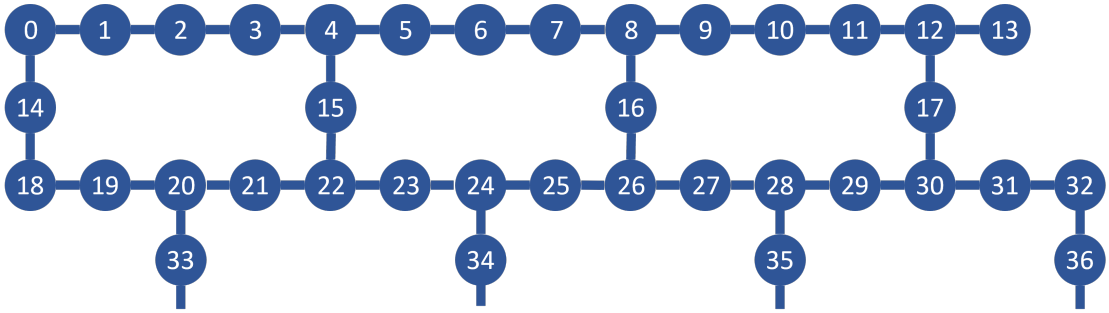

Figure 2.2: Partial topology of *ibm_sherbrooke*, a 127-qubit superconducting device provided by the IBM Quantum platform. Each circle labeled by a number represents a physical qubit of *ibm_sherbrooke*. The 2-qubit basis gate (typically the CX gate) can only be applied to pairs of physical qubits connected by a solid line.

As an example, a partial layout of the physical qubits on a 127-qubit quantum device named *ibm_sherbrooke* [66] is shown in Fig. 2.2. Each circle represents a physical qubit, which can be connected to at most three other physical qubits. The 2-qubit basis gate (typically the CX gate) can only be applied to two physical qubits that are connected to each other. Since the quantum device does not have an all-to-all structure (where all physical qubits are connected to each other), applying the 2-qubit basis gate to any two unconnected physical qubits becomes a problem. To overcome this connectivity constraint, the SWAP gates are required to route quantum states to the appropriate physical qubits, enabling the application of the 2-qubit basis gate to the desired quantum states. During the transpilation process, the SWAP gate is decomposed into three CX gates, as shown in Fig. 2.3, since the SWAP gate cannot be conducted directly on the quantum device. Due to the fact that the quantum device is noisy, the addition of the SWAP gates introduces extra noise, especially gate errors and decoherence errors. To minimize the introduced noise, the transpilation process needs to optimize the routing of quantum states to reduce the number of the SWAP gates required. The transpilation process is not deterministic and can be summarized in six main steps as follows [107,108].

(i) *Initialization.* An arbitrary quantum circuit may involve various quantum operations, including multi-qubit gates. The first step of the transpilation is to convert all

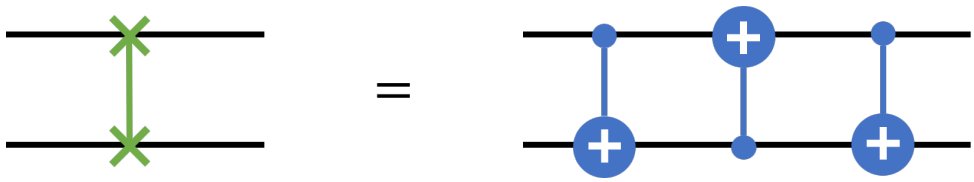

Figure 2.3: SWAP gate and its equivalent basis gates. The SWAP gate can be decomposed into three CX gates.

quantum gates into 1-qubit and 2-qubit gates.

(ii) *Layout.* All qubits in the quantum circuit are then mapped to the physical qubits on a chosen quantum device.

(iii) *Routing.* Next, the SWAP gates are inserted to complement the connectivity of the chosen quantum device.

(iv) *Translation.* Then, all quantum operations, including the inserted SWAP gates, are converted to the basis gates and the Z-basis measurements, which can be conducted directly on the quantum device.

(v) *Optimization.* In this step, an optimization process is conducted to find more efficient decompositions of quantum gates and routing processes to meet any given requirements, such as a specified circuit depth.

(vi) *Scheduling.* The final step is to optionally account for all the idle time in the transpiled quantum circuit. This step can be considered as inserting delays for qubits that are waiting for operations to be conducted on other qubits.

2.3 Quantum Error Correction and Mitigation

2.3.1 Quantum Error Correction

Current quantum devices are considered NISQ devices due to their intrinsic errors and limited connectivity between physical qubits. These drawbacks prevent quantum devices from executing efficient quantum algorithms and practical quantum computing tasks. To address this challenge, quantum error correction was introduced to detect and correct errors, protecting quantum information from decoherence and noise and paving the way for fault-tolerant quantum computing. [109].

Since qubits are restricted by the no-cloning theorem [110], quantum information cannot be duplicated, resulting in the fact that classical error correction cannot be directly applied to qubits. Therefore, the development of quantum error correction requires adaptation.

2.3.1.1 Repetition Codes

One typical classical error correction method is the repetition code, which encodes information from one bit to multiple bits to correct errors. Since qubits cannot be copied, quantum repetition code encodes information by entangling it with ancillary qubits. The simplest quantum repetition code is the three-qubit repetition code, which encodes a 1-qubit state to an entangled 3-qubit state [111–114].

In classical encoding, the only error type to consider is the bit-flip error, while quantum error correction must detect and correct both bit-flip and phase-flip errors [115–118]. The three-qubit repetition code applies different encoding strategies for each error type and is able to correct only a single bit or phase-flip error. To correct a single bit-flip error, the three-qubit repetition code maps the Z-basis states to two logical codeword

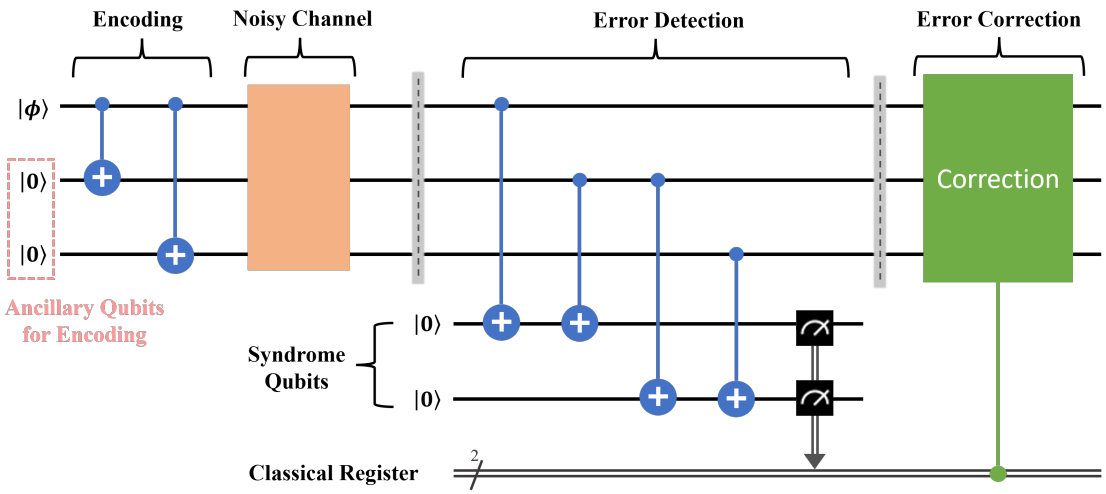

Figure 2.4: Quantum circuit of the three-qubit repetition code designed for correcting a single bit-flip error. Syndrome qubits are two ancillary qubits utilized for error detection. The operations for correction are conducted based on the measurement outcomes of the syndrome qubits (bits stored in the classical register).

states following

$$|0\rangle_L = |000\rangle \quad \text{and} \quad |1\rangle_L = |111\rangle. \tag{2.21}$$

For encoding, an arbitrary single-qubit state, $|\phi\rangle$, which contains quantum information, is entangled with two ancillary qubits initialized in the $|00\rangle$ state. The encoding logic is given by

$$|\phi\rangle = \alpha|0\rangle + \beta|1\rangle \longrightarrow |\phi\rangle_L = \alpha|000\rangle + \beta|111\rangle. \tag{2.22}$$

After encoding, $|\phi\rangle_L$ is sent to a receiver via a noisy quantum channel, during which we assume that a single bit-flip error occurs on one of the three qubits in $|\phi\rangle_L$. Another two ancillary qubits, denoted as the syndrome qubits, are needed for error detection. The syndrome qubits are used to extract syndrome information, which informs the location of the single bit-flip error, and provide guidance for correction. Specifically, the syndrome information is the measurement outcomes of the syndrome qubits. The entire process of encoding, error detection, and correction is shown in Fig. 2.4. The specific operations for correction with the corresponding syndrome information are provided in Table 2.1.

Table 2.1: Syndrome Table of Three-Qubit Repetition Code

Syndrome Information	**Noisy $\|\phi\rangle_L$**	**Correction**
$\|00\rangle$	$\alpha\|000\rangle + \beta\|111\rangle$	$I \otimes I \otimes I$
$\|10\rangle$	$\alpha\|100\rangle + \beta\|011\rangle$	$X \otimes I \otimes I$
$\|11\rangle$	$\alpha\|010\rangle + \beta\|101\rangle$	$I \otimes X \otimes I$
$\|01\rangle$	$\alpha\|001\rangle + \beta\|110\rangle$	$I \otimes I \otimes X$
$\|00\rangle$	$\alpha\|+++\rangle + \beta\|---\rangle$	$I \otimes I \otimes I$
$\|10\rangle$	$\alpha\|-++\rangle + \beta\|+--\rangle$	$Z \otimes I \otimes I$
$\|11\rangle$	$\alpha\|+-+\rangle + \beta\|-+-\rangle$	$I \otimes Z \otimes I$
$\|01\rangle$	$\alpha\|++-\rangle + \beta\|--+\rangle$	$I \otimes I \otimes Z$

After correction, $|\phi\rangle_L$ is converted back to $|\phi\rangle$ by decoding, which applies the operations from the encoding process in reverse order.

To correct a single phase-flip error, the three-qubit repetition code maps the X-basis states to two logical codeword states following

$$|+\rangle_L = |+++\rangle \quad \text{and} \quad |-\rangle_L = |---\rangle. \tag{2.23}$$

Therefore, the encoding logic of $|\phi\rangle$ turns to

$$|\phi\rangle = \alpha|0\rangle + \beta|1\rangle \longrightarrow |\phi\rangle_L = \alpha|+++\rangle + \beta|---\rangle. \tag{2.24}$$

The quantum circuit of encoding, error detection, and correction for the three-qubit repetition code correcting a single phase-flip error is shown in Fig. 2.5, and the operations for correction are provided in Table 2.1.

To correct both bit and phase-flip errors, the Shor code [6] was proposed. The encoding logic of the Shor code is given by

$$\begin{aligned} |0\rangle_L &= \frac{1}{2\sqrt{2}} \left(|000\rangle + |111\rangle\right) \otimes \left(|000\rangle + |111\rangle\right) \otimes \left(|000\rangle + |111\rangle\right) \\ \text{and} \quad |1\rangle_L &= \frac{1}{2\sqrt{2}} \left(|000\rangle - |111\rangle\right) \otimes \left(|000\rangle - |111\rangle\right) \otimes \left(|000\rangle - |111\rangle\right). \end{aligned} \tag{2.25}$$

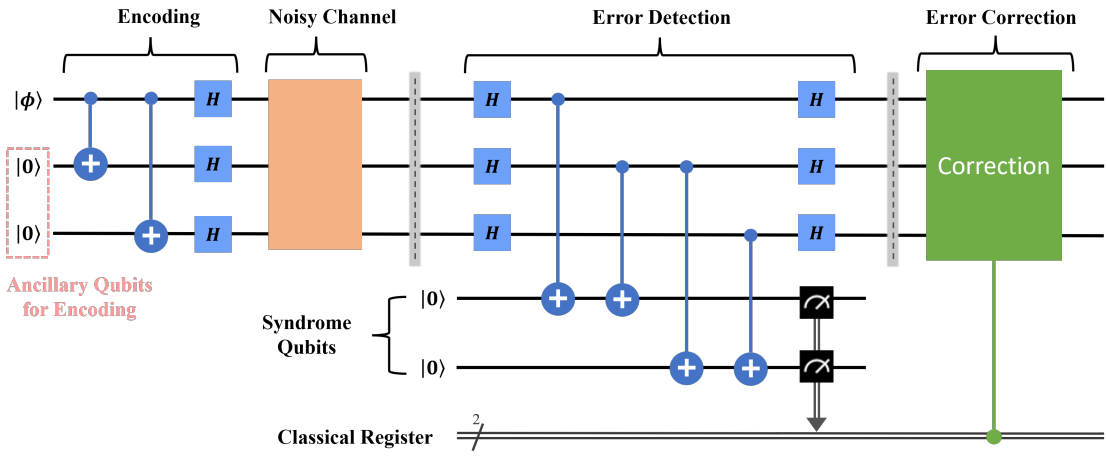

Figure 2.5: Quantum circuit of the three-qubit repetition code designed for correcting a single phase-flip error.

The encoding process of the Shor code is illustrated in Fig. 2.6. The Shor code is developed based on the three-qubit repetition code and able to correct any single-qubit errors. The drawback of the Shor code is that it encodes a 1-qubit state into a 9-qubit state, requiring eight ancillary qubits.

2.3.1.2 The Stabilizer Code

At least four ancillary qubits are required to encode a single qubit and correct an arbitrary single-qubit error. One of the well-known smallest quantum error correction codes is the [[5,1,3]] stabilizer code [119], which uses five qubits to encode one qubit with distance three. Note that three is the minimum distance required for a quantum error correction code to detect up to two errors and correct one error. The generators of the [[5,1,3]] code are

$$\begin{aligned} &M_1 = X \otimes Z \otimes Z \otimes X \otimes I, \quad M_2 = I \otimes X \otimes Z \otimes Z \otimes X, \\ &M_3 = X \otimes I \otimes X \otimes Z \otimes Z, \quad \text{and} \quad M_4 = Z \otimes X \otimes I \otimes X \otimes Z, \end{aligned} \tag{2.26}$$

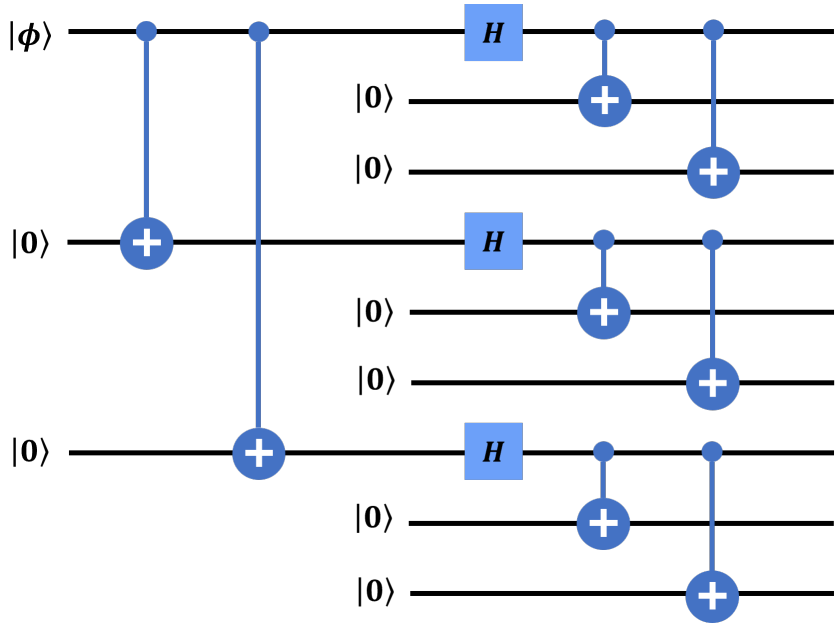

Figure 2.6: Quantum circuit for encoding in the Shor code. The single-qubit state, $|\phi\rangle$, is encoded into nine qubits.

and the encoding logic is given by $|\phi\rangle = \alpha|0\rangle + \beta|1\rangle \longrightarrow |\phi\rangle_L = \alpha|0\rangle_L + \beta|1\rangle_L$, where

$$\begin{aligned}|0\rangle_L = \frac{1}{4}\,(&|00000\rangle + |10010\rangle + |01001\rangle + |10100\rangle + |01010\rangle \\ &- |11011\rangle - |00110\rangle - |11000\rangle - |11101\rangle - |00011\rangle \\ &-|11110\rangle - |01111\rangle - |10001\rangle - |01100\rangle - |10111\rangle + |00101\rangle) \quad \text{and}\end{aligned} \tag{2.27}$$

$$\begin{aligned}|1\rangle_L = \frac{1}{4}\,(&-|11111\rangle - |01101\rangle - |10110\rangle - |01011\rangle - |10101\rangle \\ &+ |00100\rangle + |11001\rangle + |00111\rangle + |00010\rangle + |11100\rangle \\ &+|00001\rangle + |10000\rangle + |01110\rangle + |10011\rangle + |01000\rangle - |11010\rangle)\,.\end{aligned} \tag{2.28}$$

An example of a quantum circuit [120] that encodes the [[5,1,3]] code is illustrated in Fig. 2.7. Similar to the three-qubit repetition code, the [[5,1,3]] code requires four additional ancillary qubits, known as syndrome qubits, to provide information for error detection and correction [120, 121]. The quantum circuit of the error detection and correction in the [[5,1,3]] code is shown in Fig. 2.8. A total of eight ancillary qubits are needed: four for encoding and four serving as the syndrome qubits. The quantum circuit

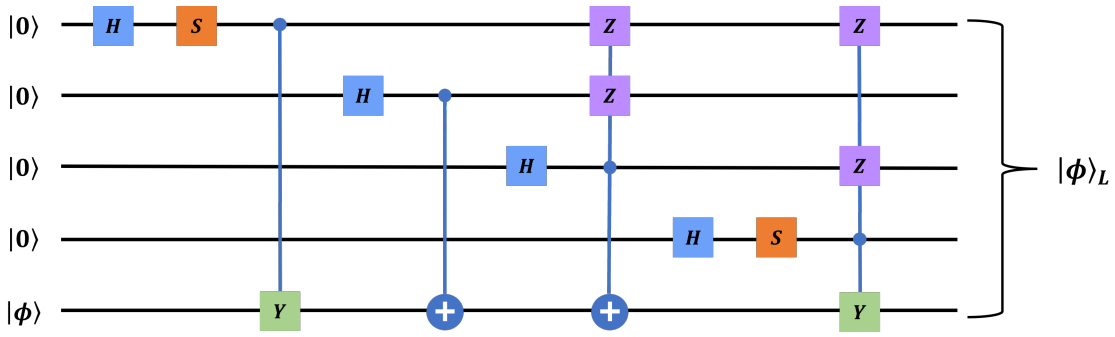

Figure 2.7: Quantum circuit for encoding in the [[5,1,3]] code. The single-qubit state, $|\phi\rangle$, is encoded into a five-qubit state, $|\phi\rangle_L$. Note that S is a single-qubit phase gate, which induces a $\pi/2$ phase.

for error detection in Fig. 2.8 is employed to measure the observables M_1, M_2, M_3, and M_4. The measurement outcome of each syndrome qubit indicates the corresponding eigenvalue of these observables [101]. To correct a single-qubit error, the syndrome information (measurement outcomes of the four syndrome qubits) is required to determine the specific correction operations, as shown in Table 2.2.

Table 2.2: Syndrome Table of the [[5,1,3]] Code

Syndrome Information	**Correction**	**Syndrome Information**	**Correction**
$\|0000\rangle$	$I \otimes I \otimes I \otimes I \otimes I$	$\|0010\rangle$	$I \otimes I \otimes Z \otimes I \otimes I$
$\|0001\rangle$	$X \otimes I \otimes I \otimes I \otimes I$	$\|1001\rangle$	$I \otimes I \otimes I \otimes Z \otimes I$
$\|1000\rangle$	$I \otimes X \otimes I \otimes I \otimes I$	$\|0100\rangle$	$I \otimes I \otimes I \otimes I \otimes Z$
$\|1100\rangle$	$I \otimes I \otimes X \otimes I \otimes I$	$\|1011\rangle$	$Y \otimes I \otimes I \otimes I \otimes I$
$\|0110\rangle$	$I \otimes I \otimes I \otimes X \otimes I$	$\|1101\rangle$	$I \otimes Y \otimes I \otimes I \otimes I$
$\|0011\rangle$	$I \otimes I \otimes I \otimes I \otimes X$	$\|1110\rangle$	$I \otimes I \otimes Y \otimes I \otimes I$
$\|1010\rangle$	$Z \otimes I \otimes I \otimes I \otimes I$	$\|1111\rangle$	$I \otimes I \otimes I \otimes Y \otimes I$
$\|0101\rangle$	$I \otimes Z \otimes I \otimes I \otimes I$	$\|0111\rangle$	$I \otimes I \otimes I \otimes I \otimes Y$

2.3.2 Quantum Error Mitigation

Quantum error correction utilizes additional qubits to encode quantum information for error correction, laying the foundation for fault-tolerant quantum computing in the future. However, current quantum devices are limited by their intrinsic error rates and the

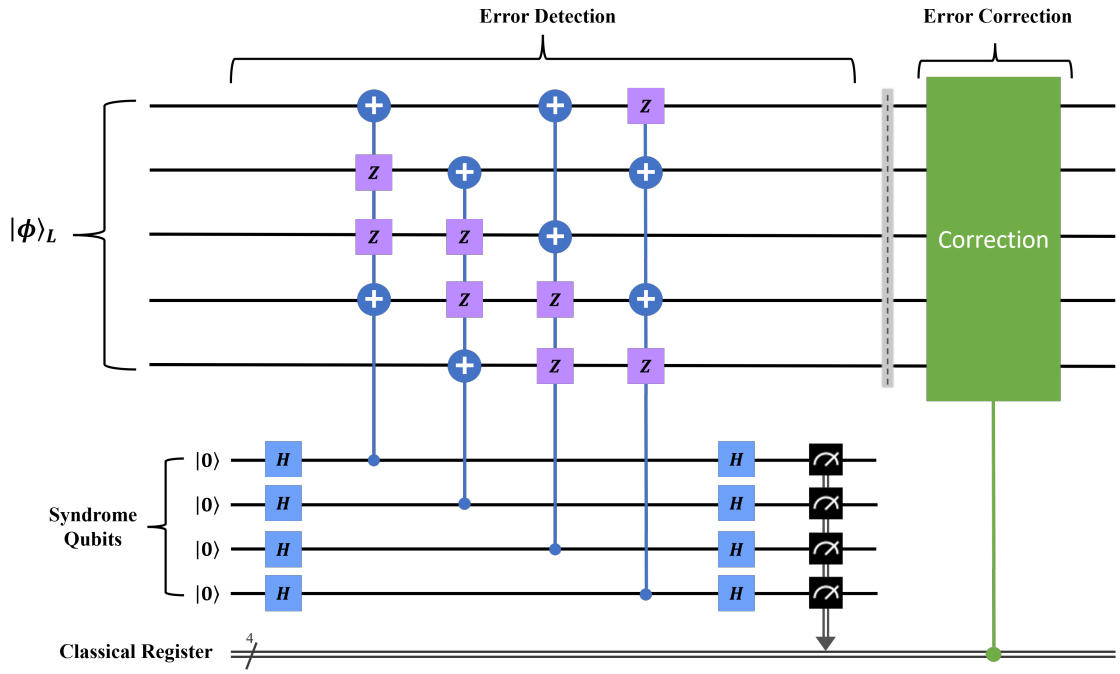

Figure 2.8: Quantum circuit for error detection and correction in the [[5,1,3]] code. The correction operations are performed based on the measurement outcomes of the four syndrome qubits.

connectivity of physical qubits, making them unsuitable for quantum error correction. To address this challenge, quantum error mitigation was proposed to decrease the effects of errors instead of correcting them [20, 21, 30].

Quantum error mitigation requires additional executions of quantum circuits and classical post-processing to realize near-term quantum advantages on NISQ devices [19–21]. The noise introduced to a quantum circuit that is executed on a quantum device increases with the circuit size (the number of qubits) and depth (the number of quantum operations). The effectiveness of quantum error mitigation is affected by the introduced noise, meaning that, given a specific hardware error rate, quantum error mitigation is only practical within a range of circuit complexity (circuit sizes and depths). Different mitigation methods have varying overheads due to the execution of the additional quantum circuits. A suitable mitigation method should be determined based on circuit

complexity and accuracy requirements for effective error mitigation to achieve optimal performance.

One promising quantum error mitigation method is ZNE [31, 32, 41, 122], which extrapolates zero-noise results from noisy results obtained from ancillary quantum circuits executed on a quantum device. These ancillary circuits are constructed by artificially introducing noise to a quantum circuit of interest (denoted as the original circuit), with each ancillary circuit possessing a distinct noise level (see details in Section 5.1.1). Another promising mitigation method is PEC [28,33,43], in which noiseless quantum gates are represented as linear combinations of noisy, implementable quantum gates. Then, the original circuit is represented as a linear combination of noisy quantum circuits, each consisting of noisy but implementable gates (see details in Section 5.1.2). To obtain higher accuracy in estimated zero-noise results, more sampling is required; that is, a greater number of the noisy quantum circuits (ancillary circuits) should be executed on a quantum device. Yet another promising method is CDR [34–36,123], a learning-based error mitigation technique. CDR involves executing a group of near-Clifford circuits both on a noiseless simulator and a quantum device, generating a linear regression model based on the noiseless and noisy results. The experimental results collected from the original circuit run on the quantum device are then mitigated using the linear regression model (see details in Section 6.2.1).

The ZNE, PEC, and CDR methods are effective in mitigating intrinsic errors in quantum devices, such as quantum gate and decoherence errors. However, measurement errors, typically introduced during the final step of quantum circuit execution, cannot be eliminated by these methods. To address this, MEM methods [37, 38, 124, 125] have been proposed specifically to mitigate these errors.

2.3.2.1 Measurement Error Mitigation

Measurement errors mistakenly read a qubit in the $|0\rangle$ state as the $|1\rangle$ state, and vice versa. In this thesis, we choose a MEM method [126] provided by Qiskit to reduce measurement errors. This protocol requires ancillary quantum circuits, which we call calibration circuits. One needs 2^n calibration circuits to construct a $2^n \times 2^n$ calibration matrix M, where n is the number of qubits that are measured. Each calibration circuit prepares the n qubits to one of 2^n Z-basis states before using the Z-basis measurements to measure them. If 3 qubits are measured, for example, the MEM protocol generates eight calibration circuits, where each circuit prepares one of the eight 3-qubit Z-basis states *i.e.*, $\{|000\rangle, |001\rangle, \cdots, |111\rangle\}$. The measurement results of the calibration circuits determine M, and M^{-1} is then applied to experimental results to eliminate measurement errors.

Other promising quantum error mitigation methods, including ZNE, PEC, and CDR, are also utilized in this thesis. The specific working principle of these methods will be introduced in the following chapters.

Chapter 3

Quantum Routing for Emerging Quantum Networks

In near-term quantum networks, quantum routers can be deployed using NISQ devices. In principle, such noisy devices can create, receive, transmit, and route qubits over quantum channels. However, noisy quantum channels that connect NISQ devices introduce unwanted errors, largely through the entanglement between the information qubit and the environment [115, 127]. This unwanted entanglement causes the leakage from the defined two-level qubit space into a larger Hilbert space [128]. Multiple quantum error correction protocols have been proposed to eliminate the errors caused by noisy quantum channels, e.g. [129–134].

In this chapter, we develop and experimentally test a quantum router with a *non-general* error correction protocol - a protocol well suited to noise conditions with similarities to the amplitude damping channel [135–137]. There are two main aims in this study:

(i) First, we wish to point out how error correction in the context of quantum routing may still be fruitful for near-term networks - if enough *a priori* statistical knowledge on

errors are known. the errors intrinsic to a NISQ device are known. We investigate channels with characteristics similar to the amplitude damping channel to make this point.[1]

(ii) Second, we wish to introduce the concept of quantum routing to the generic networking community, discussing how its inclusion in near-term quantum networks may be possible even for more general noise conditions.

With these two aims in mind, we summarize our three main contributions as follows.

(i) We design a novel quantum circuit for quantum-error-corrected quantum routing, based on noisy superconducting qubits.

(ii) We experimentally execute the quantum circuit on a 7-qubit NISQ device, *ibmq_jakarta*, accessed through the IBM Quantum platform.

(iii) We verify the quantum nature of the quantum router by identifying the generation of the path-entanglement via QST. We also discuss possible applications of path-entanglement for networks and the use of enhanced error mitigation techniques in improving quantum routing.

3.1 Quantum Routing with Error Correction

3.1.1 Quantum Routing in Future Networks

An overview of a large-scale quantum communication network is depicted in Fig. 3.1. A signal qubit is transmitted from a sender to the two end users simultaneously via quantum routers. Only one end user will receive the signal qubit upon collapse of the

[1]We do not claim such channels are representative of any current NISQ device - we simply wish to show how some knowledge on a quantum channel can sometimes greatly assist the error correction.

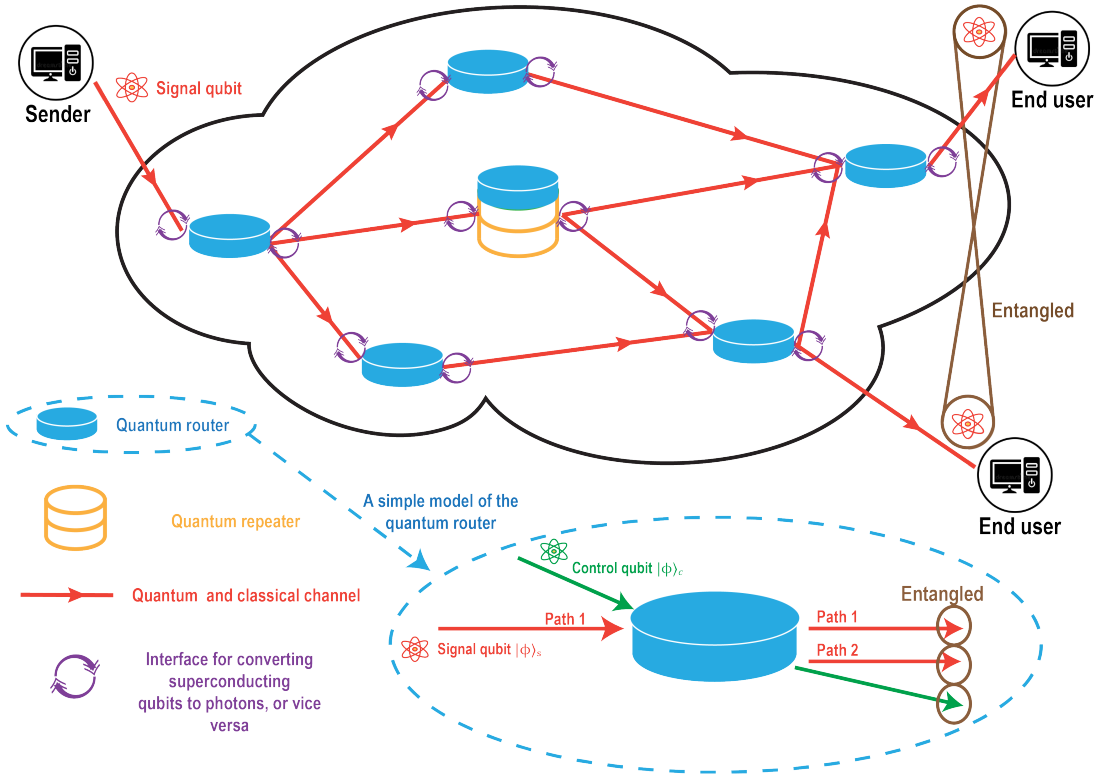

Figure 3.1: An overview of a possible future quantum communication network with embedded quantum routers.

superposition of the paths. Although not discussed in any detail here, Fig. 3.1 also includes an important component of any future quantum network - a quantum repeater. Due to the short coherence time of qubits, and the loss/noise inherent in most quantum channels, quantum repeaters will be needed to realize long-distance transmission of quantum signals. We anticipate quantum routers and quantum repeaters to co-exist in emerging quantum networks, complementing and enhancing each other's functionality (but one does not *require* the other).

A simple model of the quantum router is depicted in the bottom of Fig. 3.1. Here, the control qubit $|\phi\rangle_c$ is a superposition state and contains the control information that directs the path of a signal qubit $|\phi\rangle_s$, which carries the signal information and is received

by the quantum router via path 1. Specifically, $|\phi\rangle_c$ and $|\phi\rangle_s$ are given by

$$\begin{aligned} |\phi\rangle_c &= \alpha_c|0\rangle_c + \beta_c|1\rangle_c = \frac{1}{\sqrt{2}}\left(|0\rangle_c + |1\rangle_c\right) \quad \text{and} \\ |\phi\rangle_s &= \alpha_s|0\rangle_s + \beta_s|1\rangle_s = \cos\left(\frac{\pi}{4}\right)|0\rangle_s + e^{i\pi/4}\sin\left(\frac{\pi}{4}\right)|1\rangle_s, \end{aligned} \tag{3.1}$$

where α_c, β_c, α_s, and β_s are complex numbers satisfying $|\alpha_c|^2 + |\beta_c|^2 = 1$ and $|\alpha_s|^2 + |\beta_s|^2 = 1$. We define that $\alpha_c = \beta_c = 1/\sqrt{2}$, $\alpha_s = \cos(\pi/4)$, and $\beta_s = e^{i\pi/4}\sin(\pi/4)$. The quantum router requires an ancillary qubit $|\phi\rangle_n$, which is initially in the $|0\rangle$ state at path 2 and contains no signal information. The output of the quantum router $|\Phi\rangle_f$ is an entanglement between the control qubit and the two paths, where $|\Phi\rangle_f$ is given by

$$|\Phi\rangle_f = \alpha_c|0\rangle_c|\phi\rangle_s^{p_1}|\phi\rangle_n^{p_2} + \beta_c|1\rangle_c|\phi\rangle_n^{p_1}|\phi\rangle_s^{p_2}, \tag{3.2}$$

where the superscripts p_1 and p_2 denote that the corresponding qubit is in the path 1 and 2, respectively. The signal qubit is routed to path 1 when $|\phi\rangle_c$ is in the $|0\rangle_c$ state and to path 2 when $|\phi\rangle_c$ is in the $|1\rangle_c$ state. When $|\phi\rangle_c$ is a superposition state, the two paths both "possess" the signal qubit.

3.1.2 Noisy Quantum Channel

While the quantum router protocol outlined above assumes zero channel noise, we wish to consider in this chapter the more realistic situation where noise channels are present. That is, we assume the states $|\phi\rangle_c$ and $|\phi\rangle_s$ are prepared at some sender, and then passed through noisy quantum channels. We build a parameterized noisy quantum channel that has similar characteristics to the amplitude damping channel. The details of the noisy channel are not important in this work, we simply require that we have an effective method within the NISQ device to add arbitrary noise to the qubits, and that the level of that noise can be parameterized with a single parameter.

The qubits that transmitted through the noisy quantum channel can be regarded as an open system that interacts with the environment during the transmission. We add

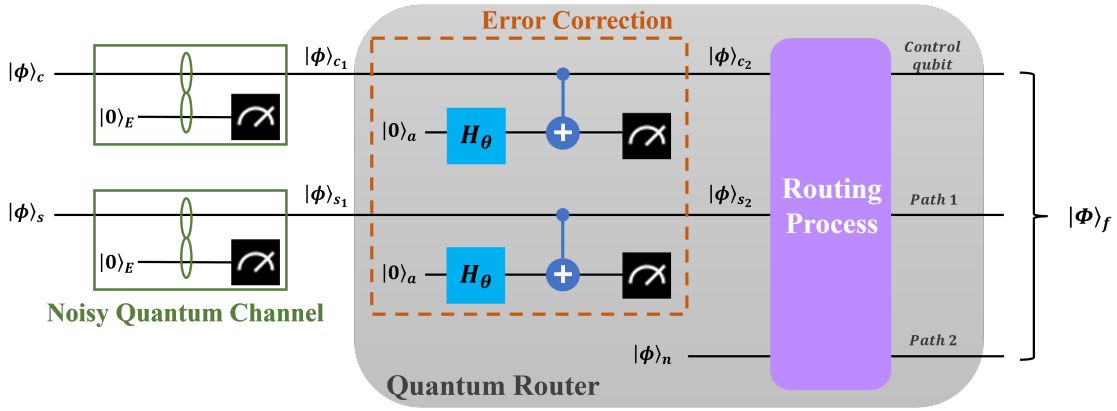

Figure 3.2: Schematic diagram of a quantum router with noisy quantum channels and error correction. Note, $|0\rangle_E$ is an auxiliary qubit that simulates the environment, and $|0\rangle_a$ stands for an ancillary qubit.

an auxiliary qubit to simulate the environment, which starts in a pure state $|0\rangle_E$, as shown in the green boxes of Fig. 3.2. The amplitude damping channel models energy relaxation from an excited state to the ground state, and we define U as the amplitude damping channel in this chapter. The evolution of $|\phi\rangle_s$ with the environment under U can be expressed as

$$U|\phi\rangle_s|0\rangle_E = \alpha_s|0_s0_E\rangle + \beta_s\sqrt{\gamma}|0_s1_E\rangle + \beta_s\sqrt{1-\gamma}|1_s0_E\rangle, \tag{3.3}$$

where $\gamma \in [0,1]$ is a tunable parameter, representing the strength of the noise in U. Specifically, U is a unitary matrix written as

$$U = \begin{bmatrix} 1 & 0 & 0 & 0 \\ 0 & \sqrt{1-\gamma} & \sqrt{\gamma} & 0 \\ 0 & -\sqrt{\gamma} & \sqrt{1-\gamma} & 0 \\ 0 & 0 & 0 & 1 \end{bmatrix}. \tag{3.4}$$

There is no noise when γ equals to 0, and with the increase of γ, the strength of the noise in U grows.

Next, and different from amplitude damping,[2] we make a Z-basis measure on the

[2]To realize the amplitude damping channel on a NISQ device, we would not imple-

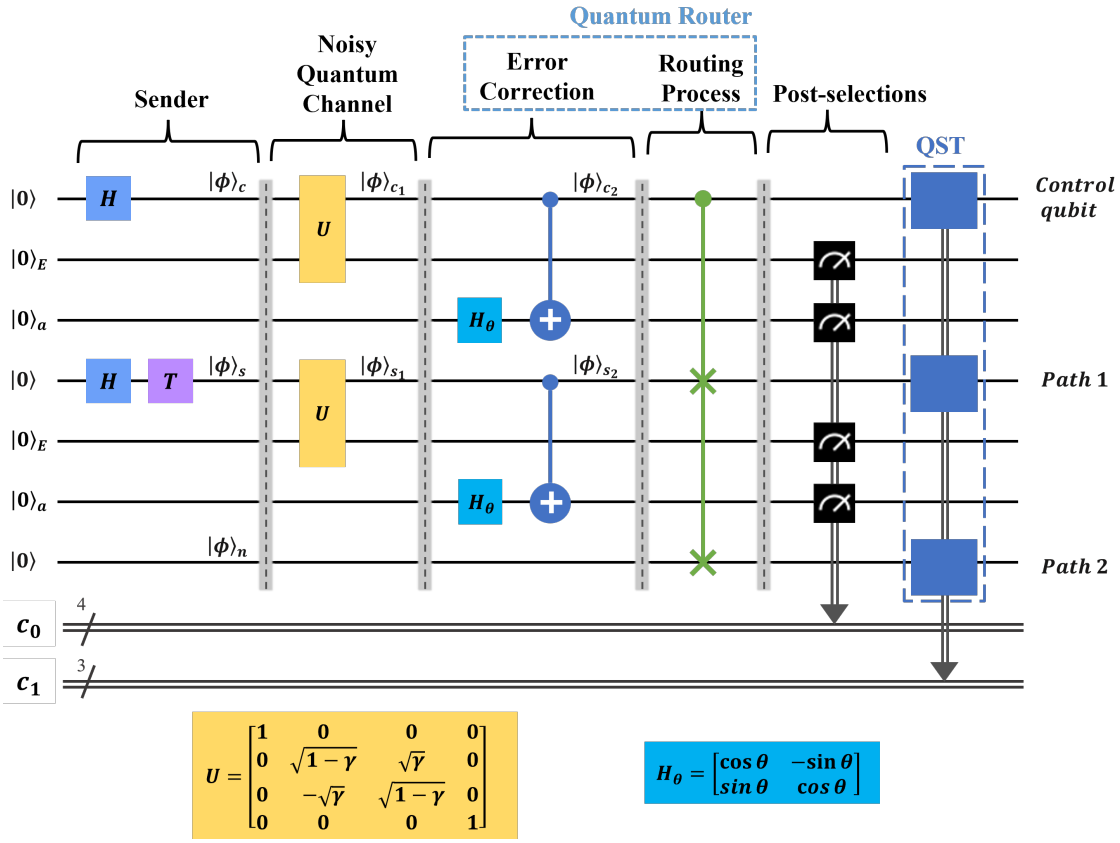

Figure 3.3: Quantum circuit of the quantum router with the error correction and QST. H represents the Hadamard gate, and T the 1-qubit phase gate, which induces a $\pi/4$ phase. The 3-qubit gate in purple is the CSWAP gate, which exchanges the two quantum states (represented by the two crosses) when the control qubit (represented by the solid circle) is in the $|1\rangle$ state. c_0 and c_1 are classical registers used for storing the measurement results in the post-selection and the state tomography, respectively.

auxiliary qubit and only keep the resulting state if the measurement outcome is $|0\rangle_E$, and at this point, the resulting state is

$$|\phi\rangle_{s_1} = \frac{1}{N_1}\left(\alpha_s|0\rangle_s + \beta_s\sqrt{1-\gamma}|1\rangle_s\right), \tag{3.5}$$

where $N_1 = \sqrt{|\alpha_s|^2 + |\beta_s|^2(1-\gamma)}$ is a normalization factor. This process, which delivers our required parameterized noisy channel, has a success probability of $p_1 = N_1^2$ [129].

To run our experiments (see Section 3.2), we first must "imprint" the noisy quantum channel onto the device, since in the current devices no such channel exists. This imprinted channel mimics noise that would be added to the qubits as they traversed a wider network before entering the router. After imprinting the noise, we "forget" we know the exact channel parameter, γ, when we attempt the error correction. This is a means to model the realistic situation where we do not know exactly the noise in the channel, only some general characteristics, but must still attempt some form of error correction.

In this work, we imprint the noisy channel by U, which requires us to set a specific value of γ, as shown in Fig. 3.3. We assume the noisy quantum channel to possess a γ in the range $0-1$, with a uniform distribution. At the error correction phase, we assume only knowledge of the distribution of γ, not its specific value in any realization. We set our estimate of γ , which we refer to as $\gamma_g = 0.5$, by setting it at the mean of the distribution. Although some real-world channels could be approximated by this process, we do not claim we have truly modeled a real-world channel. We use our channel scheme to simply illustrate that when statistical information on a channel is available, quantum error correction on quantum routing within a NISQ device becomes possible. Other, more complicated, channels will likely exist in the wide range of NISQ devices now being produced via multiple technology implementations. While we expect similar

ment the post-selections (Z-basis measurements) on the auxiliary qubits. Mathematically, following the unitary evolution of the combined system, the "environment" qubits would be traced out before executing the error correction.

outcomes to those reported here for some of these other channels, we should be clear that the explicit results we show are specific to the statistical noise model we have assumed.

3.1.3 The Error Correction Protocol

The correction protocol [129] we adopt is not designed for an arbitrary error on a qubit, but one which develops for a specific noise model. Our adopted scheme applies to scenarios where some access to the entangled environment may be available [138] or where a weak measurement is done to detect leakage from the system [129], and the loss rate can be estimated.

We first apply a special Hadamard gate H_θ with a parameter θ to $|0\rangle_a$, which is an ancillary qubit. The representation of H_θ is

$$H_\theta = \begin{bmatrix} \cos\theta & -\sin\theta \\ \sin\theta & \cos\theta \end{bmatrix}. \tag{3.6}$$

Then, a CX gate is performed on $|\phi\rangle_{s_1}$ and the ancillary qubit (performed on the control and target qubit, respectively), as illustrated in the orange dashed box of Fig. 3.2. The resulting transformation can be expressed as

$$\begin{aligned} |\phi\rangle_{s_1}|0\rangle_a &= \frac{1}{N_1}\left(\alpha_s|0\rangle_s + \beta_s\sqrt{1-\gamma}|1\rangle_s\right)\otimes|0\rangle_a \\ &\xrightarrow{I\otimes H_\theta} \frac{1}{N_1}\left(\alpha_s|0\rangle_s + \beta_s\sqrt{1-\gamma}|1\rangle_s\right)\otimes(\cos\theta|0\rangle_a + \sin\theta|1\rangle_a) \\ &\xrightarrow{\mathrm{C}X} \frac{1}{N_1}\Big(\alpha_s\cos\theta|0_s0_a\rangle + \alpha_s\sin\theta|0_s1_a\rangle \\ &\qquad + \beta_s\sqrt{1-\gamma}\cos\theta|1_s1_a\rangle + \beta_s\sqrt{1-\gamma}\sin\theta|1_s0_a\rangle\Big). \end{aligned} \tag{3.7}$$

The last step of the error correction requires a post-selection method applied to the ancillary qubit. This method involves the retention of the post-selected state only when the Z-basis measurement result of the ancillary qubit is $|0\rangle_a$. The resulting post-selected state by this process can be written,

$$|\phi\rangle_{s_2} = \frac{1}{N_1N_2}\left(\alpha_s\cos\theta|0\rangle_s + \beta_s\sqrt{1-\gamma}\sin\theta|1\rangle_s\right), \tag{3.8}$$

where N_2 is a normalization factor expressed as

$$N_2 = \frac{1}{N_1}\sqrt{|\alpha_s \cos\theta|^2 + |\beta_s \sin\theta|^2(1-\gamma)}. \tag{3.9}$$

When we set $\theta = \arctan(1/\sqrt{1-\gamma})$, giving $\cos\theta/\sin\theta = \sqrt{1-\gamma}$, $|\phi\rangle_{s_2} = |\phi\rangle_s$ with the success probability of the error correction $p_2 = N_2^2$ [129]. Note that we only used $|\phi_s\rangle$ as an example for demonstrating the derivations, and when the noisy quantum channel and the error correction are applied to $|\phi\rangle_c$, the process is similar.

Our adopted correction protocol is different from the quantum error correction protocols introduced in Section 2.3.1. These latter protocols encode a logical qubit to multiple physical qubits and rely on syndrome information for error correction. In contrast, our adopted correction protocol employs post-selections, terminating the entire procedure if the auxiliary or ancillary qubits yield undesired outcomes. Due to this distinction, the adopted correction protocol can also be regarded as a noise-adapted error detection or mitigation protocol.

3.2 Experiments

3.2.1 Experimental Setup

Our experiments are implemented on the IBM quantum device, *ibmq_jakarta*, which has seven superconducting qubits in a horizontal H-shaped geometry [66]. This quantum device only supports five basis gates, namely the single-qubit gates I, RZ, $\sqrt{X}$, and X, and the two-qubit gate CX, as shown in Table. 3.1. The quantum circuit of the router (alongside the noisy quantum channel and the error correction) is shown in Fig. 3.3.

The three router qubits, (*i.e.*, counting from the top - the first, fourth, and last qubit in the quantum circuit of Fig. 3.3), are prepared as $|\phi\rangle_c$, $|\phi\rangle_s$, and $|\phi\rangle_n$ via single qubit gates. The two qubits initialized in the $|0\rangle_E$ state are two auxiliary qubits that simulate the environment, and the two qubits initialized in the $|0\rangle_a$ state stand for the

Table 3.1: Basis Gates of *ibmq_jakarta*

Basis Gates	**Matrix Representation**
single-qubit gate I	$I = \begin{bmatrix} 1 & 0 \\ 0 & 1 \end{bmatrix}$
single-qubit gate RZ (single-qubit rotation about the z-axis)	R$Z(\varphi)$[1] $= \begin{bmatrix} e^{-i\frac{\varphi}{2}} & 0 \\ 0 & e^{i\frac{\varphi}{2}} \end{bmatrix}$
single-qubit gate $\sqrt{X}$	$\sqrt{X} = \frac{1}{2}\begin{bmatrix} 1+i & 1-i \\ 1-i & 1+i \end{bmatrix}$
single-qubit gate X	$X = \begin{bmatrix} 0 & 1 \\ 1 & 0 \end{bmatrix}$
two-qubit gate CX	CX[2] $= \begin{bmatrix} 1 & 0 & 0 & 0 \\ 0 & 0 & 0 & 1 \\ 0 & 0 & 1 & 0 \\ 0 & 1 & 0 & 0 \end{bmatrix}$

[1] φ is a phase term.
[2] Qiskit uses little-endian order.

ancillary qubits used in the error correction protocol. As discussed earlier, to realize the noisy channel and the error correction on the quantum device, post-selections are performed on these four qubits, as illustrated in Fig. 3.3. The classical registers c_0 contains the measurement outcomes of the four qubits. In our experiments, we set $\gamma \in \{0, 0.1, 0.2, \cdots, 0.9\}$ for the noisy channel, and for the error correction θ is set based on γ_g, *i.e.*, $\theta = \arctan(1/\sqrt{1-\gamma_g})$. The CSWAP gate is performed to realize the quantum routing process, which is the core part of the router. The CSWAP gate acts on the three router qubits: the positions of $|\phi\rangle_{s_2}$ and $|\phi\rangle_n$ would be swapped and unchanged when $|\phi\rangle_{c_2}$ is in the $|1\rangle$ and $|0\rangle$ state, respectively. The classical register c_1 contains the measurement outcomes of QST, which is utilized to identify the router output.

We choose the fidelity F between ρ' and ρ as one of our performance metrics, where $\rho' = |\Phi\rangle_f\langle\Phi|$ is the "theoretical" density matrix of the router output, and ρ is the "experimental" density matrix of the router output. Note that ρ is reconstructed via QST (see Subsection 2.1.3). The fidelity, F, is given by

$$F = \left(\mathrm{Tr}\sqrt{\sqrt{\rho}\,\rho'\sqrt{\rho}}\right)^2. \tag{3.10}$$

Note that F estimates the similarity between ρ' and ρ, and ranges from 0 to 1. When ρ' and ρ are identical to each other, F equals 1, and when ρ' and ρ are orthogonal to each other, F equals 0.

The whole experimental procedure to determine F is depicted in Fig. 3.4. The quantum circuit should first be transpiled to a circuit that only includes basis gates - *i.e.*, gates that can be implemented on the quantum device directly (more details of the transpilation process are provided in Subsection 2.2.2.2). For conducting QST, different types of measurements are attached at the end of the transpiled circuit and 27 tomography circuits (the 27 measurements $\{X \otimes X \otimes X, X \otimes X \otimes Y, \cdots, Z \otimes Z \otimes Z\}$ are required for rebuilding the 3-qubit state) are generated. We then send these tomography circuits with γ_g and a chosen γ to the quantum device, which executes each tomography circuit 100,000 times. Due to the fact that the quantum device is noisy, we

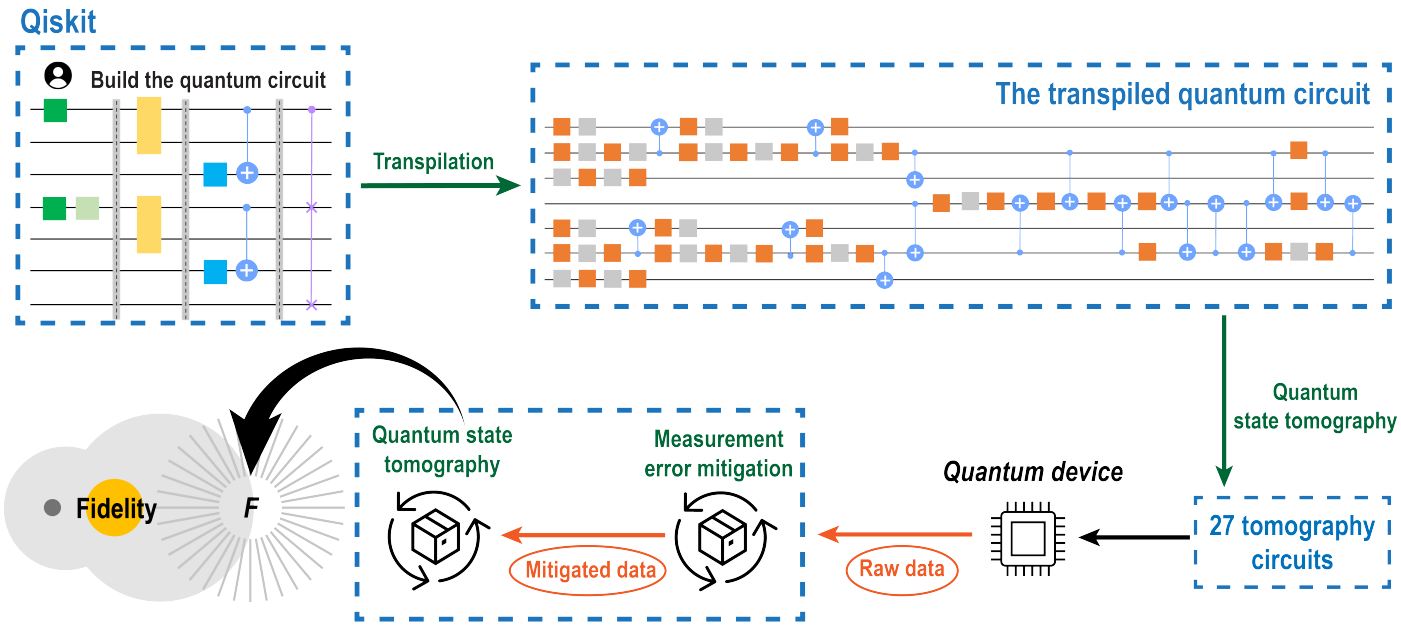

Figure 3.4: An illustration of the whole experimental procedure from building the quantum circuit to obtaining the fidelity result.

apply the MEM method introduced in Subsection 2.3.2.1 to reduce errors implicit in the measurement process within the device. The MEM method is applied to three physical qubits of the quantum device, where these physical qubits will be utilized as the three router qubits in the transpiled circuit. After the application of the MEM, we implement QST to reconstruct ρ; with the known ρ and ρ' we then calculate the fidelity F.

3.2.2 Experimental Results

Each circle in Fig. 3.5 represents an outcome averaged over ten repetitions, with an error bar indicating two standard deviations from the mean. Note that we have checked the experiments with more repetitions and found that the results are effectively the same. The experimental F indicates the difference between the theoretical density matrix of the router output and the corresponding experimental density matrix, as mentioned above. The state of the router output is fixed by the chosen state of the signal qubit and the fixed state of the control qubits. We see from Fig. 3.5(a) that the quantum router with the error correction is feasible when $\gamma \geq 0.5$ on the quantum device. Note, a baseline is the case where no noisy channel and no error correction is applied, for which the fidelity of the quantum routing is 0.85 (non-unity as a consequence of intrinsic errors within the device). For current NISQ devices, quantum error correction introduces more qubits and quantum operations, incurring higher intrinsic errors within the device and making error correction unfeasible. However, we note that the error correction improves the performance of the quantum routing within the range of $\gamma \geq 0.5$, as the error-corrected results in this range are significantly above the ones without the error correction. We do emphasize, that in this range where the error correction partially works, we are not eliminating the noise in the channel, just reducing it. That is, we do not correct fully back to the baseline case. When $\gamma < 0.5$, the experimental F is decreased after the error correction. The reason of this phenomenon is that the noise induced by our noisy quantum channel is smaller than the noise accumulated from the quantum gates. We note that there remains a small probability that this situation observed at low γ is an

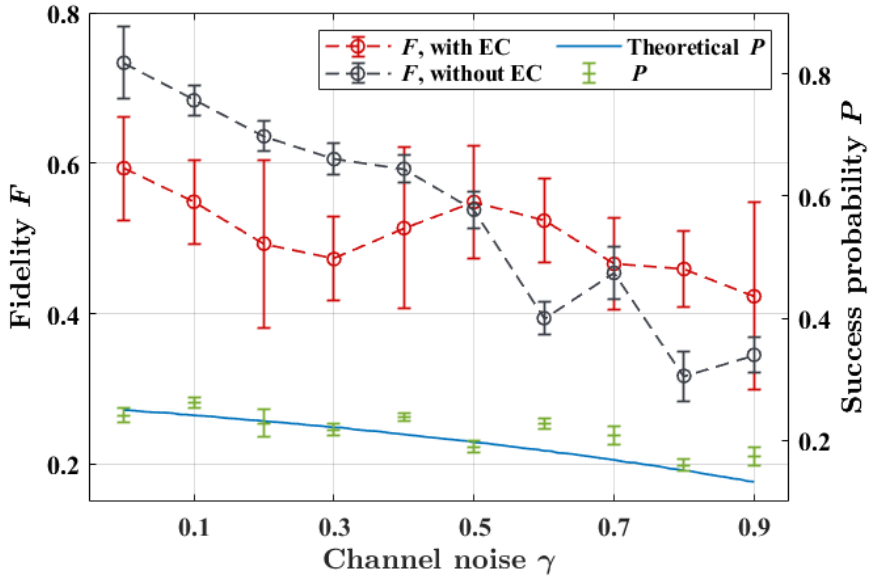

(a)

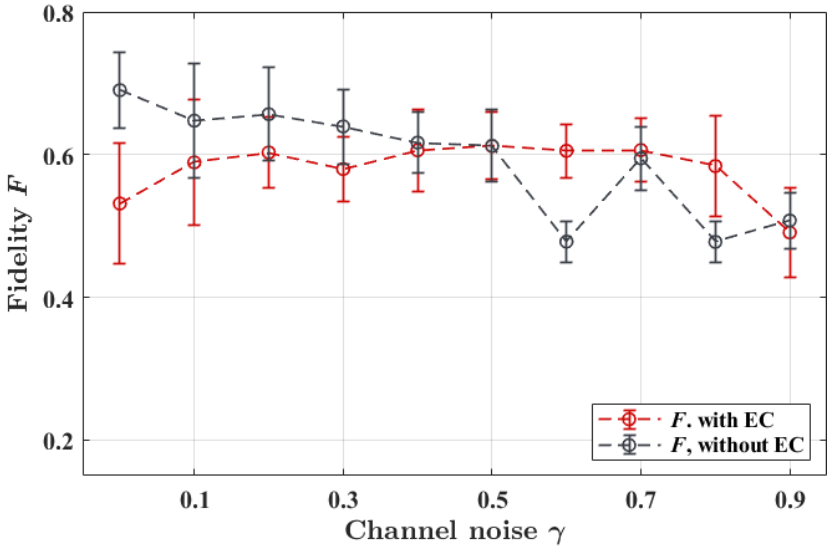

(b)

Figure 3.5: Fidelity, F, as a function of γ with $\gamma_g = 0.5$, where the noisy quantum channel and the error correction are performed on $|\phi\rangle_c$ and $|\phi\rangle_s$ (a); or only performed on $|\phi\rangle_s$ (b). Note, EC represents error correction.

artifact of experimental noise as evidenced by the error bars shown. The observed overall trend of F with γ is as expected - the quantum channel introduces more noise for larger γ and the device performs the error correction less efficiently as the noise increases.

Beyond fidelity, we utilize success probability P of the whole procedure (quantum-error-corrected quantum routing) as another performance metric, as shown (right-hand scale) in Fig. 3.5(a). As the noisy quantum channel and the error correction are implemented on two qubits ($|\phi\rangle_c$ and $|\phi\rangle_s$), P should be square of p_2. Remind that p_2 is the success probability of the error correction for a noisy qubit derived earlier and the quantum routing process is deterministic. We can observe that higher γ results in lower P and F, where the experimental P is consistent with the theory. The success probability, P, decreases with the increase of γ and approaches 0 as $\gamma \to 1$, which indicates a tradeoff between P and the error correction. We also consider the scenario where the noisy quantum channel and the error correction are implemented only on $|\phi\rangle_s$, the results of which are shown in Fig. 3.5(b). We can see that the error correction appears feasible when γ is larger than 0.6.

Finally, the quantum nature of the router is demonstrated by the entanglement generated at the output. We verify the entanglement by reconstructing its density matrix via QST, the results of which are in Fig. 3.6. The theoretical density matrix, ρ', is demonstrated in Fig. 3.6(a) and Fig. 3.6(b), and the experimental ρ with the noisy quantum channel and error correction implemented on $|\phi\rangle_s$ only, with $\gamma = 0.6$ and $\gamma_g = 0.5$, is illustrated in Fig. 3.6(e) and Fig. 3.6(f). For comparison, we also demonstrated ρ without the error correction after the noisy quantum channel performed, with $\gamma = 0.6$, on $|\phi\rangle_s$ (Fig. 3.6(c) and Fig. 3.6(d)). From the comparison of these figures, the good performance of the error-corrected quantum routing is verified - the corrected state clearly being closer in its matrix elements to the theoretical density matrix elements. Detailed information on the values of these elements can be seen from the range of values shown, and fidelities between the matrices determined. It can be found that F improves from 0.48 to 0.61 after the error correction.

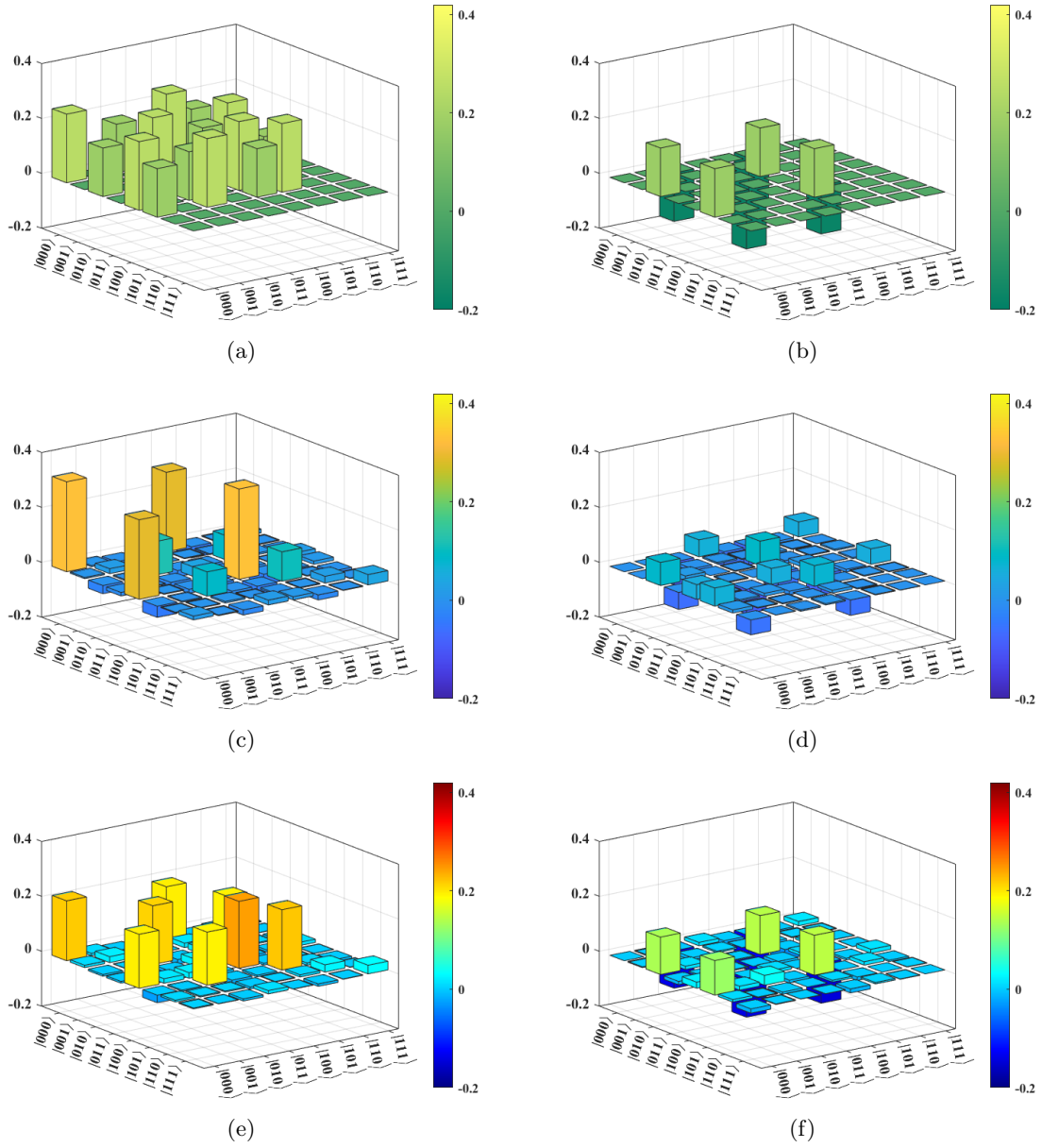

Figure 3.6: Theoretical and experimental density matrices of $|\Phi\rangle_f$, the entanglement generated at the output of the quantum router. (a), (b) represent the real and imaginary parts of the theoretical density matrix, ρ', respectively. (c), (d) together represent ρ without the error correction after the noisy quantum channel performed on $|\phi\rangle_s$ only. Similarly, (e) and (f) depict ρ with the noisy quantum channel and error correction applied on $|\phi\rangle_s$.

3.3 Summary

In this chapter, we designed and experimentally demonstrated a quantum router embedded with a quantum error correction scheme. Via QST, we verified the quantum nature of the router and the impact of the error correction on the routing performance. Our results demonstrate that quantum routing with embedded quantum error correction is viable in near-term noisy devices - pointing the way toward the inclusion of quantum routing in quantum networks. Although we have used a specifically designed noisy channel, our work demonstrates that with the use of statistical information only, quantum-error-corrected routing is viable in NISQ devices. The inclusion of quantum routing within near-term quantum networks will enhance the functionality of such networks, allow for the deployment of RAM, and provide a pathway to the development of additional network functionality.

Chapter 4

Error-Corrected Quantum Routing

In Chapter 3, we have experimentally implemented a quantum router with an error correction technique designed for a specific noise model. The experimental results have showed, however, that the error correction technique, in the context of quantum routing, was only useful for very specific quantum channels—rendering it of no value for generic (or unknown) channel conditions. In this chapter, we utilize a more sophisticated error correction technique. Specifically, we embed a robust QECC within the quantum router that can correct for any single qubit error, independent of the quantum noise model. As we shall see, although such error correction is not viable on current low-complexity NISQ devices provided by the IBM Quantum platform, our work highlights the pathway forward to more robust error-corrected quantum routing. Our novel contributions in this chapter are as follows.

(i) We benchmark quantum routing performance using a currently available 7-qubit NISQ device, assuming noiseless quantum signals.

(ii) Using such quantum routing, we then implement a viable QRAM.

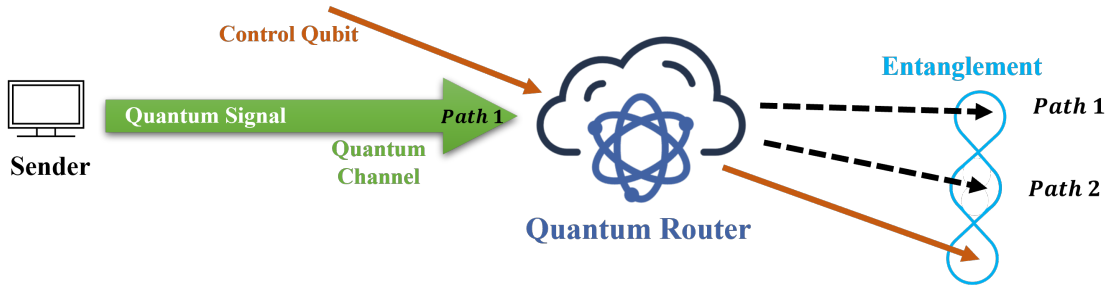

Figure 4.1: Schematic diagram illustrating the principle of a quantum router. A sender prepares and sends a quantum signal to the quantum router via a quantum channel, and a control qubit directs the quantum signal's path based on the control information it stores. The output of the quantum router is an entanglement between the control qubit and the two paths.

(iii) We then evaluate the performance of a quantum router embedded within a 5-qubit QECC suitable for any single-qubit error channel. In doing this, we consider the intrinsic errors as well as errors that mimic the effects of a noisy quantum channel.

(iv) With regard to the quantum error-corrected routing performance of NISQ devices, we experimentally demonstrate the significance of minimizing the number of control gates utilized, and identify the importance of the qubit-coupling map of superconducting quantum devices for realizing a quantum routing process over noisy channels.

4.1 Quantum Routing with an Error-Correcting Code

4.1.1 Quantum Routing

A schematic diagram of the principle of a quantum router with a sender is shown in Fig. 4.1, and a quantum circuit of the quantum router with QST is shown in Fig. 4.2—henceforth, we refer to this circuit as the "router circuit." The working principle of the quantum router and the specific states we utilized for $|\phi\rangle_c$, $|\phi\rangle_s$ and $|\phi\rangle_n$ are provided in Subsection 3.1.1. We still use the fidelity, F, between ρ and ρ' as our performance metric, as shown in Eq. (3.10). Note that $\rho' = |\Phi\rangle_f\langle\Phi|$ is the theoretical density matrix of the

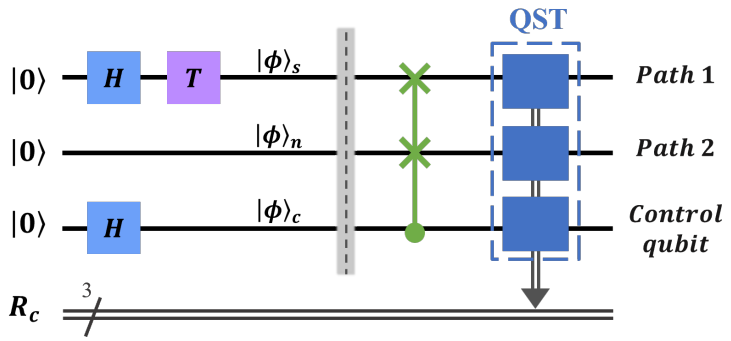

Figure 4.2: Quantum circuit of a quantum router with QST. H stands for the Hadamard gate, and T is the phase gate that introduces a $\pi/4$ phase. All qubits start from the $|0\rangle$ state, and the second qubit initially is $|\phi\rangle_n = |0\rangle_n$. The 3-qubit gate in purple is the CSWAP gate, which exchanges the two quantum states (represented by the two crosses) when the control qubit (represented by the solid circle) is in the $|1\rangle$ state. The density matrix of the quantum router's output is reconstructed via the QST. R_c represents a classical register that contains the quantum measurement results of the QST.

router output, and ρ is reconstructed via QST (see Subsection 2.1.3) in experiments.

Fig. 4.3 shows a distribution of the fidelity between ρ and ρ_r, determined from Eq. (3.10), where ρ_r is a 3-qubit system uniformly sampled from the space of all possible 3-qubit systems. Here, we used the fact that a generic 3-qubit state can be expressed with only 5 terms with the help of the canonical 5-term decomposition, that is,

$$|\Delta\rangle = \alpha_0|000\rangle + \alpha_1 e^{i\vartheta}|100\rangle + \alpha_2|101\rangle + \alpha_3|110\rangle + \alpha_4|111\rangle, \tag{4.1}$$

where $\sum_{j=0}^{4}\alpha_j^2 = 1$ and $\alpha_j, \vartheta \in \mathbb{R}$. Note that $\vartheta \in (0, \pi)$ is a phase term [139]. From this, we see that the probability of randomly selecting a state with $F > 0.5$ is less than 1.25%. As an additional comparison, we note the averaged fidelity between ρ and a 3-qubit product state uniformly sampled from $\{|000\rangle, |001\rangle, \cdots, |111\rangle\}$, is $F = 0.125$.

4.1.2 Quantum Random Access Memory

The quantum router directs the signal qubit along the two paths in a coherent superposition, a process that can be utilized for QRAM. As opposed to classical RAM, QRAM

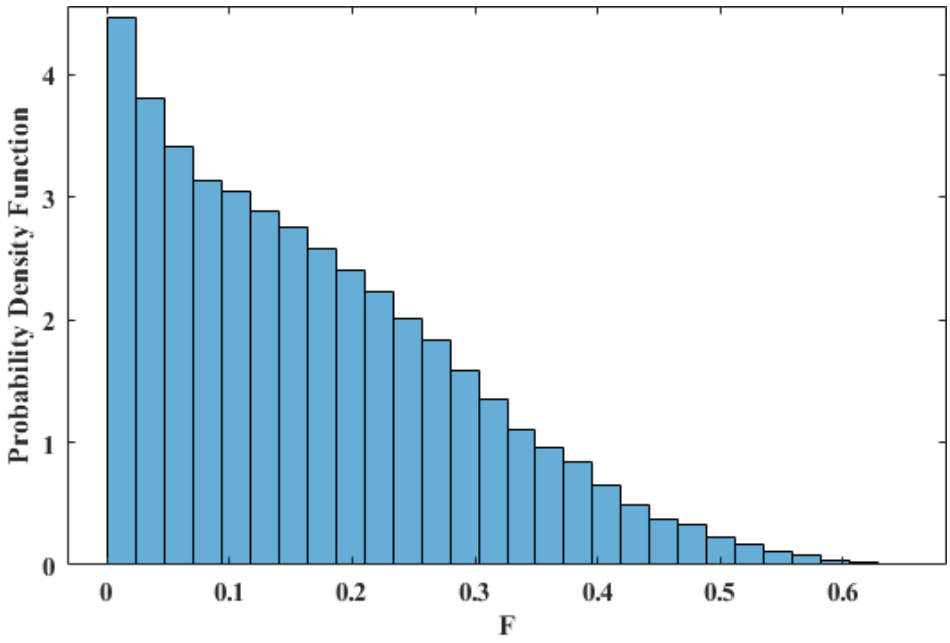

Figure 4.3: Probability density function of F between ρ and ρ_r obtained from 100,000 samples.

can access the information stored in memory in superposition. There are mainly two QRAM structures: the conventional fanout structure [140] and the "bucket brigade" structure [79]. In the fanout QRAM, each "address" qubit changes the states of all "routing nodes" that constitute a binary tree architecture.[1] The routing nodes are qubits used for the decision-making in the binary tree architecture to access memory elements (see [141]). The fanout QRAM is vulnerable to decoherence errors due to its working principle, limiting its scalability. In contrast, the bucket brigade QRAM has a higher noise resistance than the fanout QRAM since the address qubits only change the states of the routing nodes needed for accessing memory elements [81,82]. The structure of a bucket brigade QRAM with two memory cells is illustrated in Fig. 4.4(a). Each memory cell can store either a classical bit or a qubit. The binary tree node makes a binary decision based on the address qubit received: the left (right) memory cell will be

[1]The binary tree architecture is a widely used data structure for RAM and it maintains binary relationships among memory elements.

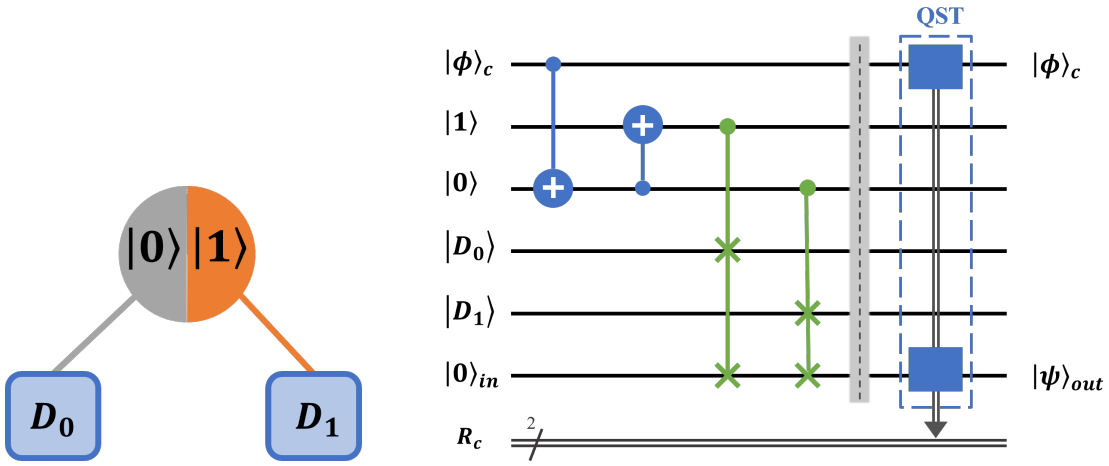

(a) (b)

Figure 4.4: (a) Illustration of the structure of bucket brigade QRAM with two memory cells, D_0 and D_1. (b) Quantum circuit of the QRAM that includes two memory cells with QST. The 2-qubit gate is the CX gate, the 3-qubit gate is the CSWAP gate, and the dashed blue outline indicates the QST process.

accessed if the address qubit is $|0\rangle$ ($|1\rangle$).

Based on the circuit for the bucket brigade QRAM in [141], we design a quantum circuit of our QRAM (the "QRAM circuit") with one address qubit and two memory elements, as shown in Fig. 4.4(b). In our QRAM, what was termed previously as the control qubit and is now referred to as the address qubit, $|\phi\rangle_c$, which is a superposition of two addresses ($|0\rangle$ and $|1\rangle$). The two qubits initialized to the $|1\rangle$ and $|0\rangle$ states are the routing nodes (referred to above) that help to access the memory elements, $|D_0\rangle$ and $|D_1\rangle$, storing bits or qubits. We use the last qubit initialized as $|0\rangle_{in}$ in the QRAM circuit to store the accessed memory elements. We define that the input and the output of our QRAM is $|\Psi\rangle_{in}$ and $|\Psi\rangle_f$, respectively, which can be expressed as

$$|\Psi\rangle_{in} = |\phi\rangle_c|0\rangle_{in} \xrightarrow{\text{QRAM}} |\Psi\rangle_f = |\phi\rangle_c|\psi\rangle_{out} = \alpha_c|0\rangle_c|D_0\rangle_{out} + \beta_c|1\rangle_c|D_1\rangle_{out}. \tag{4.2}$$

4.1.3 Five-Qubit Quantum Error-Correcting Code

The QECC code we adopt is that of [142], which encodes the quantum signal by 5 qubits, requires no post-selections or stabilizer measurements. The best-known 5-qubit QECC is the [[5,1,3]] code (see Subsection 2.3.1.2), which requires not only 5 qubits for encoding but also four ancillary qubits for stabilizer measurements (requires nine qubits in total). The 5-qubit QECC [142] utilized for this research only requires 5 qubits in total, and it permits corrections of generic single-qubit errors. A quantum circuit of the QECC (the "QECC circuit") embedded within the quantum router is demonstrated in Fig. 4.5. The first five qubits (counting from the top) in the QECC circuit are utilized for an encoding logic given by

$$\begin{aligned} |0\rangle_L = \frac{1}{\sqrt{8}} (&|00000\rangle - |01111\rangle - |10011\rangle + |11100\rangle \\ &+|00110\rangle + |01001\rangle + |10101\rangle + |11010\rangle) \quad \text{and} \\ |1\rangle_L = \frac{1}{\sqrt{8}} (&|11111\rangle - |10000\rangle + |01100\rangle - |00011\rangle \\ &+|11001\rangle + |10110\rangle - |01010\rangle - |00101\rangle) . \end{aligned} \tag{4.3}$$

The encoded qubit is the third qubit in the QECC circuit, which is prepared as $|\phi\rangle_s$ before the encoding. After the encoding, the five qubits are sent to the quantum router via a noisy quantum channel, which introduces a generic single-qubit error. We utilize a unitary transformation to represent this single-qubit error, and in this chapter, we redefine U as this transformation, where U is given by

$$U = \begin{bmatrix} c_0 & c_1 \\ c_2 & c_3 \end{bmatrix} = \frac{c_0 + c_3}{2} I + \frac{c_1 + c_2}{2} X + \frac{c_2 - c_1}{2i} Y + \frac{c_0 - c_3}{2} Z, \tag{4.4}$$

where c_0, c_1, c_2, and c_3 are complex numbers and satisfy the requirements of a unitary matrix.

Once the quantum router receives the qubits, it realizes the error-finding, error-correction, and quantum-routing processes. After the error-finding process, quantum measurements should be applied to the first, second, fourth, and fifth qubits to find

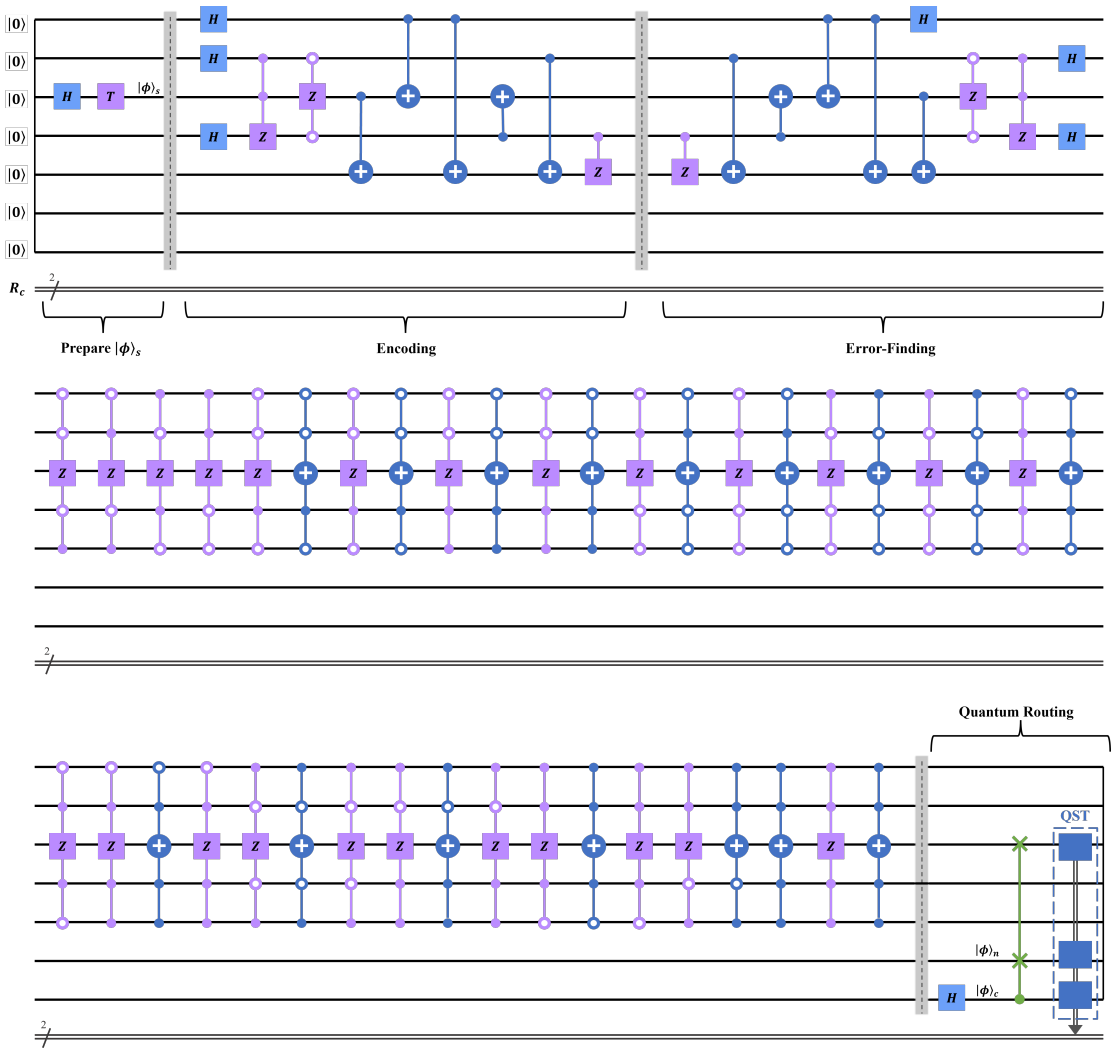

Figure 4.5: Quantum circuit of the 5-qubit QECC embedded within the quantum router with QST. The first part of this quantum circuit is the state preparation of $|\phi\rangle_s$ on the third qubit (counting from the top), followed by the encoding, error-finding, error correction, and quantum routing. The first five qubits, except for the third qubit, are ancillary qubits for encoding, the sixth qubit is $|\phi\rangle_n$, and the last qubit is prepared as $|\phi\rangle_c$. Note that Z stands for the Z gate, the 2-qubit gate with two solid circles is the CZ gate. The 3-qubit and the 5-qubit gates are either a multi-CX or a multi-CZ gate, whose solid and hollow circles indicate that the control state is the $|1\rangle$ or $|0\rangle$ state, respectively. Note that the row being continued across the three blocks is the continuation of the previous row.

syndromes that indicate the exact error that occurred on any of the five qubits, as summarized in Table 4.1. However, due to the limitations of current 7-qubit superconducting quantum devices, we cannot apply quantum gates based on the quantum measurement results. Instead, we implement multi-controlled gates conditioned on the states of those four qubits, as shown in Fig. 4.5. Note that the multi-controlled gates realizing the error correction process are equivalent to applying the X and Z gates on the third qubit conditioned on the measurement results of the four qubits [143].

The sixth qubit is $|\phi\rangle_n$, and the last qubit is prepared as $|\phi\rangle_c$ by the Hadamard gate. Upon completing the quantum routing process, we implement QST (see Subsection 2.1.3) on the third and the last two qubits to reconstruct ρ, thereby allowing us to determine F.

4.2 Experimental Results

4.2.1 Quantum Routing without Error Correction

Our experiments are implemented on the 7-qubit *ibmq_jakarta*, and all the above quantum circuits are designed via Qiskit [67]. Executing a circuit on a quantum device requires the transpilation process (see Subsection 2.2.2.2), and we refer to the circuit after the transpilation as a "transpiled" circuit. The general transpilation process includes steps which are stochastic in nature, e.g., the number of gates resulting from the transpilation. However, it is possible to generate reproducible and deterministic transpiled circuits, and we adopt this approach here (ensuring the minimum number of CX gates are used). In addition, all measurement results returned from the quantum device are first processed the MEM method (see Subsection 2.3.2.1) so as to mitigate measurement errors, one type of intrinsic error.

To benchmark the performance of the quantum router on *ibmq_jakarta*, we implement two quantum routing experiments that verify the quantum nature of the quan-

Table 4.1: Syndrome Table with Error Correction Operations

Syndromes (Error Type [1])	**Quantum State before Error Correction [2]**	**Error Correction [3]**
$0001(X_2)$, $0101(Y_2)$, $1010(Z_3)$, $1100(Z_5)$	$\alpha_s\|0\rangle_s - \beta_s\|1\rangle_s$	Z_3
$1000(Z_1)$, $0100(Z_2)$, $0010(Z_4)$, $0011(X_5)$	$-\alpha_s\|0\rangle_s - \beta_s\|1\rangle_s$	$Z_3X_3Z_3X_3$
$0110(X_1)$, $1110(Y_1)$, $0111(X_3)$, $1011(X_4)$, $1001(Y_4)$	$-\alpha_s\|1\rangle_s - \beta_s\|0\rangle_s$	$Z_3X_3Z_3$
$1101(Y_3)$	$-\alpha_s\|1\rangle_s + \beta_s\|0\rangle_s$	Z_3X_3
$1111(Y_5)$	$-\alpha_s\|0\rangle_s + \beta_s\|1\rangle_s$	$X_3Z_3X_3$

[1] When representing errors, X_j, Y_j, and Z_j, where $j \in \{1, 2, 3, 4, 5\}$, denote the X, Y, and Z-type errors, respectively, that occur on the jth qubit in the QECC circuit. Note that no error occur when the syndromes are 0000.

[2] The quantum state of the third qubit in the QECC circuit after the error-finding.

[3] Here, X_3 and Z_3 represent the X and Z gates applied to the third qubit for correction, respectively.

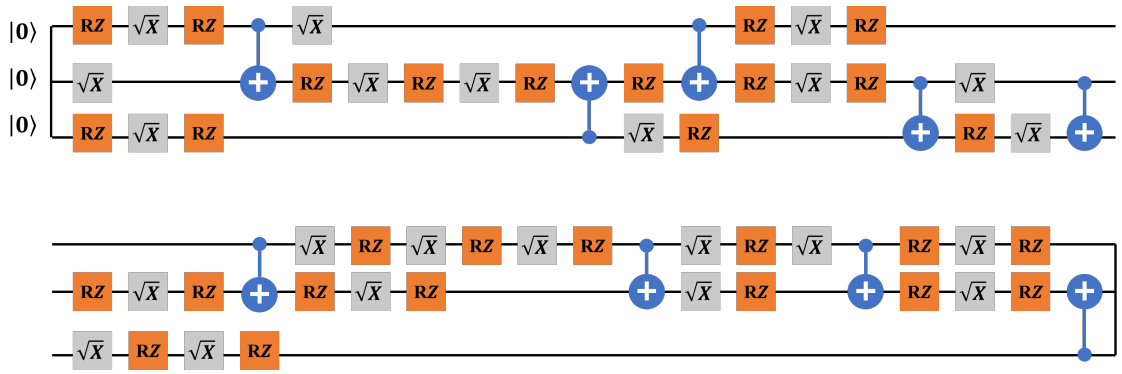

Figure 4.6: A transpiled circuit of the router circuit. Note that QST is not included here, and 9 CX gates are involved. The quantum gates included in this transpiled circuit are basis gates that can be physically operated on *ibmq_jakarta*.

tum router and the preservation of $|\phi\rangle_s$, respectively. We refer to these experiments as "*Experiment-1*" and "*Experiment-2*," respectively, and we assume that the quantum channel introduces zero noise in these two experiments, which means that only the intrinsic errors of *ibmq_jakarta* are included. In *Experiment-1*, we execute the router circuit to confirm the quantum nature by experimentally demonstrating the generation of $|\Phi\rangle_f$. The transpiled circuit of the router circuit is demonstrated in Fig. 4.6, and it includes 9 CX gates. To conduct QST, 27 copies of the transpiled circuit are generated, each with a distinct projective measurement (see Subsection 2.1.3). We refer to one single execution of a circuit as one "shot". That is, when a circuit executes 100 shots, say, the circuit is executed 100 times. The transpiled circuit executes 100,000 shots for each projective measurement, which is the maximum number of shots for *ibmq_jakarta*. The results of the projective measurements returned from *ibmq_jakarta* are first processed by the MEM method and then utilized for calculating F. The entire procedure from the transpilation to the calculation of F is referred to as a "run." Several runs with the same transpiled circuit are taken, from which the averaged F is adopted as our performance metric.

The comparison of ρ and ρ' is demonstrated in Fig. 4.7. Here, after ten runs, an average $F = 0.85$ is determined. Note that this fidelity result is calculated with the

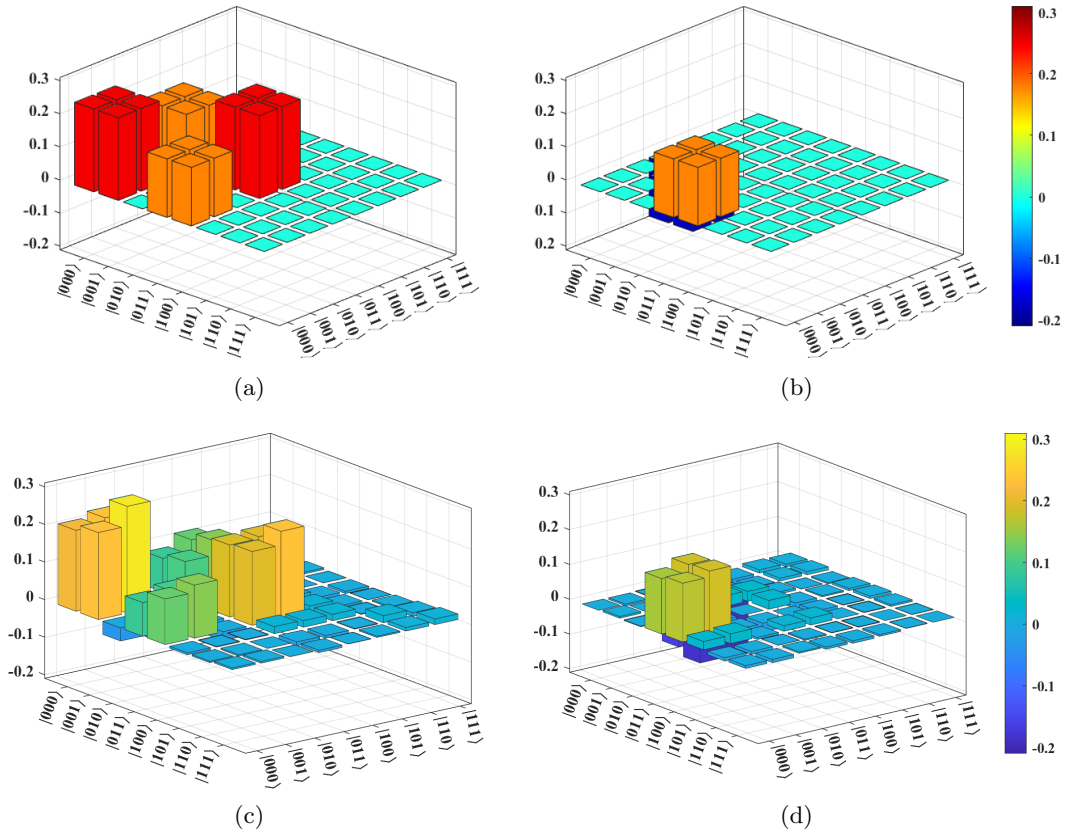

Figure 4.7: Theoretical and experimental density matrices of $|\Phi\rangle_f$. (a), (b) represent the real and imaginary parts of ρ', the theoretical density matrix of $|\Phi\rangle_f$, respectively. (c), (d) show the real and imaginary parts of ρ, the experimental density matrix of $|\Phi\rangle_f$, respectively. The entanglement fidelity, F, between ρ and ρ' is 0.85.

specific output state of the quantum router, as we have selected a specific state for the signal qubit. We have tested other signal states and observed similar experimental outcomes. Therefore, although the experimental result is state-dependent, the fidelity result remains representative. We conclude that the two output paths of the quantum router are entangled, and the quantum nature is verified on the quantum device. We emphasize that four specific experimental setups help improve the performance of *ibmq_jakarta*. These are the following: (i) We chose three physically connected qubits (qubits labeled by 0, 1, and 3 in Fig. 4.8(a)) of the quantum device with the lowest 1-qubit and 2-qubit

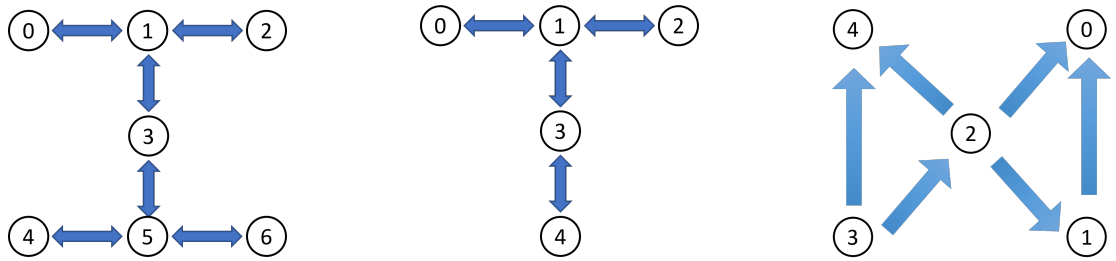

(a) (b) (c)

Figure 4.8: Coupling maps of *ibmq_jakarta* (a), *ibmq_quito* and *ibmq_belem* (b), and *ibmqx4* (c). The two-way arrows in (a) and (b) represent that the CX gate can be implemented between the two pointed qubits in both directions. The one-way arrows in (c) indicate that the CX gate can only be implemented in one direction (the arrowheads point to the target qubits). In the connected qubit pair labeled by 0 and 1 in (c), for example, qubit 1 can only act as the control qubit of the CX gate with the qubit 0 as the target qubit.

error rates to implement *Experiment-1*.[2] (ii) We utilized the transpiled circuit with the lowest number of CX gates. (iii) We executed the transpiled circuit with the maximum shots. (iv) The MEM method was applied to the data returned from the quantum device.

As the errors in 2-qubit gates and 1-qubit gates are of the order 10^{-2} and 10^{-4}, respectively, optimizing the number of CX gates is a helpful way to reduce quantum gate errors [144]. We implement the quantum router with another transpiled circuit which includes 14 CX gates instead of 9 CX gates, and with other experimental setups unchanged, we find that F decreases to 0.68. This phenomenon emphasizes the significance of lowering the number of CX gates with regard to routing performance. We also note that F drops from 0.85 to 0.79 if the MEM method is removed, highlighting the importance of this step.

We now review the preservation of the quantum signal. *Experiment-2* utilizes the router circuit but with a slight modification: the control qubit is set as $|\phi\rangle_{c'} = |1\rangle_c$ by applying an X gate instead of the Hadamard gate on the $|0\rangle$ state. Moreover, a 1-qubit

[2]The quantum device, *ibmq_jakarta*, is calibrated daily, and the error rates may change over time.

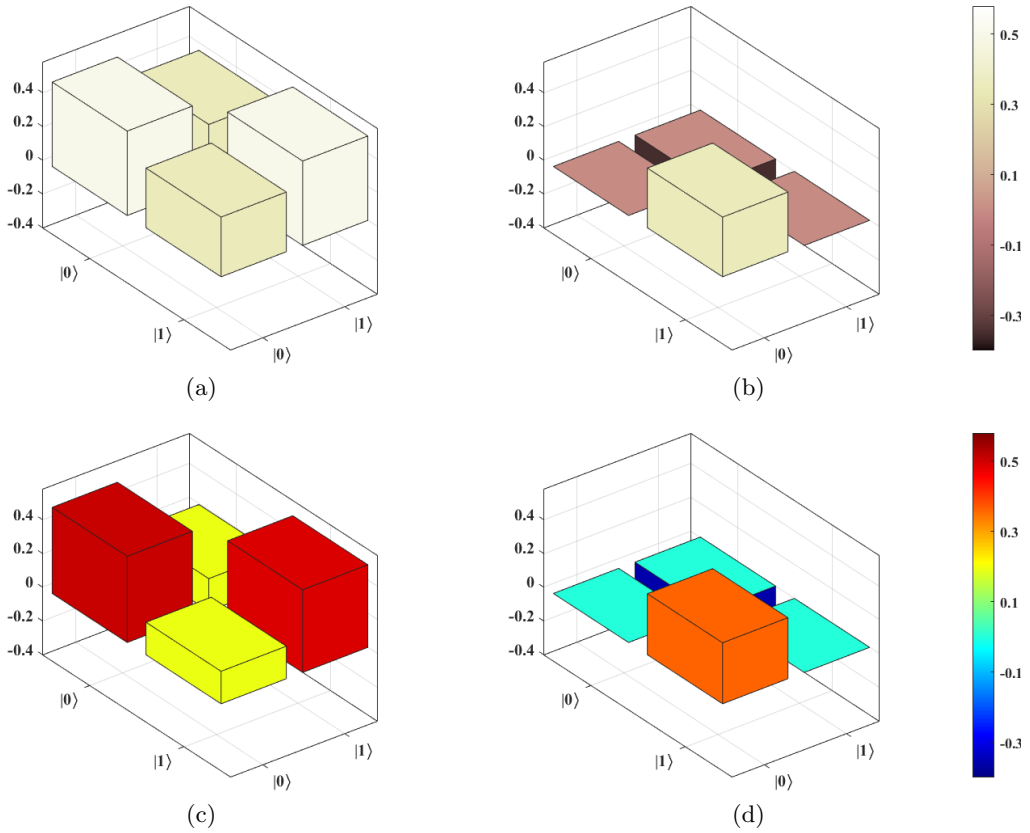

Figure 4.9: Theoretical and experimental density matrices of $|\phi\rangle_s$ after the quantum routing process with $|\phi\rangle_{c'} = |1\rangle_c$. (a), (b) represent the real and imaginary parts of ϱ', the theoretical density matrix of $|\phi\rangle_s$, respectively. (c), (d) show the real and imaginary parts of ϱ, the experimental density matrix of $|\phi\rangle_s$, respectively. The state fidelity, F_s, between ϱ' and ϱ is 0.89.

QST is applied to the qubit in path 2 to check whether its state is $|\phi\rangle_s$. We use the state fidelity F_s as our performance metric, where F_s is given by

$$F_s = \left(\mathrm{Tr} \sqrt{\sqrt{\varrho}\ \varrho' \sqrt{\varrho}} \right)^2 . \tag{4.5}$$

We refer to $\varrho' = |\phi\rangle_s\langle\phi|$ as the theoretical density matrix of $|\phi\rangle_s$ and ϱ as the experimental density matrix of $|\phi\rangle_s$ reconstructed by 1-qubit QST. Similar to our previous discussion, the modified router circuit is transformed into a transpiled circuit with 9 CX gates. Note that F_s is averaged from ten runs and is found to be 0.89, as demonstrated in Fig. 4.9. This result implies that the quantum signal is well preserved after the quantum routing

process on *ibmq_jakarta*.

We return to the full implementation of the quantum router (*Experiment-1*) on *ibmq_jakarta*, whose coupling map is illustrated in Fig. 4.8(a), and where we obtained an averaged result of $F = 0.85$. However, Behera et al. [74] demonstrated a quantum router on the *ibmqx4* (its coupling map is shown in Fig. 4.8(c)) and obtained an F of approximately 0.98. We name their router the "BRGP" router to differ from our router shown in Fig. 4.2, as these two routers utilize different quantum states and devices. The BRGP router sets the control and signal qubits in states $(|0\rangle_c - e^{i\pi/4}|1\rangle_c)/\sqrt{2}$ and $\cos(\pi/8)|0\rangle_s + \sin(\pi/8)|1\rangle_s$, respectively. The control qubit is prepared by sequentially applying the H, S, T, and S gates on the $|0\rangle$ state. Similarly, the signal qubit is prepared by sequentially implementing the H, T, H, and S gates on the $|0\rangle$ state. The BRGP router defines that $|\phi\rangle_n$ is in the $(|0\rangle_n + |1\rangle_n)/\sqrt{2}$ state. In contrast, in the router of Fig. 4.2, we set $|\phi\rangle_n = |0\rangle_n$, meaning that it is an ancillary qubit without any information in the quantum router. As *ibmqx4* is retired, we reproduce the BRGP router on *ibmq_quito* and *ibmq_belem*, which are 5-qubit quantum devices sharing a coupling map (as shown in Fig. 4.8(b)) close to *ibmqx4*'s map. The experimental results we obtained from *ibmq_quito* and *ibmq_belem* were $F = 0.85$ and 0.79, respectively. Thus, we conclude that $F = 0.85$ obtained in *Experiment-1* is close to the best outcome for a quantum router built using currently available small-qubit superconducting quantum devices.

The disparity of F between 0.85 and 0.98 likely demonstrates the importance of the coupling map for the quantum device acting as the quantum router. The coupling map of *ibmqx4* ensures that every qubit is connected to two or four qubits, and we can find that qubits 0, 1, and 2 (same for qubits 2, 3, and 4) are connected to each other. The CSWAP gate is a 3-qubit quantum gate that realizes the quantum routing process, which therefore benefits from this topology. We also note that in this topology, the CX gate can only be implemented in one way on *ibmqx4* (see Fig. 4.8). However, this disadvantage is somewhat compensated by the fact that on *ibmqx4* topology, an

inverse-CX gate can be implemented (by adding 4 Hadamard gates [145]). Even though *ibmq_quito* and *ibmq_belem* can implement the CX gate in both directions, they do not have a similar 3-qubit topology, which leads to the implementation of the CSWAP gate requiring multiple swap gates during the transpilation. The introduction of swap gates causes extra quantum gate errors, thus decreasing the performance of the quantum router. In summary, having a coupling map with at least 3 qubits physically connected is significant for a superconducting quantum device that hopes to act as the quantum router.

Additionally, we implement another experiment ("*Experiment-3*") that executes the QRAM circuit. We first consider the case where the memory stores quantum information, which means that $|D_0\rangle$ and $|D_1\rangle$ are set as two arbitrary qubits. We utilize the fidelity F' as our performance metric, where F' is given by

$$F' = \left(\mathrm{Tr} \sqrt{\sqrt{\kappa}\ \kappa' \sqrt{\kappa}} \right)^2 . \tag{4.6}$$

We refer to $\kappa' = |\Psi\rangle_f \langle\Psi|$ as the theoretical density matrix (no errors) of $|\Psi\rangle_f$ and κ as the experimental density matrix of $|\Psi\rangle_f$ reconstructed by QST. The experimental result is $F' = 0.86$, which is an averaged result from ten runs. This result indicates that QRAM with quantum memory is feasible on current small-qubit NISQ devices. We next consider the case where the memory stores classical information. In this case, the experimental result is slightly higher ($F' = 0.88$) than the quantum case since fewer basis gates are required for initializing the memory elements $|D_0\rangle = |1\rangle$ and $|D_1\rangle = |0\rangle$. Entanglement distillation protocols are designed so that higher entanglement can be created from an ensemble of states possessing lower entanglement [146,147]. The experimental results for our QRAM, F', are all above 0.5, which is high enough to implement a viable distillation process. Therefore, we conclude that our QRAM is viable.

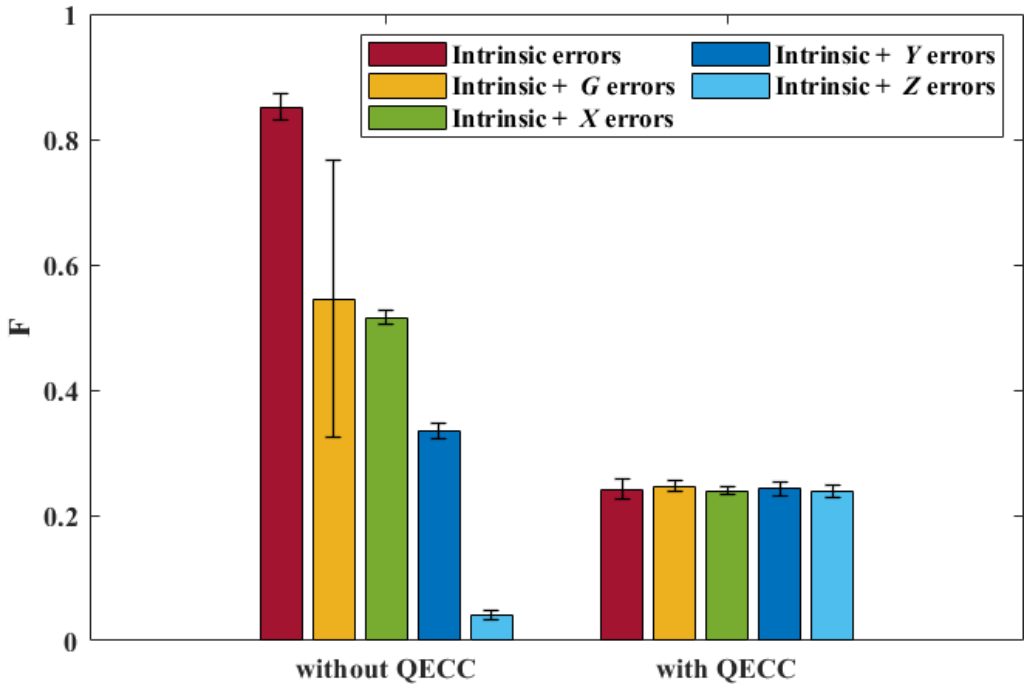

Figure 4.10: F of the quantum router without and with the QECC.

4.2.2 Quantum Routing with the Error-Correcting Code

We now implement an experiment that executes the QECC circuit—we refer to this experiment as "*Experiment-4*." Although we will find, not surprisingly, that full-blown QECC for quantum routing is not feasible on *current* small-qubit superconducting NISQ devices, our results highlight the pathway towards error-corrected versions of quantum routing.

The transpiled circuit of the QECC circuit has thousands of CX gates and is too complex to illustrate here. Due to the long run time in the quantum device for the QECC circuit, we take F averaged from only four runs as our performance metric. While *Experiment-1* implemented the quantum router on the quantum device with intrinsic errors only, *Experiment-4* considers the QECC applied to generic single-qubit errors. We consider a noise model in which a noisy quantum channel introduces one generic single-qubit error that can be represented by U, as explained in Eq. (4.4). In this noise

model, $U \in \{G, X, Y, Z\}$, where in this chapter, G is a 2×2 unitary matrix randomly generated (different in each of the runs). In *Experiment-4*, U is manually applied to $|\phi\rangle_s$ when the QECC is not considered. When the QECC is considered, U is randomly applied to any of the five qubits by codes after the encoding.

The results of *Experiment-4* are demonstrated in Fig. 4.10, where each bar shows the averaged F from four runs (the error bars represent the standard deviation). As we can see, only when $U = Z$ do we find that F is improved after considering the QECC. Indeed, we see that F is effectively constant with the QECC included, no matter which type of errors are included. Focusing on the intrinsic-errors-only bars, this demonstrates that F decreases substantially after introducing the QECC even when only intrinsic errors are present. The reason for this phenomenon is that thousands of basis gates are introduced after the transpilation due to the QECC, and thus, the intrinsic errors (mainly quantum gate errors) accumulate. The transpilation decomposes all of the 5-qubit gates in Fig. 4.5 (those gates taking five qubits as an input) into thousands of basis gates, while the remaining quantum gates only transpile to hundreds of basis gates. Beyond the accumulation of quantum gate errors, decoherence errors also increase due to the introduction of the QECC. The additional execution of the quantum gates required by the QECC extends the time for the signal qubit to be contaminated by the environment, leading to a further loss of quantum information. We conclude that the adopted QECC is not effective when working on current small-qubit superconducting NISQ devices. This is, in part, evidenced by noticing that after introducing the QECC F is only 0.24. The probability of the "comparison" fidelity, discussed earlier, being larger than 0.24 is 27%, as shown in Fig. 4.3.

4.3 Discussion and Summary

Let us summarize our findings regarding QECC. We have shown how quantum routing can be performed, with useful fidelity, on currently available small-qubit NISQ devices—

under the assumption that the quantum signals traversing the network arrive at the router in a noiseless condition. However, we have also shown how correction of arriving noisy quantum signals within the router is plagued by the very large number of CX gates that arise from the transpilation process required to run the QECC circuits alongside the routing circuits. We have provided evidence that a reduction in the number of these gates is the pathway to full-blown QECC quantum routing. In this regard, we note the correction techniques based on self-mitigation via Trotter circuits that several groups have proposed, which indicate that up to 400 CX gates can be run while still retaining useful quantum information in the signal [148–150]. Measurement-conditioned quantum gates are allowed in some higher qubit ($\geq$27) "exploratory" devices provided by the IBM Quantum platform. In these devices, therefore, the 5-qubit gates of our circuits can be removed, leading to a transpilation with much fewer CX gates. Our future work will investigate the use of these techniques within the quantum routing process.

In the experiments of this work, we focused on low-complexity devices since they are likely to be the first to be deployed in real-world quantum networks. However, with a quantum device possessing more qubits, we could potentially bring more benefits for quantum routing schemes. We discuss two of these potential benefits: (i) The quantum router can be extended and generalized to one with more paths. (ii) Different quantum error correction techniques that require a larger number of ancillary qubits can be considered.

Considering (i) above: For a quantum router with N paths, n control qubits are required, where $N \leq 2^n$; and instead of CSWAP gates, multi-CSWAP gates are needed. For example, for a quantum router with four paths, ten qubits are required, including two control qubits, one signal qubit, three ancillary qubits, and four ancillary qubits for the QECC. The principle of a four-path quantum router is similar to the one shown in Fig. 4.1. The quantum signal is injected into the quantum router via path 1, while the output of the quantum router is entangled with the two control qubits and the four paths. To generate the required entanglement, the quantum router applies three

different two-CSWAP gates: an anti-controlled-CSWAP gate, a controlled-anti-CSWAP gate, and a controlled-CSWAP gate.

In this work, we experimentally demonstrated an emerging application of quantum entanglement in the communication space. Specifically, we implemented a quantum router on a low-complexity superconducting quantum device. We first bench-marked the quantum router's performance with all errors being intrinsic to the quantum device only. In comparison with quantum routing on historical NISQ devices, we found that it is critical to have a coupling map that has at least three qubits inter-connected. We also investigated an application of quantum routing—a QRAM implementation—showing its feasibility for both classical and quantum memory states. We then considered noisy quantum signals for evaluating the performance of a five-qubit QECC embedded within the quantum router showing the challenges faced by such error correction. Our research enlightens the usage of QECCs for today's quantum devices and points the way forward to the near-term error-corrected quantum routing within real-world quantum networks.

Chapter 5

Error-Mitigated Quantum Routing

In Chapters 3 and 4, we have demonstrated that quantum error correction is, in general, ineffective on the current IBM quantum devices in the context of quantum routing. In this chapter, we redirect our research to quantum error mitigation, which provides a potential alternate pathway to application deployment - a possibility that has recently attracted widespread attention. We specifically investigate two promising error mitigation methods, ZNE and PEC, along with their concatenation embedded into the quantum router application. We shall see that these quantum error mitigation methods significantly improve the entanglement fidelity of the quantum router - to the point that quantum applications based on quantum routing become effective on current NISQ devices. The main contributions of this Chapter can be summarized as follows.

(i) We use a 7-qubit superconducting quantum device to benchmark the performance of quantum routing via ZNE and PEC separately.

(ii) We further investigate the routing performance of ZNE and PEC in a concatenated form.

(iii) With the quantum error mitigation methods, we explore the performance of QRAM on a NISQ device.

5.1 Quantum Error Mitigation

Before proceeding, let us clarify some necessary variables and notations. Suppose that O is an operator with expectation value $\langle O \rangle$ and discrete eigenvalues $\{a_x,\, x = 1, 2, \cdots, 2^n\}$, each associated with one of the 2^n eigenvectors. Here, n is the number of some qubits (represented by a state $|\psi\rangle$) to be measured by the operator O. In the operational perspective, C_{tot} copies of $|\psi\rangle$ are prepared, and each copy is measured by O. The number of times that a_x is obtained as the result of the measurement is denoted as $C_x \in [0, C_{tot}]$. The frequency of obtaining a_x from a limited number of trials is defined as $F_x = C_x/C_{tot}$. The probability of obtaining a_x with zero finite sampling error is obviously $P_x = \lim_{C_{tot}\to\infty} (C_x/C_{tot})$. Therefore, the expectation value of O with respect to the state $|\psi\rangle$ can be expressed as

$$\langle O \rangle = \lim_{C_{tot}\to\infty} \sum_{x=1}^{2^n} \frac{C_x}{C_{tot}} a_x = \sum_{x=1}^{2^n} P_x a_x. \tag{5.1}$$

In this thesis, we assume $P_x = F_x$. When an eigenvalue or eigenvector is given, we simply use P to represent the probability[1] instead of P_x. Henceforth, we redefine that U is a unitary quantum circuit that contains n' qubits, all of which are initialized in the state $|0\rangle$. Note that $n \leq n'$ and n is the number of the qubits in U to be measured by the operator O.

In this thesis, the "measurement results" of U are referred to the Z-basis measurement outcomes of the n qubits, while the "experimental results" indicate the measurement results obtained from the quantum device. Note that the measurement results

[1]Note that P was used to represent the success probability of the whole quantum error-corrected quantum routing procedure in Chapter 3. In this chapter, P is redefined as the probability of obtaining an eigenvector as the result of the measurement of O.

represent the probabilities of all possible measurement outcomes occurring in C_{tot} measurements.

5.1.1 Overview of Zero Noise Extrapolation

One promising quantum error mitigation method is ZNE [28, 31, 32, 41, 122, 151], which extrapolates zero-noise results from noisy results obtained from ancillary quantum circuits. The main idea of ZNE is to extrapolate the zero-noise expectation value of an operator from noise-scaled circuits at different noise levels [152]. ZNE can be divided into analog and digital ZNE based on the noise-scaling method adopted. Analog ZNE scales the noise by extending the microwave pulse duration (used to execute a gate), while digital ZNE scales the noise via the insertion of additional quantum gates. In this thesis, we consider only digital ZNE.

ZNE involves two main steps: constructing noise-scaled circuits and extrapolating estimated values to a zero-noise level. In digital ZNE, global and local folding are the two main methods utilized for constructing the noise-scaled circuits. Assume that in ZNE, U is an original circuit of interest containing K unitary gates $\{G_k\}_{k=1}^{K}$, where U can be expressed as $U = G_K \cdots G_k \cdots G_2 G_1$. Note that G_k also indicates the specific qubits that are to be applied. To generate the noise-scaled circuits, some of the unitary gates are randomly selected and then noise-scaled following

$$G_k \to G_k \left(G_k^\dagger G_k\right)^\xi, \quad \xi = 0, 1, 2, \cdots. \tag{5.2}$$

This method artificially inserts noise without changing the effect of U since $G_k^\dagger G_k = I$. This noise-scaling method is known as the local folding, and the global folding applies the same folding logic but to the entire quantum circuit: $U \to U \left(U^\dagger U\right)^\xi$.

The noise-scale factors, denoted as $\{\lambda_j\}_{j=1}^{J}$, are utilized to quantify the levels of noise present in J noise-scaled circuits. Specifically, λ_j is defined as the ratio of the number of the unitary gates in the j^{th} noise-scaled circuit to the number of the unitary gates

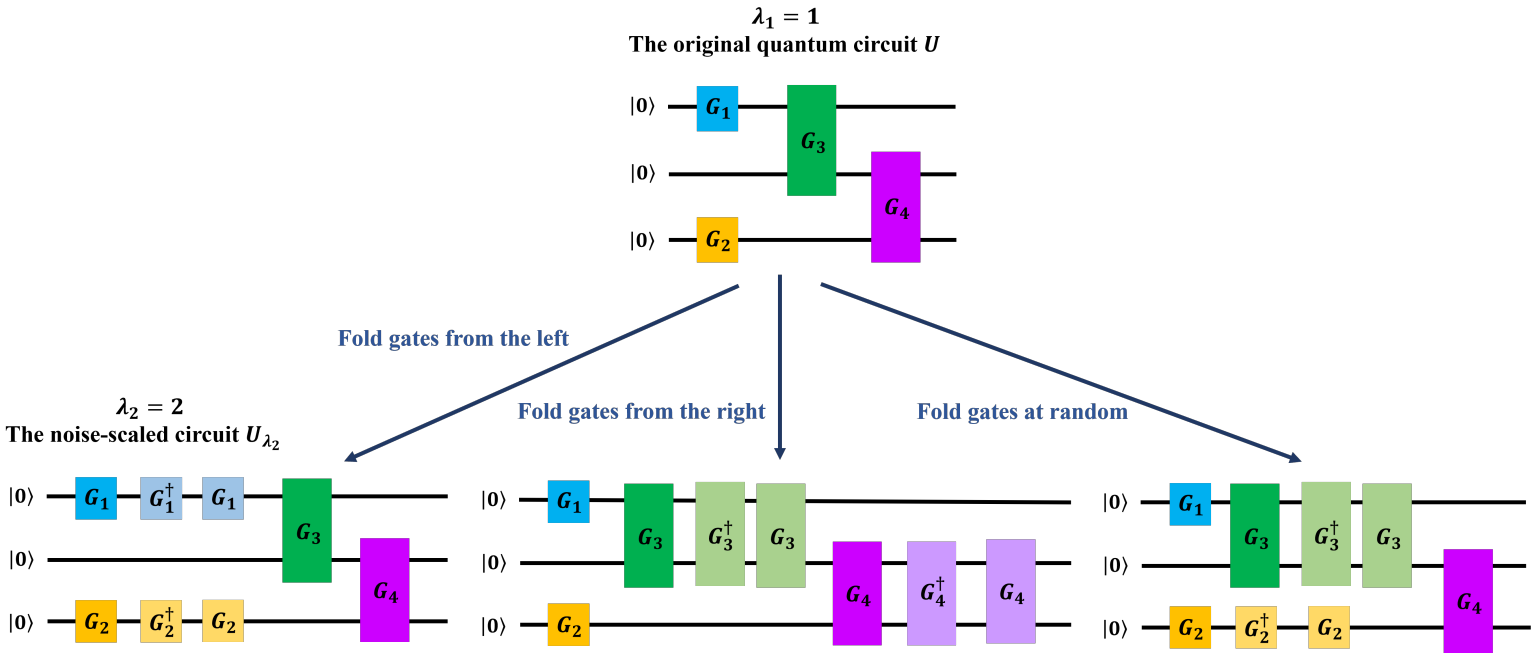

Figure 5.1: Three methods of local folding gates in ZNE. The value of λ decides how many gates should be inserted to extend the strength of the noise. The total number of gates after the insertion should be approximately λ times the number of gates in the unmitigated circuit.

in U. Note that $\lambda_j \geq 1$ and typically, $\lambda_1 = 1$. Suppose that the measurement of O is applied to n qubits of the noise-scaled circuits, denoted as $\{U_{\lambda_j}\}_{j=1}^{J}$, which are executed on the quantum device to collect their measurement results. Note that $U_{\lambda_1} = U$, when $\lambda_1 = 1$. The local folding method involves three approaches for inserting the folding gates to generate U_{λ_j}: from the left, from the right, or at random (see Fig. 5.1). In this thesis, we consider local folding gates at random.

After the execution of the noise-scaled circuits on the quantum device, a total of J noisy expectation values $\{\langle\tilde{O}\rangle_{\lambda_j}^{zne}\}$ are calculated via Eq. (5.1). Extrapolation is then implemented as a post-processing method acting on $\{\langle\tilde{O}\rangle_{\lambda_j}^{zne}\}$, which is the second step of ZNE. Multiple extrapolation models, such as linear extrapolation and polynomial extrapolation, can be considered. The extrapolation models are functions of Λ, where $\Lambda \in \{\lambda_0, \lambda_1, \cdots, \lambda_J\}$ and $\lambda_0 = 0$. These models fit the curve plotted by $\{\langle\tilde{O}\rangle_{\lambda_j}^{zne}\}$ as a function of Λ, and the least squares method is typically utilized to find the best-fit parameters of this function. By evaluating the function at $\Lambda = \lambda_0$, the zero-noise expectation value $\langle\hat{O}\rangle_{\lambda_0}^{zne}$ can be found, as shown in Fig. 5.2.

The critical assumption of ZNE is that the noise in the quantum device can be described by the noise-scale factors, $\{\lambda_j\}$. This implies that incoherent errors are the dominant type of noise and other types of errors are negligible, since only incoherent errors can be effectively amplified by these noise-scaling methods.

5.1.2 Overview of Probabilistic Error Cancellation

The main idea of PEC is to approximate a noiseless quantum circuit by averaging over distinct noisy circuits which consist of noisy, but implementable, quantum gates. The key assumption in PEC is having the full tomographic knowledge of these noisy gates. The first core step of PEC is to represent each noiseless gate, G_k, in U as a set of noisy but implementable gates $\{\tilde{G}_{k,h}\}_{h=1}^{\mathcal{H}}$. The total number of the noisy gates, $\mathcal{H}$, required to represent G_k at any time varies gate by gate and is dependent on k. The noisy

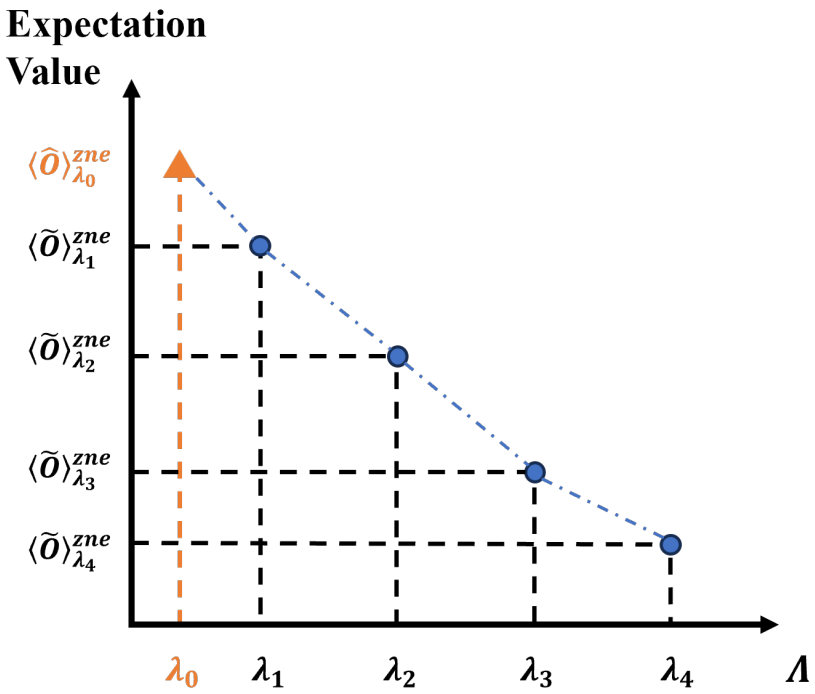

Figure 5.2: Noisy and zero-noise expectation values as a function of Λ obtained via ZNE.

representation of G_k is given by

$$G_k = \sum_{h=1}^{\mathcal{H}} \Gamma_{k,h} \tilde{G}_{k,h} = \Gamma_{k,1}\tilde{G}_{k,1} + \Gamma_{k,2}\tilde{G}_{k,2} + \cdots + \Gamma_{k,\mathcal{H}}\tilde{G}_{k,\mathcal{H}}, \tag{5.3}$$

where $\{\Gamma_{k,h}\}$ are real coefficients and may take negative values. Moreover, $\{\Gamma_{k,h}\}$ satisfy the trace-preserving condition, *i.e.*,

$$\sum_h \Gamma_{k,h} = 1 \quad \text{and} \quad \zeta_k = \sum_h |\Gamma_{k,h}| \geq 1, \tag{5.4}$$

implying that $\{\Gamma_{k,h}\}$ are normalized and form a quasiprobability distribution [28, 33] in terms of the index h. The constant ζ_k represents the one-norm of the quasiprobability distribution and quantifies its negativity, indicating the extent of its deviation from a true probability distribution [153].

The second core step of PEC is to estimate the noiseless expectation value, $\langle O \rangle$, by sampling from the noisy representations of the noiseless gates, as shown in Eq. (5.3), via

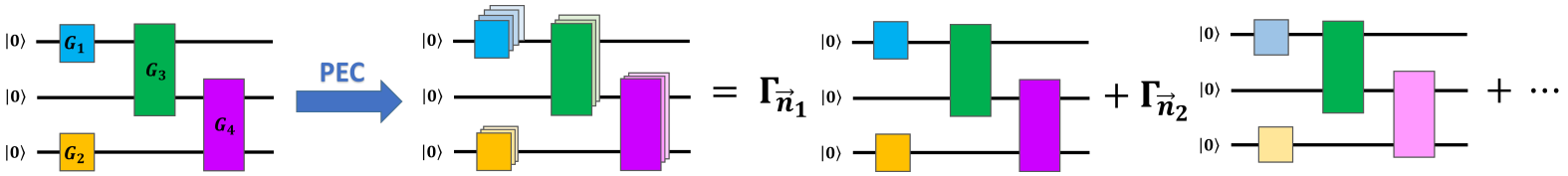

Figure 5.3: Noisy representation of the original (noiseless) quantum circuit, U, in PEC. Suppose that U includes four noiseless unitary gates, namely G_1, G_2, G_3, and G_4, and each unitary gate is represented by a group of implementable but noisy gates. Therefore, U can be represented by a linear combination of noisy quantum circuits with implementable gates only.

a Monte Carlo average [28]. Replacing each G_k in U with its noisy representation, $\langle O\rangle$ can be expressed as

$$\langle O\rangle = \mathrm{Tr}\left[U(\rho_0)O\right] = \sum_{\vec{n}} \Gamma_{\vec{n}} \langle \tilde{O}\rangle_{\vec{n}}^{pec}, \tag{5.5}$$

where ρ_0 is the initial state, $|0\rangle^{\otimes n'}$, of U and $\{\langle \tilde{O}\rangle_{\vec{n}}^{pec}\}$ are noisy expectation values. Note that $\{\Gamma_{\vec{n}}\}$ are real coefficients and also form a quasiprobability distribution with one-norm ζ, *i.e.*,

$$\sum_{\vec{n}} \Gamma_{\vec{n}} = 1 \quad \text{and} \quad \zeta = \sum_{\vec{n}} |\Gamma_{\vec{n}}| = \prod_{k=1}^{K} \zeta_k. \tag{5.6}$$

Note that, in specific, $\Gamma_{\vec{n}}$ and $\langle \tilde{O}\rangle_{\vec{n}}^{pec}$ can be expressed as

$$\Gamma_{\vec{n}} := \prod_{k=1}^{K} \Gamma_{k,h} \quad \text{and} \quad \langle \tilde{O}\rangle_{\vec{n}}^{pec} := \mathrm{Tr}\left[\tilde{U}_{\vec{n}}\left(\rho_0\right) O\right], \tag{5.7}$$

where $\tilde{U}_{\vec{n}}$ is defined as

$$\tilde{U}_{\vec{n}} := \prod_{k=1}^{K} \tilde{G}_{k,h}, \quad \text{such that} \tag{5.8}$$

$$U = \sum_{\vec{n}} \Gamma_{\vec{n}} \tilde{U}_{\vec{n}} = \Gamma_{\vec{n}_1} \tilde{U}_{\vec{n}_1} + \Gamma_{\vec{n}_2} \tilde{U}_{\vec{n}_2} + \cdots = \prod_{k=1}^{K} \left(\sum_{h=1}^{\mathcal{H}} \Gamma_{k,h} G_{k,h} \right). \tag{5.9}$$

The noisy representation of U, as shown in Eq. (5.9), is illustrated in Fig. 5.3. Note that $\{\tilde{U}_{\vec{n}}\}$ are regarded as ancillary circuits of PEC. Since these ancillary circuits only require implementable gates, all $\langle \tilde{O}\rangle_{\vec{n}}^{pec}$ can be obtained from the NISQ devices. In principle, with full tomographic knowledge of $\{\tilde{G}_{k,h}\}$ and a sufficiently large number of the ancillary circuits, an unbiased estimate of $\langle O\rangle$ can be obtained. However, the required number of executions of the ancillary circuits grows exponentially with the circuit depth in U, making PEC typically unfeasible [33]. To solve this problem, a Monte Carlo approximation is considered [28, 30, 153, 154].

To conduct the Monte Carlo approximation, the quasiprobability distribution in terms of $\Gamma_{k,h}$ should be converted to a positive probability distribution in the form of

$$p_k(h) = \frac{|\Gamma_{k,h}|}{\zeta_k}. \tag{5.10}$$

Therefore, the noisy representation of G_k can be rewritten as

$$G_k = \sum_{h=1}^{\mathcal{H}} \Gamma_{k,h} \tilde{G}_{k,h} = \sum_{h=1}^{\mathcal{H}} p_k(h) \zeta_k \mathrm{sgn}\left(\Gamma_{k,h}\right) \tilde{G}_{k,h}, \tag{5.11}$$

where $\mathrm{sgn}\left(\cdot\right)$ represents the sign function. Then, a noisy but implementable gate is sampled from $\{\tilde{G}_{k,h}\}$ at random over the probability distribution, $p_k(h)$, where the sampled gate is denoted as $\tilde{G}_{k,\hat{h}}$. With sufficient samples, an estimation of G_k can be represented as

$$\hat{G}_k = \left\{ \zeta_k \mathrm{sgn}\left(\Gamma_{k,\hat{h}}\right) \tilde{G}_{k,\hat{h}} \right\}_{\mathrm{avg}}, \tag{5.12}$$

where $\{\cdot\}_{\mathrm{avg}}$ represents the sampling average. After sampling each G_k in U, an unbiased estimate of U can be expressed as

$$\hat{U} = \hat{G}_K \cdots \hat{G}_k \cdots \hat{G}_2 \hat{G}_1 = \zeta \mathrm{sgn}\left(\Gamma_{\vec{n}}\right) \tilde{U}_{\vec{n}}, \tag{5.13}$$

where $\mathrm{sgn}\left(\Gamma_{\vec{n}}\right) = \prod_{k=1}^{K} \mathrm{sgn}\left(\Gamma_{k,\hat{h}}\right)$ and $\tilde{U}_{\vec{n}} = \prod_{k=1}^{K} \tilde{G}_{k,\hat{h}}$, such that $U = \{\hat{U}\}_{\mathrm{avg}}$. Note that $\tilde{U}_{\vec{n}}$ is the sampled noisy circuit (the ancillary circuit of PEC) and ζ is a constant, as shown in Eq. (5.6). Consequently, an estimation of $\langle O \rangle$ is given by

$$\langle \hat{O} \rangle^{pec} = \left\{ \mathrm{Tr}\left[\hat{U}(\rho_0) O \right] \right\}_{avg} = \left\{ \zeta \mathrm{sgn}\left(\Gamma_{\vec{n}}\right) \langle \tilde{O} \rangle_{\vec{n}}^{pec} \right\}_{avg}, \tag{5.14}$$

where $\langle \tilde{O} \rangle_{\vec{n}}^{pec} = \mathrm{Tr}\left[\tilde{U}_{\vec{n}}(\rho_0) O \right]$.

Using the Monte Carlo approximation, a finite number of samples is required regardless of the circuit depth of U. To ensure the precision of the estimation of $\langle O \rangle$, the required number of samples scales as

$$\text{the required number of samples} \propto \frac{\zeta^2}{\delta^2}, \tag{5.15}$$

where δ represents the absolute error between $\langle \hat{O} \rangle^{pec}$ and $\langle O \rangle$. It can be observed that the required number of samples increases with ζ, which grows exponentially with the number of gates in U, indicating that PEC is more practical for quantum circuits with medium or small depth [33].

5.2 Experiments

We now apply the mitigation methods to quantum routing realized on *ibmq_jakarta*, the 7-qubit superconducting quantum device. We use the quantum routing protocol introduced in Subsection 3.1.1 as the application to benchmark the performance of the mitigation methods. The quantum circuit used to realize the routing application is the router circuit shown in Fig. 4.2. However, since except for the fidelity, F, we also use the probability, P, as our performance metric, QST applied to the three qubits is replaced by three Z-basis measurements when the evaluated performance metric is P. The two quantum error mitigation methods, ZNE and PEC, mainly focus on quantum gate errors, decoherence errors, and cross-talk errors - they cannot mitigate measurement errors. Therefore, the MEM method (see Subsection 2.3.2.1) is still considered in our experiments to eliminate measurement errors. Henceforth by the term "unmitigated" we will mean without any ZNE or PEC included in the results - MEM is by default included in *all* results we show here. The term "error mitigation" will henceforth refer only to ZNE and/or PEC.

5.2.1 Experimental Setup

To investigate the experimental performance of the quantum routing protocol with quantum error mitigation, we utilize an open-source package named Mitiq [155] to implement ZNE and PEC. Although Qiskit recently released built-in functions for employing quantum error mitigation methods (twirled readout error extinction, ZNE, and PEC) [156], one cannot implement these methods step by step and obtain detailed data. Another reason why we choose Mitiq instead of Qiskit's built-in functions is that we can concatenate multiple mitigation methods through Mitiq. For implementing ZNE, we set the noise scale factor $\{\lambda_j\}_{j=1}^{J=7} = \{1, 3, 5, 7, 9, 11, 13\}$, and we choose local folding at random to scale the noise. Seven noise-scaled circuits are generated based on the seven values of λ_j, and each noise-scaled circuit is executed $C_{tot} = 100,000$ times (this number of exe-

cutions applied to all experiments in this chapter). We choose polynomial extrapolation with order 2 to obtain the zero-noise expectation value, $\langle \hat{O} \rangle_{\lambda_0}^{zne}$.

In principle, we need to acquire full tomographic knowledge of the quantum gates in the transpiled circuit to implement PEC. However, to simplify our experiments, we make two assumptions: (i) We assume we can neglect single-qubit gate errors and only focus on two-qubit gate errors since the two-qubit gate error rates are an order of magnitude higher. (ii) We assume that the two-qubit gates are followed by a global depolarizing noise. The transpiled circuit only has one type of two-qubit gate, the CX gate. Based on assumption (ii), we have

$$\tilde{G}_{noisy}^{\mathrm{C}X} = \mathcal{D} \circ \mathcal{P} \circ G_{ideal}^{\mathrm{C}X}, \tag{5.16}$$

where $\tilde{G}_{noisy}^{\mathrm{C}X}$ is the implementable CX gate that we assumed, $G_{ideal}^{\mathrm{C}X}$ is the noiseless CX gate, and $\mathcal{P} \in \{I, X, Y, Z\}^{\otimes 2}$ is a Pauli trace-preserving completely positive map. Note that

$$\mathcal{D}(\rho_{in}) = (1 - \epsilon)\rho_{in} + I\epsilon/4, \tag{5.17}$$

represents the 2-qubit depolarizing channel [28], where ρ_{in} stands for the input state of this channel and in this chapter, ϵ is the noise level of the CX gate. For each CX gate in the transpiled circuit, we acquire the associated CX gate error ϵ, which varies over time, from the calibration data reported in [66]. Based on Eqs. (5.16) and (5.17), and with known ϵ, $G_{ideal}^{\mathrm{C}X}$ can be represented by a group of noisy gates in the form of Eq. (5.3). Then, using noisy representation of the noiseless CX gate, we conduct a Monte Carlo sampling process via Mitiq with 20 samples (20 ancillary circuits are generated for PEC). From the many executions, the measurement results of the ancillary circuits are collected to estimate $\langle O \rangle$.

To concatenate ZNE and PEC, we first fold gates (from the left) of the transpiled circuit with $\{\lambda_j\}_{j=1}^{J=5} = \{1, 3, 5, 7, 9\}$, generating five noise-scaled circuits. We then apply PEC to each noise-scaled circuit with 20 samples, which means that we represent each CX gate in the noise-scaled circuits by its noisy representation that we derived before.

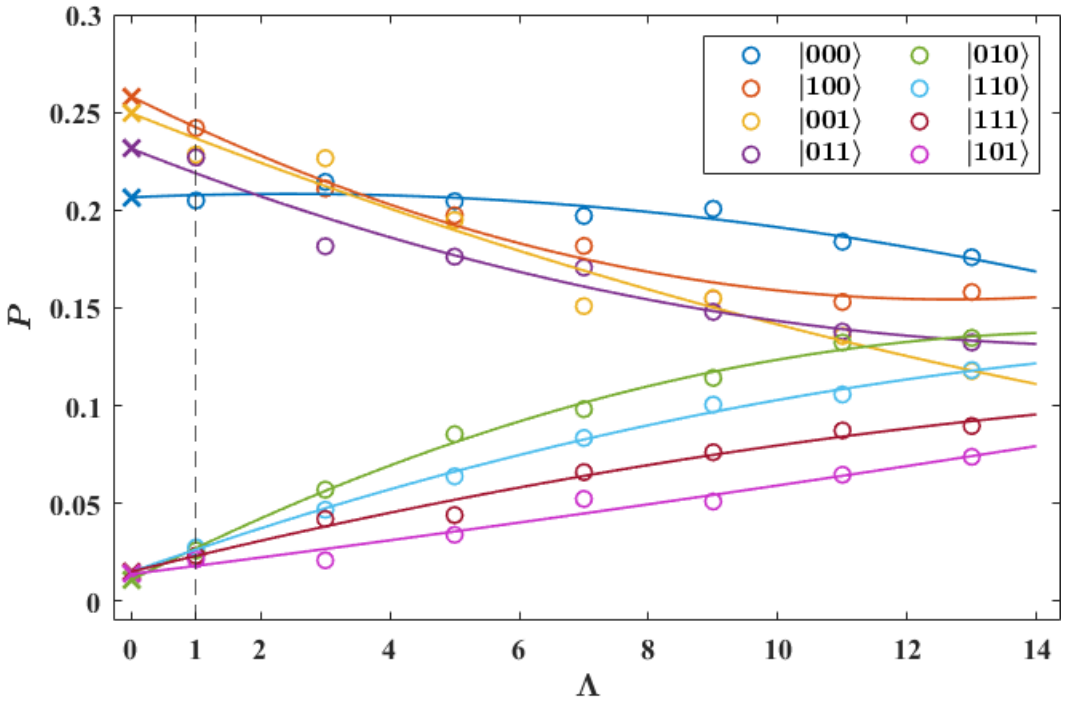

Figure 5.4: P as a function of Λ using ZNE. The circles represent P obtained from the quantum device, and the circles plotted on the vertical dashed lines indicate the unmitigated results of P. The solid lines are polynomial fitted curves with order 2, and the cross markers stand for the corresponding mitigated results of P.

From the many executions, the error-mitigated data of the noise-scaled circuits are collected, the data will be utilized for extrapolating to the zero-noise expectation value, again by polynomial extrapolation with order 2.

5.2.2 Experimental Results

Instead of using the expectation values, we utilize probability P as one of our performance metrics. In this quantum routing experiment, P is the probability of measuring ρ to be in one of the eight eigenstates, which are $\{|000\rangle, |001\rangle, \cdots, |111\rangle\}$) with the measurement operator $O = Z^{\otimes 3}$. The values of P as a function of λ using ZNE are demonstrated in Fig. 5.4. In the noiseless situation, the probability of observing one of

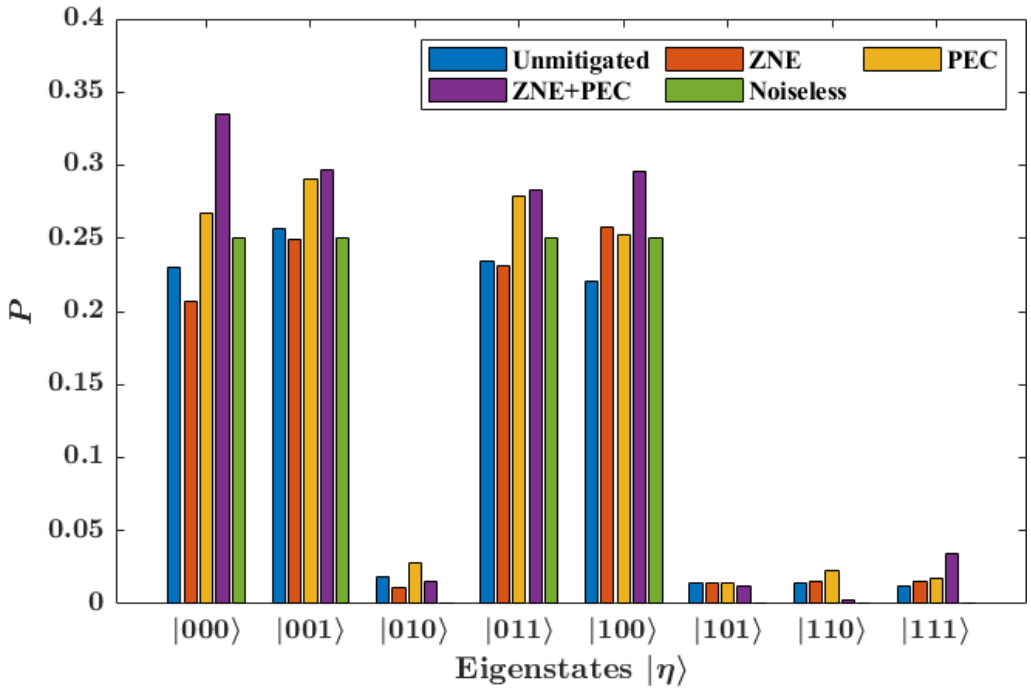

Figure 5.5: Results using ZNE or/and PEC obtained from the quantum device. The green bars are noiseless results plotted for reference, and the missing green bars indicate that the noiseless results should be 0.

the $|000\rangle$, $|001\rangle$, $|011\rangle$, and $|100\rangle$ states is 0.25, and the probability of observing one of the remaining states is 0. We see that the noise grows with increasing Λ, and the extrapolated results are closer to (or even the same as) the noiseless results, indicating that ZNE is an effective method to mitigate quantum errors. The unmitigated and mitigated P using different error mitigation methods are demonstrated in Fig. 5.5. One can observe that P are closer to the noiseless results after introducing an error mitigation method. However, some over-correction can be noticed, especially when the concatenation of ZNE and PEC is applied.

Beyond P, we choose the fidelity, F, between ρ' and ρ as our main performance metric, as shown in Eq. (3.10). Recall that $\rho' = |\Phi\rangle_f\langle\Phi|$ is the theoretical density matrix of the quantum router's output, and ρ is the corresponding experimental density matrix. Since ρ is a 3-qubit density matrix reconstructed by QST (see Subsection 2.1.3), there

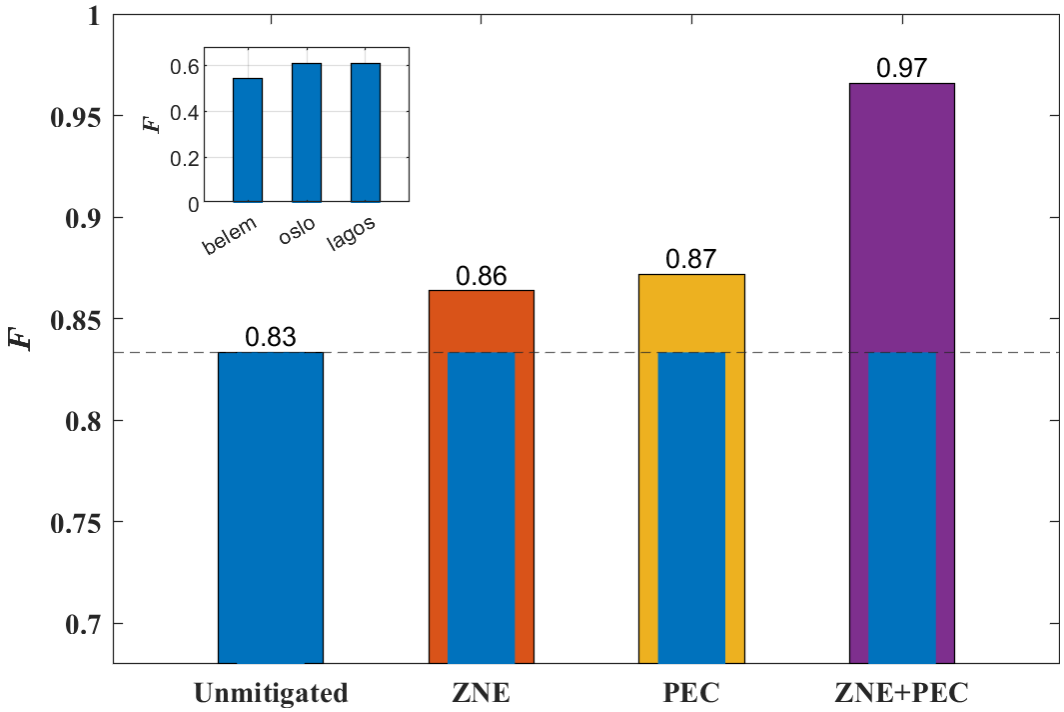

Figure 5.6: F of the quantum router with and without quantum error mitigation methods. The dashed horizontal line indicates the fidelity with MEM only. The inset figure indicates the unmitigated result of the quantum routing protocol conducted on other quantum devices, namely *ibmq_belem*, *ibm_oslo*, and *ibm_lagos*. One can observe that these machines obtained lower values of F compared to the one of *ibmq_jakarta*, such that we take the unmitigated value $F = 0.83$ as the baseline for comparing the mitigated results.

are $3^3 = 27$ copies of the transpiled circuits (the router circuit after the transpilation process), each with distinct measurement operators. We apply ZNE or/and PEC to each transpiled circuit for error mitigation.

The values of F determined with different error mitigation methods are plotted in the main part of Fig. 5.6. Note that although F is state-dependent, we have tested other signal states and observed similar experimental outcomes. For comparison, in the inset of Fig. 5.6, we also demonstrate the unmitigated F values determined from other IBM's quantum devices, namely, *ibmq_belem*, *ibm_oslo*, and *ibm_lagos*. These inset values show that the machine we use here, *ibm_jakarta*, offers the optimal performance in terms of

unmitigated results and therefore forms the optimal starting point to apply mitigation methods to. Reverting back to the main part of the figure, we can see the fidelity results for singular use of ZNE and PEC are similar, showing a minor improvement in F compared to the unmitigated result obtained from *ibm_jakarta*. However, interestingly the concatenation method demonstrates $F \approx 1$, representing an almost-perfect performance. We should note this improvement does come at a cost - the concatenation method has a higher resource requirement and demands a longer execution time compared to the singular use of ZNE or PEC. Typically, for a transpiled circuit, ZNE and PEC require 210 and 74 seconds for execution, respectively, while the concatenation method requires 1116 seconds. ZNE cannot amplify coherent errors via folding gates, *i.e.*, only incoherent errors can be scaled and mitigated. PEC mitigates the CX gate errors (regardless of whether coherent or incoherent errors), which compensates for the drawback of ZNE. *The almost-unity fidelity outcome of Fig. 5.6 represents the main result of this work.*

5.2.3 Quantum Random Access Memory with Error Mitigation

It is perhaps useful to close this work with a short discussion on QRAM, another application that uses quantum-routing-like functionality. We still use the bucket-brigade style QRAM circuit shown in Fig. 4.4(b) to conduct our experiment. However, in this chapter, we define that $|D_0\rangle$ is a random qubit storing quantum information and $|D_1\rangle = |1\rangle$ stores classical information, where $|D_0\rangle$ and $|D_1\rangle$ are data stored at the two memory cells. We again utilize F' as our performance metric (see Eq. (4.6)), where F' is the fidelity between the theoretical density matrix of $|\Psi\rangle_f$ (the output of the QRAM) and the experimental density of $|\Psi\rangle_f$ reconstructed by applying QST on the first (count from the top) and the last qubits of the QRAM circuit illustrated in Fig. 4.4(b). However, from our QRAM experiments we find the maximum increase in fidelity due to error mitigation is only 4% (maximum fidelity found being 0.76). This phenomenon is caused by the complexity of the transpiled circuits, relative to the transpiled quantum routing

application discussed earlier. In particular, one can observe that the QRAM circuit includes two controlled-swap gates (see Fig. 4.4(b)), while the quantum routing circuit requires one such gate. The increase in the number of controlled-swap gates leads to a longer time and a higher complexity for the execution of QRAM. The longer execution time amplifies the decoherence errors, and the increase of the number of gates in the execution accumulates the gate errors. Future work for implementing QRAM on the NISQ devices should focus on the improvement of the quantum error mitigation methods designed for complicated quantum circuits.

5.3 Summary

In this work, we experimentally tested the performance of two quantum error mitigation methods, ZNE and PEC, implemented in the context of a quantum routing protocol. We found concatenating ZNE and PEC impressively increased the entanglement fidelity of the quantum router to effectively unity. Although quantum error mitigation methods require additional executions of ancillary quantum circuits, our results show the critical role such methods can have for applications run on current NISQ devices. More specifically, our results provide an overview of what can be anticipated for an error-mitigated quantum router in practice - illustrating that full-blown quantum error correction processes need not be implemented on current devices for this important quantum application.

Chapter 6

Error-Mitigated Multi-Layer Quantum Routing

In Chapter 5, we have explored the performance of the quantum router, which has only one layer, with quantum error mitigation on current superconducting devices. Although the concatenation of ZNE and PEC has shown success in the quantum routing application, it is evident that, in applications with greater circuit depth, the performance of quantum error mitigation is limited and may, in some cases, be worse than unmitigated circuits [33, 35, 42, 157, 158]. Therefore, room for new mitigation techniques, tailored to specific applications, exists. In this chapter, we propose a new quantum error mitigation method, named eCDR, that builds a conceptual bridge between the ZNE and CDR - exploiting the characteristics of both methods best suited to the application at hand. The application we focus on to design and test our new mitigation method is multi-layer quantum routers (in which each router output path is input into another router). We shall see our new method, eCDR, goes beyond a simple concatenation of different existing methods. The main contributions of this Chapter can be summarized as follows.

(i) We propose a new quantum error mitigation method, namely eCDR, and bench-

mark this method using a practical quantum application: multi-layer quantum routers.

(ii) We experimentally implement multi-layer quantum routers on a NISQ device and benchmark their performance with and without ZNE, CDR, or eCDR methods.

6.1 Quantum Routers with State Tomography

6.1.1 Multi-layer Quantum Routers

The simplest structure of the quantum router consists of the signal qubit, $|\phi\rangle_s$, the control qubit, $|\phi\rangle_c$, and the ancillary qubit $|\phi\rangle_n = |0\rangle_n$. The output of the quantum router, $|\Phi\rangle_f$, is an entanglement of these three qubits, as explained in Subsection 3.1.1. We denote the quantum router with two output paths as the 1-layer quantum router. To increase the number of output paths, we concatenate quantum routers as depicted in Fig. 6.1. The output paths of the first-layer (second-layer) quantum router serve as the input paths for the quantum routers in the second (third) layer. The 2-layer quantum router consists of three 1-layer quantum routers, resulting in four output paths, and the 3-layer quantum router consists of seven 1-layer quantum routers, resulting in eight output paths. For clarification, we denote the first output path of the 1-layer quantum router as path 1-1, and the remaining output paths following a similar notation.

The 1-layer quantum router circuit is also demonstrated in Fig. 6.1. In this router circuit, the signal qubit is prepared in a random quantum state using the purple single-qubit gate. In our experiments, this purple gate transforms the signal qubit to a quantum state with the parameters $\alpha_s = 0.5 + 0.13i$ and $\beta_s = -0.82 - 0.22i$. The control qubit is converted to a superposition with $\alpha_c = \beta_c = 1/\sqrt{2}$ using the Hadamard gate. The controlled-swap gate, the 3-qubit gate in orange, realizes the quantum routing process. The 2-layer router circuit is similar to the 1-layer router circuit but with 3 control qubits, 4 path qubits (1 signal qubit and 3 ancillary qubits), and 3 controlled-swap gates, as

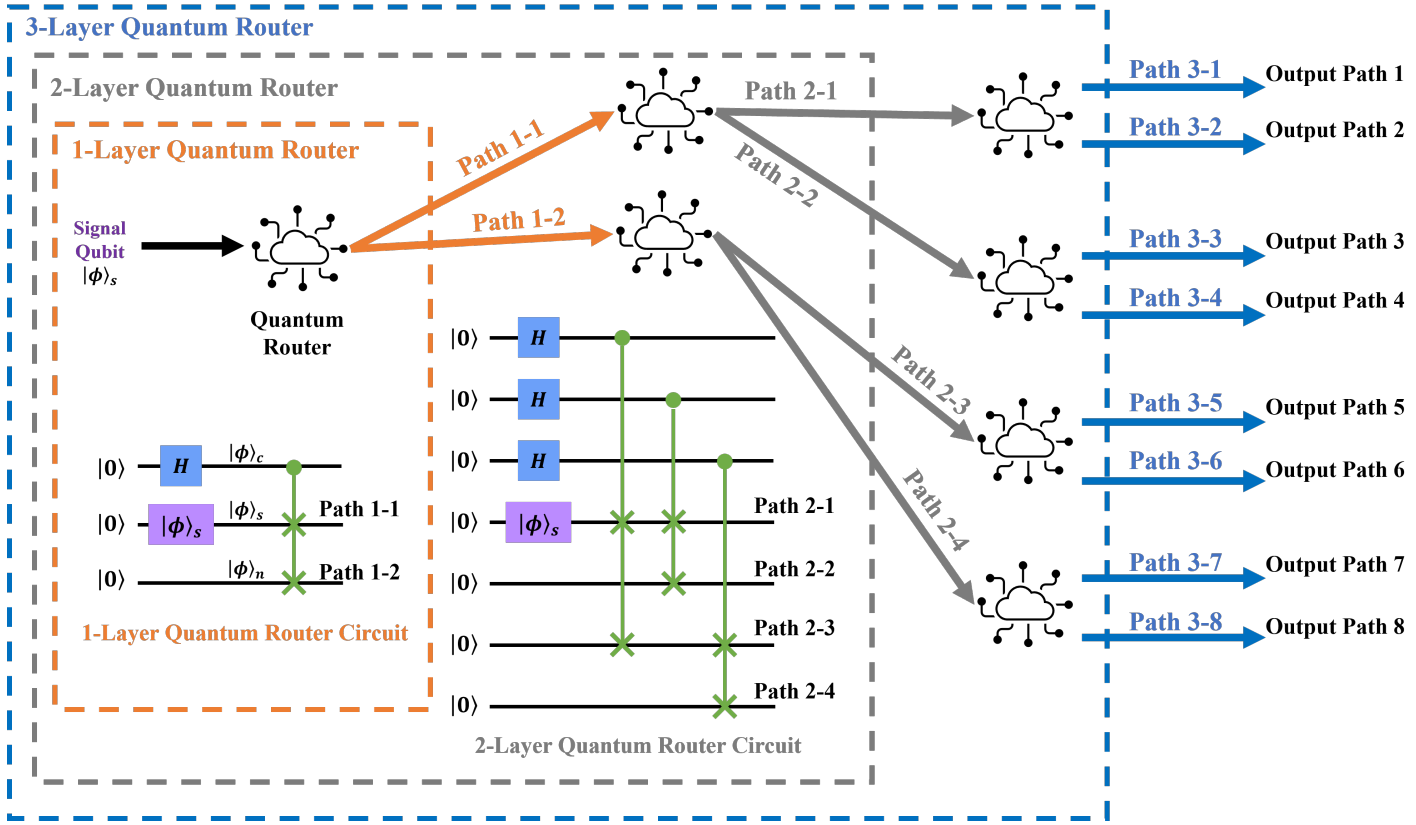

Figure 6.1: Schematic of multi-layer quantum routers with 1 and 2-layer quantum router circuit. In the circuits, all qubits are initialized in the $|0\rangle$ state. The single-qubit gate in blue represents the Hadamard gate, while the one in purple prepares the signal qubit by transforming $|0\rangle$ into $|\phi\rangle_s$. The 3-qubit gate is a controlled-swap gate that swaps the states of the qubits marked with cross symbols when the qubit marked with a solid circle is in the $|1\rangle$ state and leaves them unchanged when it is in the $|0\rangle$ state.

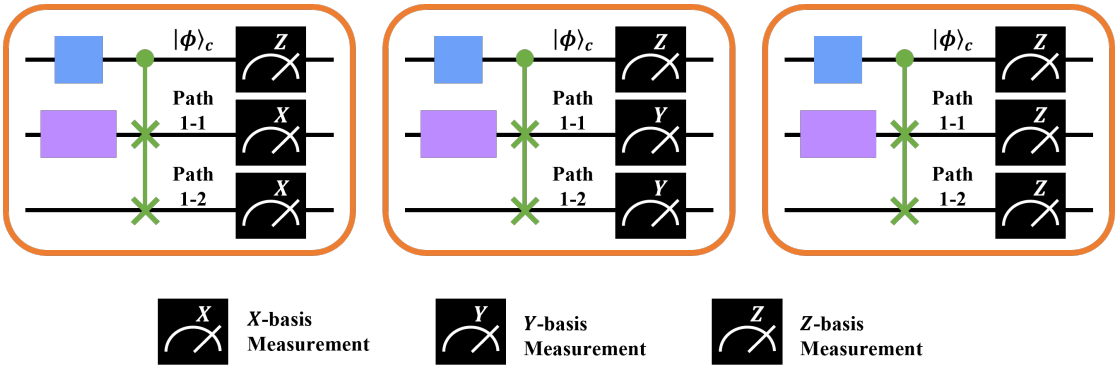

Figure 6.2: Tomography circuits utilized to reconstruct the quantum state of the signal qubit in the 1-layer quantum router.

demonstrated in Fig.6.1. Similarly, the 3-layer router circuit has 7 control qubits, 8 path qubits (1 signal qubit and 7 ancillary qubits), and 7 controlled-swap gates.

6.1.2 Multi-layer Quantum Routers with State Tomography

We choose the state fidelity, F_s, between ϱ' and ϱ as our performance metric, as shown in Eq. (4.5). Recall that $\varrho' = |\phi\rangle_s\langle\phi|$ and ϱ is the reconstructed quantum state of the signal qubit at the output of the quantum router. In other words, ϱ represents the noisy experimental density matrix of the signal qubit and is reconstructed via QST, while ϱ' is the noiseless density matrix used for comparison.

Since the signal information can be found in multiple output paths after the quantum routing process, we apply the Z-basis measurements to the control qubits, whose measurement result indicates the location of the signal qubit. We also apply the three basis measurements to each path qubit and post-select only the measurement results of the path qubit that contains the signal information to reconstruct ϱ. For the 1-layer quantum router, there are a total of three tomography circuits, as demonstrated in Fig. 6.2, which correspond to the 1-layer router circuit with three different measurement operators: $O = Z \otimes Z \otimes Z$, $Z \otimes X \otimes X$, and $Z \otimes Y \otimes Y$. Since the quantum device only supports the Z-basis measurements, we perform the X-basis measurements by adding a

Hadamard gate before the Z-basis measurement and achieve the Y-basis measurements by sequentially adding an $S^\dagger$ gate (which induces a $-\pi/2$ phase) and a Hadamard gate before the Z-basis measurement.

6.2 Quantum Error Mitigation

6.2.1 Overview of Clifford Data Regression (CDR)

The main idea of CDR involves constructing near-Clifford circuits, denoted as $\{V_m\}_{m=1}^{M}$, that can be efficiently computed by classical simulators. Note that these near-Clifford circuits are close to U, the original circuit of interest, and evaluated both on a noiseless simulator and the quantum device. The measurement results of $\{V_m\}$ obtained from the simulator are considered noiseless results, while those from the quantum device are considered noisy results. Using these noiseless and noisy results, the noiseless and noisy expectation values of O after executing the near-Clifford circuits are calculated, and a linear regression model is constructed in the form of

$$\langle \hat{O} \rangle^{cdr} = a\langle \tilde{O} \rangle + b, \tag{6.1}$$

where $\langle \hat{O} \rangle^{cdr}$ represents the CDR error-mitigated expectation value and $\langle \tilde{O} \rangle$ represents the experimental expectation value of O after executing U. Note that a and b are real parameters determined by

$$(a, b) = \arg\min_{(a,b)} \sum_{m=1}^{M} \left[\langle O \rangle_m^{cdr} - \left(a\langle \tilde{O} \rangle_m^{cdr} + b \right) \right]^2, \tag{6.2}$$

where $\left\{ \langle O \rangle_m^{cdr} \right\}$ and $\left\{ \langle \tilde{O} \rangle_m^{cdr} \right\}$ represent the noiseless and noisy expectation values of O after executing the near-Clifford circuits, respectively. The linear regression model can also be constructed directly from the experimental results of the near-Clifford circuits and then applied to the experimental results of U. Note that CDR can, in principle, perfectly mitigate the noise of a global depolarizing channel [34].

The specific working principle of ZNE is provided in Subsection 5.1.1. The concatenation of ZNE and CDR denoted as "ZNE+CDR" and "CDR+ZNE," can be considered for potentially better results. The ZNE+CDR method first generates a group of noise-scaled circuits and then utilizes CDR to mitigate the experimental results of each noise-scaled circuit. These mitigated results are then utilized to extrapolate the zero-noise result. The drawback of ZNE+CDR is that mitigating the experimental results of the noise-scaled circuits makes it challenging to redefine the relationship between these results and the noise scale factors of the noise-scaled circuits. The main idea of CDR+ZNE is similar but in the opposite order: first, near-Clifford circuits close to U are generated, and the experimental results of each near-Clifford circuit are error-mitigated by ZNE. Afterward, this ZNE error-mitigated data is utilized to conduct the remaining steps of CDR: constructing a linear regression model and using this model for error mitigation. The disadvantage of CDR+ZNE is that since this method finally relies on the relationship between noisy and noiseless results to mitigate errors, applying any error mitigation to the near-Clifford data disrupts this relationship.

6.2.2 The Extrapolated CDR Method

The key idea of eCDR is that it establishes several groups of near-Clifford circuits. Each group is evaluated at different noise levels, and their experimental results are used to construct linear regression models. The real parameters in these models are then extrapolated to derive a new linear regression model, which is then applied to the experimental results of the original quantum circuit. Note that eCDR can be used to derive error-mitigated expectation values, however, here we use the experimental results to provide an example of the eCDR method. The schematic of eCDR is illustrated in Fig. 6.3, and its main steps are as follows.

(i) *Generation of noise-scaled circuits.* Firstly, we generate J noise-scaled circuits, denoted as $\{N_{\lambda_j}\}_{j=1}^{J}$, in the same manner as the initial step of ZNE.

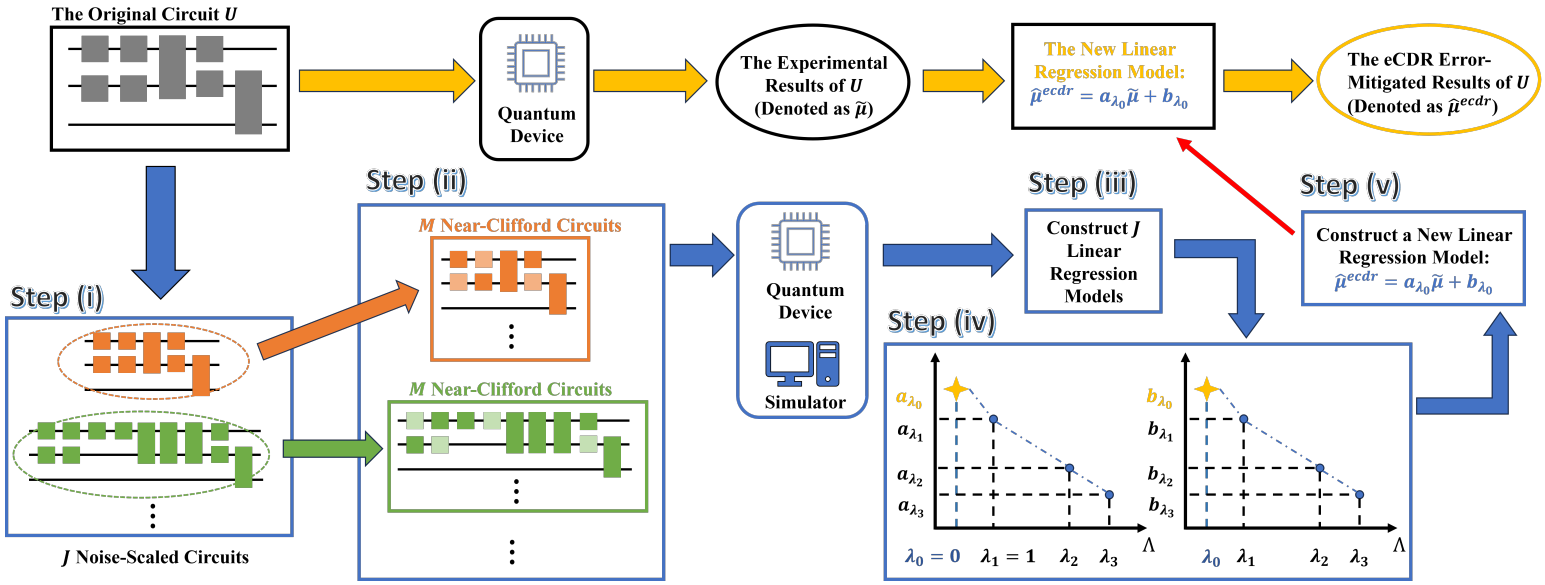

Figure 6.3: Schematic of the eCDR method. Based on U, J noise-scaled circuits are generated, and M near-Clifford circuits are constructed for each noise-scaled circuit. All near-Clifford circuits are executed on a simulator and a quantum device to construct a total of J linear regression models. Then, the real parameters in these models are extrapolated to build a new linear regression model for mitigating the experimental results of U.

(ii) *Generation of near-Clifford circuits.* Then, for each noise-scaled circuit, N_{λ_j}, we generate M near-Clifford circuits, denoted as $\{T_{\lambda_j,m}\}_{m=1}^{M}$. Note that the M circuits in $\{T_{\lambda_j,m}\}$ are all close to N_{λ_j} but slightly different from each other, as they are generated by randomly converting a portion of non-Clifford gates in N_{λ_j} to Clifford gates. There are a total of J sets of $\{T_{\lambda_j,m}\}$ and a total of $\mathbb{D} = JM$ near-Clifford circuits.

(iii) *Construction of linear regression models.* We execute $\mathbb{D}$ near-Clifford circuits on both the simulator and the quantum device. We denote the measurement results of $\{T_{\lambda_j,m}\}$ from the simulator and the quantum device as $\{\mu^{ecdr}_{\lambda_j,m}\}$ and $\{\tilde{\mu}^{ecdr}_{\lambda_j,m}\}$, respectively. Note that $\{\mu^{ecdr}_{\lambda_j,m}\}$ and $\{\tilde{\mu}^{ecdr}_{\lambda_j,m}\}$ are regarded as noiseless and noisy measurement results, respectively. We then construct a linear regression model in the form of

$$\hat{\mu}^{ecdr}_{\lambda_j,m} = a_{\lambda_j}\tilde{\mu}^{ecdr}_{\lambda_j,m} + b_{\lambda_j}, \tag{6.3}$$

where $\hat{\mu}^{ecdr}_{\lambda_j,m}$ is an estimated measurement result of $T_{\lambda_j,m}$. Note that a_{λ_j} and b_{λ_j} are real parameters determined by the least-squares method given by

$$(a_{\lambda_j}, b_{\lambda_j}) = \underset{(a_{\lambda_j}, b_{\lambda_j})}{\arg\min} \sum_{m=1}^{M} \left[\mu^{ecdr}_{\lambda_j,m} - (a_{\lambda_j}\tilde{\mu}^{ecdr}_{\lambda_j,m} + b_{\lambda_j})\right]^2. \tag{6.4}$$

There are a total of J linear regression models corresponding to J noise-scaled circuits. This step is proposed based on CDR, which utilizes a linear regression model to describe the relationship between noiseless and noisy measurement results.

(iv) *Extrapolations.* We then collect all of the real parameters in these J linear regression models, specifically $\{a_{\lambda_j}\}$ and $\{b_{\lambda_j}\}$. We then employ curve fitting to these parameters to extrapolate two new parameters, denoted as a_{λ_0} and b_{λ_0}. Similar to ZNE, alternative extrapolation methods can be considered, we choose to use quadratic polynomial extrapolation model in our experiments. Using $\{a_{\lambda_j}\}$ as an example, the quadratic polynomial extrapolation is in the form of

$$f(\Lambda) = c_0 + c_1\Lambda + c_2\Lambda^2, \tag{6.5}$$

where c_0, c_1, and c_2 are real parameters selected by

$$(c_0, c_1, c_2) = \underset{(c_0,c_1,c_2)}{\arg\min} \sum_{j=1}^{J} \left[a_{\lambda_j} - \left(c_0 + c_1\lambda_j + c_2\lambda_j^2\right)\right]^2. \tag{6.6}$$

This curve fitting process for $\{b_{\lambda_j}\}$ is the same but the selected parameters, c_0, c_1, and c_2, are different. By setting $\Lambda = \lambda_0$ in Eq. (6.5), we determine a_{λ_0} and b_{λ_0}, which can also be expressed as

$$a_{\lambda_0} = \sum_{j=1}^{J} \gamma_j a_{\lambda_j} \quad \text{and} \quad b_{\lambda_0} = \sum_{j=1}^{J} \gamma_j b_{\lambda_j}, \tag{6.7}$$

where $\{\gamma_j\}$ are real parameters determined by the values of $\{\lambda_j\}$ and the selected extrapolation model.

(v) *Construction of a new linear regression model for mitigation.* With a_{λ_0} and b_{λ_0}, we construct a new linear regression model given by

$$\hat{\mu}^{ecdr} = a_{\lambda_0}\tilde{\mu} + b_{\lambda_0}, \tag{6.8}$$

where $\tilde{\mu}$ is the experimental results of U and $\hat{\mu}^{ecdr}$ is the corresponding eCDR error-mitigated results. Similar to CDR, the selection of this linear regression model in eCDR is motivated by considering the effect of the global depolarizing channel (see Appendix B.1). It can be observed that if CDR were capable of perfectly correcting errors, the additional noise scaling in eCDR would introduce further errors. However, in practice, CDR cannot fully correct errors on current quantum devices, a limitation that motivates the design of eCDR.

It is worth mentioning that the eCDR method should not be confused with variable-noise CDR (vnCDR) [35, 157]. Although both vnCDR and eCDR use noise-scaled near-Clifford data for error mitigation, the approaches to utilizing this data differ. In vnCDR, a set of near-Clifford circuits, denoted as $\{\mathcal{T}_m\}_{m=1}^{M}$, are first generated, and then, for each $\mathcal{T}_m$, a set of noise-scaled near-Clifford circuits, denoted as $\{\mathcal{T}_{m,\lambda_j}\}_{j=1}^{J}$, are generated. After the execution of $\mathbb{D}$ noise-scaled near-Clifford circuits, vnCDR constructs an

extrapolation model for mitigation given by

$$\hat{\mu}^{vncdr} = \sum_{j=1}^{J} A_j \cdot \tilde{\mu}_{\lambda_j}, \tag{6.9}$$

where $\hat{\mu}^{vncdr}$ stands for the vnCDR error-mitigated result of U and $\tilde{\mu}_{\lambda_j}$ represents the experimental result of U_{λ_j}. Note that $\tilde{\mu}_{\lambda_1} = \tilde{\mu}$ with $\lambda_1 = 1$ and A_j are parameters selected by the least-squares method following

$$A_j = \arg\min_{A_j} \sum_{m=1}^{M} \left[\mu_m^{vncdr} - \sum_{j=1}^{J} A_j \cdot \tilde{\mu}_{m,\lambda_j}^{vncdr} \right]^2, \tag{6.10}$$

where μ_m^{vncdr} represents the measurement results of $\mathcal{T}_m$ collected from the simulator and $\tilde{\mu}_{m,\lambda_j}^{vncdr}$ represents the measurement results of $\mathcal{T}_{m,\lambda_j}$ collected from the quantum device. The vnCDR and eCDR methods utilize the noise-scaled near-Clifford data to construct the extrapolation model and the new linear regression model for mitigation, respectively. By comparing Eqs. (6.8) and (6.9), it can be observed that eCDR requires fewer resources compared to vnCDR: eCDR only requires the execution of U, while vnCDR requires the execution of $\{U_{\lambda_j}\}$, which includes J circuits.

For multi-layer quantum routers, the complexity of their circuits increases with the number of layers (see details in the next Section). Specifically, the number of qubits and circuit depth of a router circuit grow with the number of layers of the quantum router, with more qubits becoming entangled in higher-layer quantum routers. To mitigate errors in the router circuit with increased complexity, we designed eCDR, which combines the advantages of ZNE and CDR. ZNE is mainly effective for incoherent errors, while CDR is primarily effective for coherent errors and measurement errors. By extrapolating the parameters within the linear regression model, eCDR demonstrates the potential to effectively mitigate errors in the router circuits with increased complexity.

6.3 Experiments of Extrapolated CDR

6.3.1 Experimental Setup of Extrapolated CDR

In this work, we utilize a 127-qubit quantum device named *ibm_sherbrooke* [66] and a simulator to conduct our experiments. The quantum device, *ibm_sherbrooke*, is currently one of the smallest quantum devices provided by IBM, and the simulator is realized through Qiskit [67]. Our experiments utilize 3, 7, and 15 qubits to implement 1, 2, and 3-layer quantum routers, respectively. The tomography circuits must undergo transpilation (see Subsection 2.2.2.2), the process that converts them into transpiled circuits, prior to their execution on the quantum device. In transpilation, the control and path qubits are mapped to specific physical qubits of the quantum device, and each quantum gate in the tomography circuits is decomposed into basis gates, which can be directly implemented on the quantum devices. After the transpilation, the circuit depths of the 1, 2, and 3-layer transpiled router circuits are 54, 102, and 205, respectively. In addition, Mitiq software package [155] is partially utilized for the implementation of ZNE and CDR.

In our experiments, U corresponds to the unitary parts of the transpiled circuit, *i.e.*, the transpiled circuit excluding measurements. Any quantum circuit that requires execution on the quantum device or the simulator is executed $C_{tot} = 20,000$ times. The ZNE, CDR, and vnCDR methods were originally proposed to be utilized for expectation values, while in our experiments, we implement modified versions of them for calculating the state fidelity. Specifically, we apply these three methods to the measurement results instead of the expectation values of O (henceforth, the terms ZNE, CDR, and vnCDR in this chapter will refer only measurement result usage). We now discuss the experimental setups of the six mitigation methods we investigate.

(i) For ZNE, we generate three noise-scaled circuits (with measurements reintroduced) with λ_j values of approximately 1, 3, and 5, respectively. We choose the quadratic polynomial extrapolation model (as shown in Eq. (6.5)) to extrapolate error-mitigated

values. Note that our experiments can also be regarded as using Richardson extrapolation, as $J = 3$ and Richardson extrapolation is a special case of polynomial extrapolation of order $J - 1$.

(ii) For CDR, we generate 50 near-Clifford circuits that approximate the transpiled circuit to obtain adequately near-Clifford data for error mitigation. The transpiled circuit only contains the basis gates and measurement operations, and among all of the basis gates (see Tab. 3.1), only the $\mathrm{R}Z(\varphi)$ gate could potentially be a non-Clifford gate, depending on the value of φ. Note that the $\mathrm{R}Z(\varphi)$ gate rotates a single-qubit along the z-axis, where φ is a phase factor. We randomly select non-Clifford gates in the transpiled circuit with a probability of 90% to ensure that the near-Clifford circuits can be executed efficiently on the simulator, even for more complex transpiled circuits. The selected non-Clifford gates are converted to the nearest Clifford gates by adjusting the value of φ.

(iii) For eCDR, we generate the same noise-scaled circuits as in ZNE, and for each noise-scaled circuit, we generate ten near-Clifford circuits.

(iv) For ZNE+CDR, we first generate three noise-scaled circuits, as in ZNE, for each transpiled circuit. We then generate five near-Clifford circuits, as in CDR, for each noise-scaled circuit. Since we aim to provide a basic comparison of the ZNE+CDR and CDR+ZNE methods, from a resource-saving perspective we generate only five near-Clifford circuits (as in CDR) for each noise-scaled circuit. There are a total of 45 quantum circuits to be executed, as there are three transpiled circuits. The CDR error-mitigated results become the new results for the noise-scaled circuits and are then further mitigated by the quadratic polynomial extrapolation model.

(v) For CDR+ZNE, we use only the first transpiled circuit (the one with the measurement operator $O = Z^{\otimes 3}$) to generate five near-Clifford circuits. Based on each of these, we generate three noise-scaled circuits. There are a total of 15 quantum circuits to be executed.

(vi) Finally, for vnCDR, we use the same approach as eCDR to generate ten near-Clifford circuits, and for each near-Clifford circuit, we generate three noise-scaled circuits with λ_j values of approximately 1, 3, and 5. The generation of the error mitigation model in vnCDR follows its original version: the model is generated based on the expectation values of $\{\mathcal{T}_{m,\lambda_j}\}$. However, the model is then applied to the measurement results of $\{U_{\lambda_j}\}$ to obtain error-mitigated fidelity.

Due to the complexity of the quantum routers with a higher number of layers, we simplify the 3-layer router circuit to enhance the accuracy of the measurement results. We simplify the 3-layer router circuit by randomly selecting four control qubits to be in the superposition while setting the remaining control qubits to be in the state $|0\rangle_c$. Based on this setup for the control qubits, only certain path qubits are expected to contain the signal information at the output of the quantum router (these will be measured in the three basis). Among the control qubits, only those in superposition will be measured in the Z-basis.

6.3.2 Experimental Results of Extrapolated CDR

The experimental results of the 1 and 2-layer quantum routers with ZNE, CDR, eCDR, ZNE+CDR, and CDR+ZNE methods are demonstrated in Fig. 6.4. Note that although F_s is state-dependent, we have tested other signal states and observed similar experimental outcomes. The unmitigated experimental results are also illustrated for comparison. Each bar shows the averaged F_s from 20 repetitions (Unmitigated, ZNE, CDR, and eCDR), 2 repetitions (vnCDR), or 3 repetitions (ZNE+CDR and CDR+ZNE), and the error bars represent the standard deviation. We conduct fewer repetitions for the vnCDR, ZNE+CDR, and CDR+ZNE methods to provide a basic comparison. The primary focus of this work is the performance of eCDR in comparison to ZNE and CDR within the context of quantum routing. Although these error mitigation methods demonstrate similar error-mitigating performance for the 1-layer quantum routers, eCDR yields

significantly enhanced results compared to the other four methods for the 2-layer quantum router. Given the improved performance of eCDR in the 2-layer quantum router, the reason eCDR yields a lower fidelity result for the 1-layer quantum router compared to ZNE and CDR is that the unmitigated fidelity result is relatively high, providing limited potential for further improvement.

For the 3-layer quantum router, the unmitigated experimental result in terms of fidelity is approximately 0.5, and the ZNE, CDR, and eCDR methods are basically ineffective. These 3-layer mitigation results indicate that quantum error mitigation methods are ineffective when unmitigated results are very noisy. Mitigating errors for quantum circuits with large circuit depths remains a significant challenge. One potential direction in meeting this challenge could be a combination of quantum error mitigation with quantum error correction techniques. However, any introduction of quantum error correction will almost certainly require an advancement in current hardware to lower noise levels.

In addition to the five quantum error mitigation methods mentioned above, we also evaluated the performance of the ZNE+PEC method (the concatenation of ZNE and PEC) and the vnCDR method when applied to the quantum routers. The ZNE+PEC method slightly improves F_s for the 1-layer quantum router compared to the unmitigated fidelity, while it reduces F_s for the 2-layer quantum router. The vnCDR error-mitigated signal fidelities (averaged from 2 repetitions) for the multi-layer quantum routers are all slightly lower than the corresponding unmitigated signal fidelities. We found that the mitigation model (as described by Eq. (6.9)) generated in vnCDR varies significantly across repetitions.

The vnCDR method generates the mitigation model using noisy expectation values, and this model is then applied to measurement results for mitigation. The mitigation model in vnCDR is formed from near-Clifford data and can also be identified as an extrapolation model, which is typically employed in ZNE and constructed from noise-

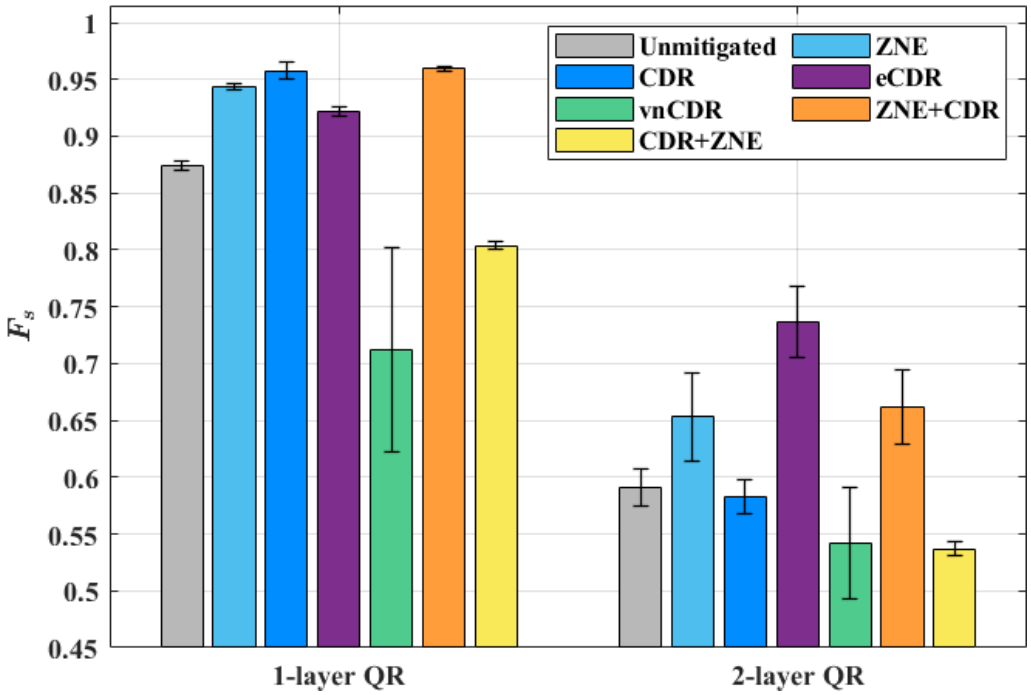

Figure 6.4: State fidelity, F_s, of the 1 and 2-layer quantum router with and without quantum error mitigation methods realized on *ibm_sherbrooke* device. QR stands for quantum router. Note that the fidelity results for Unmitigated, ZNE, CDR, and eCDR are averaged over 20 repetitions, the fidelity result for vnCDR is averaged over 2 repetitions, and the fidelity results for ZNE+CDR and CDR+ZNE are averaged over 3 repetitions. The error bars represent the standard deviation.

scaled experimental data. These mismatches could be the main reasons for the poor performance of vnCDR.

For ZNE, additional errors are more prone to be introduced to the noise-scaled circuits, $\{U_{\lambda_j}\}$, with higher complexity and larger value of λ_j when executed on the quantum device. As a result, λ_j may not accurately represent the noise ratio between the measurement results of U_{λ_j} and those of U, thereby decreasing the effectiveness of error mitigation for the 2-layer quantum router. Our eCDR method employs an extrapolated linear regression model (as shown in Eq. (6.8)) to estimate the relationship between noisy and noiseless measurement results of U. If the linear regression model generated by CDR can precisely describe the relationship — usually occurring when

unmitigated measurement results of U are close to the noiseless measurement results — further introducing extrapolations (which is the main step of eCDR) can add additional errors, resulting in worse outcomes. However, due to the fact that the unmitigated measurement results of the 2-layer router circuit are relatively noisy, the extrapolated linear regression model in eCDR provides a more accurate description of the relationship, rather than introducing additional errors.

6.4 Summary

In this work, we proposed a quantum error mitigation method, denoted as eCDR, which conceptually combines the characteristics of two promising error mitigation methods, ZNE and CDR. We embedded ZNE, CDR, and eCDR methods into the 1, 2, and 3-layer quantum routers to benchmark their performance conducted on a 127-qubit quantum device named *ibm_sherbrooke*. For the 1-layer quantum router, the three methods demonstrated a similar positive mitigation effect, whereas for the 2-layer quantum router, the eCDR method demonstrated superior performance compared to the other two methods. For the 3-layer quantum router, error mitigation was found to be ineffective. Our results indicate, in the context of quantum routing, the circuit depths below which error mitigation will be successful using current hardware.

Chapter 7

Error-Mitigated Quantum Random Access Memory

In Chapters 4 and 5, we have shown the performance of a QRAM with two memory cells on current quantum devices. In this chapter, we investigate the performance of a QRAM with eight memory cells using a modified version of ZNE for error mitigation on a 27-qubit quantum device named *ibm_cairo*. The two main contributions of this chapter are summarized as follows.

(i) We propose a modified version of ZNE, henceforth referred to as sZNE. We consider two different methods, within sZNE, of selecting the preferred extrapolation function, one based on some noisy estimate of the noiseless limit (from an independent method), and one independent of such a noisy estimate. The former method allows integration of sZNE with third-party algorithms, and the latter method provides a stand-alone solution.

(ii) We then embed ZNE and sZNE into a quantum device and experimentally deploy both algorithms in the context of QRAM (with quantum state tomography) in order to show their relative real-world performance (fidelity).

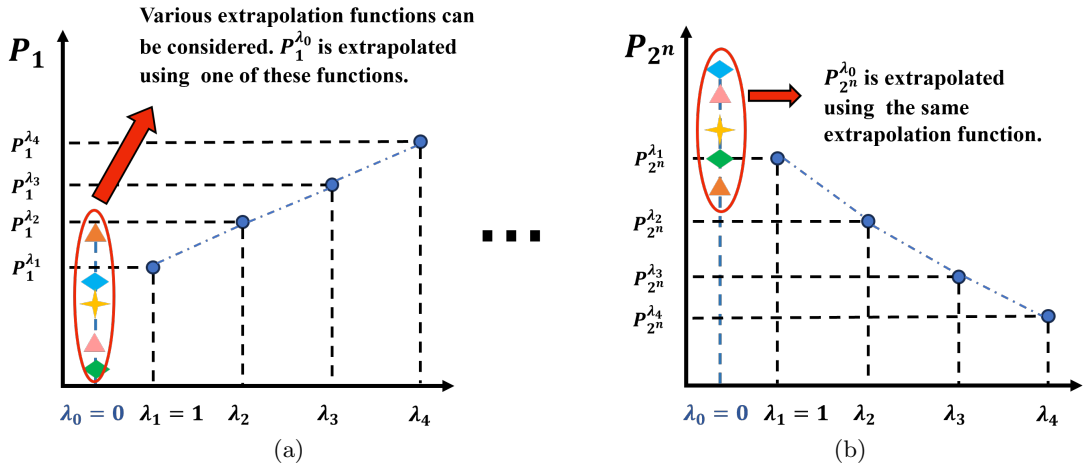

Figure 7.1: (a), (b) Schematic of ZNE shows how it calculates the zero-noise probabilities. The square dots between subfigures represent the intervening probabilities P_2 to P_{2^n-1}.

7.1 Overview

7.1.1 Zero Noise Extrapolation

ZNE is a quantum error mitigation method that involves running additional quantum circuits and classical post-processing of experimental data. The main idea of ZNE is to extrapolate the zero-noise expectation value of an operator from noise-scaled circuits at different noise levels [152]. The detailed working principle of ZNE is provided in Subsection 5.1.1.

Recall that O is an operator with expectation value $\langle O \rangle$ and discrete eigenvalues $\{a_x,\, x = 1, 2, \cdots, 2^n\}$, each associated with one of the 2^n eigenvectors. The measurement of O is applied to n qubits of the noise-scaled circuits, associated with the noise-scaling factors $\boldsymbol{\lambda} = [\lambda_1, \lambda_2, \cdots, \lambda_j, \cdots, \lambda_J]$. Note that the noise-scaled circuits are generated based on the original circuit of interest, U, and the probability of obtaining a_x as the measurement outcome with zero finite sampling error is P_x. After the execution of the noise-scaled circuits on the quantum device, the measurement results of these circuits are

collected. The measurement results of the noise-scaled circuit are probabilities denoted as

$$\boldsymbol{P_s^{\lambda}} = [\boldsymbol{P_s^{\lambda_1}}, \cdots, \boldsymbol{P_s^{\lambda_j}}, \cdots, \boldsymbol{P_s^{\lambda_J}}] = [\boldsymbol{P_1^{\lambda}}, \cdots, \boldsymbol{P_x^{\lambda}}, \cdots, \boldsymbol{P_{2^n}^{\lambda}}], \tag{7.1}$$

where $\boldsymbol{P_s^{\lambda_j}} = [P_1^{\lambda_j}, \cdots, P_x^{\lambda_j}, \cdots, P_{2^n}^{\lambda_j}]$ and $\boldsymbol{P_x^{\lambda}} = [P_x^{\lambda_1}, \cdots, P_x^{\lambda_J}]$. We separately define the zero-noise probabilities $\boldsymbol{P_s^{\lambda_0}} = [P_1^{\lambda_0}, \cdots, P_x^{\lambda_0}, \cdots, P_{2^n}^{\lambda_0}]$, where $\lambda_0 = 0$, and we set $\Lambda \in \{\lambda_0, \lambda_1, \cdots, \lambda_J\}$. The process of finding $\boldsymbol{P_s^{\lambda_0}}$ via extrapolation is illustrated in Fig. 7.1(a) and Fig. 7.1(b). Note that in the entire process of ZNE, only one extrapolation can be considered. The least square method is typically utilized to find the best-fit parameters of a chosen extrapolation function.

Originally, ZNE was proposed with Richardson extrapolation [28], and this remains a commonly used extrapolation function in ongoing studies of ZNE [32, 33, 35]. Beyond Richardson extrapolation, other functions can be used, including linear, polynomial, poly-exponential, and exponential extrapolation [31]. Given an extrapolation function, there are two approaches to extrapolate the zero-noise expectation value $\langle O \rangle^{\lambda_0}$ using $\boldsymbol{P_s^{\lambda}}$. One approach is applying the extrapolation function to noisy expectation values, denoted as $\boldsymbol{\langle O \rangle^{\lambda}} = [\langle O \rangle^{\lambda_1}, \cdots, \langle O \rangle^{\lambda_j}, \cdots, \langle O \rangle^{\lambda_J}]$. Note that $\langle O \rangle^{\lambda_j}$ is calculated from $\boldsymbol{P_s^{\lambda_j}}$ using Eq. (5.1). Another approach involves applying the extrapolation function to $\boldsymbol{P_x^{\lambda}}$ to obtain $P_x^{\lambda_0}$, and then calculating $\langle O \rangle^{\lambda_0}$ using $\boldsymbol{P_s^{\lambda_0}}$ via Eq. (5.1). Both approaches yield the same value for $\langle O \rangle^{\lambda_0}$ since the same extrapolation function is utilized.

From the working process of ZNE, it is evident that multiple assumptions must hold true for ZNE to provide an effective error-mitigated result. In digital ZNE, a critical assumption is that the noise in a quantum device can be amplified by folding unitary gates in U, implying that the noise is assumed to be incoherent errors [31]. Incoherent errors are associated with independent gate errors and decoherence. The execution time of the noise-scaled circuit increases with its circuit depth, resulting in greater decoherence. Other types of errors, such as coherent errors and measurement errors, may not be amplified by global and unitary folding. Coherent errors might be

canceled by adding the inverse of a unitary gate. Other methods, including randomized compiling and twirling [159, 160], can be considered for mitigating coherent errors. We note measurement errors are unrelated to the circuit depth.

In ZNE, the circuit depth of the noise-scaled circuit is independent of the number of qubits in U. In digital ZNE with global folding, the circuit depth of the noise-scaled circuit increases linearly with the number of gates in U. In digital ZNE with local folding, the circuit depth of the noise-scaled circuit is determined by its noise-scaling factor, λ_j. In ZNE, the best choice of the extrapolation function with its best-fit parameters is unknown *a priori*. The accuracy of the extrapolated values depends on the quantity and accuracy of the input data injected into the extrapolation function. Generally, having more noise-scaled circuits with a wider range of circuit depths can improve the accuracy of extrapolation. This is because a greater amount of the input data across a broader range allows for better identification of curve-fitting patterns and trends, leading to higher accuracy in selecting the extrapolation function and its parameters. Beyond quantity, the accuracy of the input data in demonstrating the amplification of the noise is also crucial. Moreover, extrapolation can be unreliable when the input data have critical fluctuations and/or the chosen function is a high-order polynomial extrapolation function [161]. These problems limit the power of ZNE and lead to the fact that $\langle O \rangle^{\lambda_0}$ extrapolated via ZNE can be inaccurate at times [35].

7.1.2 Bucket Brigade Quantum Random Access Memory

We consider a tomography application that includes QRAM to benchmark and study the performance of ZNE implemented on the quantum device. The critical advantage of QRAM is that multiple classical and/or quantum data stored in memory cells can be queried in superposition. A QRAM query can be expressed as

$$\sum_{d=0}^{N-1} \alpha_d |d\rangle|0\rangle \xrightarrow{\text{QRAM}} |\Psi\rangle_f = \sum_{d=0}^{N-1} \alpha_d |d\rangle|D_d\rangle, \tag{7.2}$$

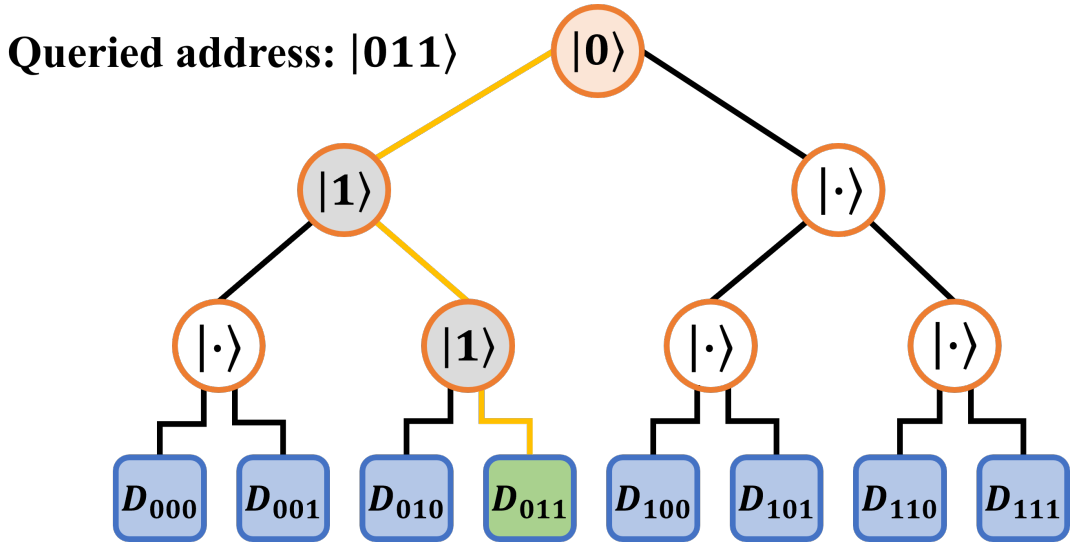

Figure 7.2: Bucket brigade scheme for a QRAM with eight memory cells. The binary tree nodes are initialized to the $|\cdot\rangle$ state, which is a waiting state. The queried address qubits $|011\rangle$ are read by the tree nodes sequentially, and the nodes that receive the address qubits will be activated and changed to the received qubits. The activated tree nodes generate a route to the memory cell D_{011}.

where N is the number of the memory cells, α_d is the amplitude of each address $|d\rangle$ in the superposition, and $|D_d\rangle$ represents the data stored in the memory cell addressed $|d\rangle$. [1] One of the most robust designs for QRAM is the bucket brigade scheme, which requires a binary tree for querying addresses [141]. A bucket brigade QRAM scheme with eight memory cells is schematically depicted in Fig. 7.2. In this QRAM, the binary tree has seven tree nodes, each of which makes a binary decision. Each binary tree node is a three-level system (a qutrit) with states $|\cdot\rangle$, $|0\rangle$, and $|1\rangle$, where the $|\cdot\rangle$ state is called the waiting state. In this three-level system, each tree node is initialized to the waiting state. The queried address qubits are injected into the tree nodes from the root node, and the tree nodes read the address qubits sequentially to generate routes to the queried memory cells. If the tree node receives the $|0\rangle$ state (the $|1\rangle$ state), this node activates the left (right) child, which can be either one of the next-level tree nodes or one of the

[1] Note that in this chapter, $|\Psi\rangle_f$ represents the output of the QRAM with eight memory cells, while in Chapters 4 and 5, $|\Psi\rangle_f$ stands for the output of the QRAM with two memory cells.

memory cells. If the queried address is $|011\rangle$, the root node reads the first address qubit, which is in the state $|0\rangle$. Then, the chosen second and third-level nodes read the rest of the two qubits sequentially. After this reading process, the data stored in the memory cell, labeled as D_{011}, is accessed.

Based on this QRAM scheme, we construct a bucket-brigade style QRAM circuit (with QST added), as illustrated in Fig. 7.3. The entire circuit includes 20 qubits initialized to the $|0\rangle$ state, including three address qubits, eight tree-node qubits, eight memory qubits, and one output qubit. The first three qubits (read from the top) are the address qubits that contain the addresses intended to be queried. Each address qubit is prepared to the state $|+\rangle = (|0\rangle + |1\rangle)/\sqrt{2}$ via a Hadamard gate, indicating the queried addresses are $|000\rangle$, $|001\rangle$, $\cdots$, and $|111\rangle$, *i.e.*,

$$\sum_{d=0}^{N-1} \alpha_d |d\rangle = (|000\rangle + \cdots + |111\rangle)/2\sqrt{2}. \tag{7.3}$$

The next eight qubits are the tree-node qubits, where the second tree-node qubit is prepared to the $|1\rangle$ state, and the rest to the $|0\rangle$ state. Since qutrits cannot be implemented on the IBM quantum device, we utilize eight qubits instead of seven qutrits to act as the seven tree nodes (of Fig. 7.2). The next eight qubits of Fig. 7.3 represent the memory cells (corresponding to the memory cells D_{000} to D_{111} of Fig. 7.2), each containing a quantum state or a classical state. The last qubit is an output qubit containing all of the queried data after the QRAM query.

Typically, once the output qubit acquires all of the queried data, the states of the binary tree nodes will be reversed to their initial state. This step can be done by implementing the CX and CCX gates in the QRAM circuit in reverse order, or by re-setting each tree node to the $|0\rangle$ state and implementing the X gate to the second tree-node qubit. For simplicity, we ignore this simple step in the QRAM circuit. To benchmark the performance of the QRAM, we apply QST to the four "tomography qubits" - the three address qubits and the output qubit - to reconstruct $|\Psi\rangle_f$. Note that QST is represented by the gray boxes in Fig. 7.3, and the details on the implementation

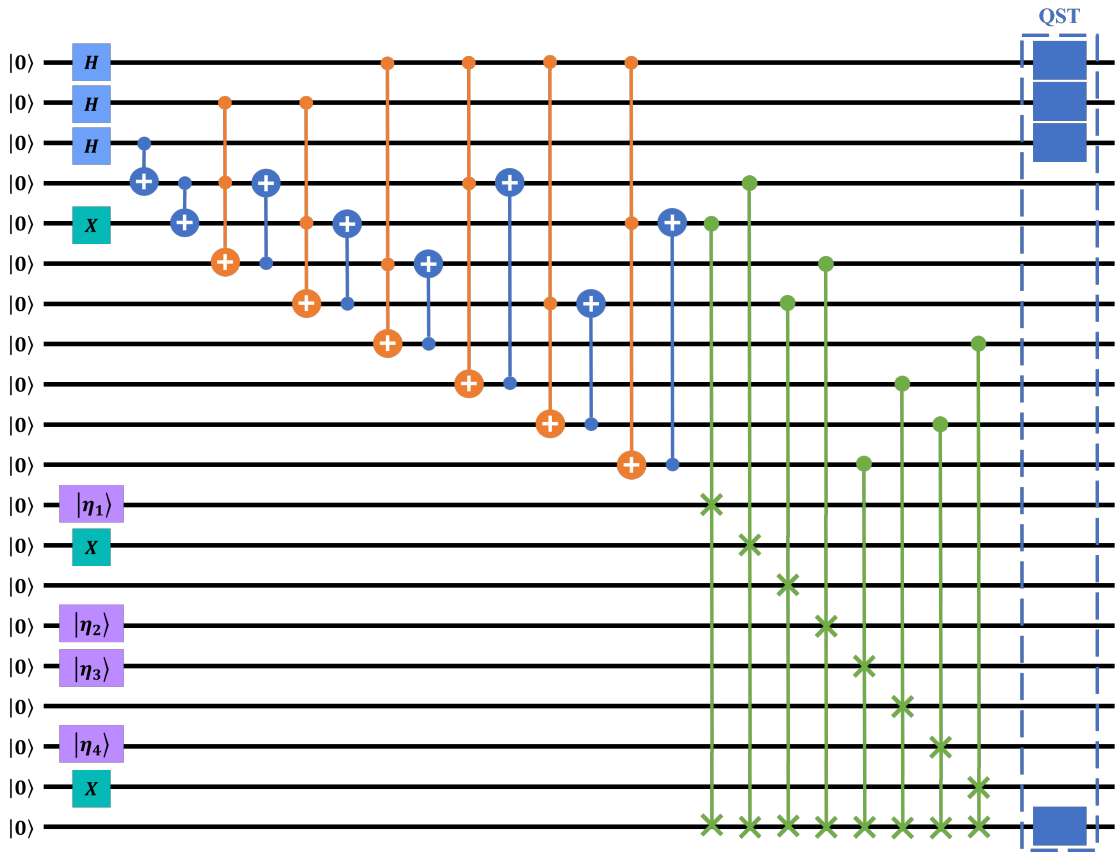

Figure 7.3: Quantum circuit of a bucket-brigade style QRAM with QST. The four purple gates indicate state preparations of four random quantum states, namely, $|\eta_1\rangle$, $|\eta_2\rangle$, $|\eta_3\rangle$, and $|\eta_4\rangle$. The H represents the Hadamard gate, and the X is the NOT gate. The two-qubit gates in blue stand for CX gates. The three-qubit gates in orange and green are CCX and controlled-swap gates, respectively. The four gray boxes with the dashed line indicate that QST is applied to these four qubits.

of QST are provided in Subsection 2.1.3. In our experiments, this QRAM tomography application is employed with ZNE or sZNE embedded into it.

7.2 The Selected-Zero-Noise Extrapolation Method

To benchmark the performance of ZNE embedded into the bucket brigade QRAM, we again use the fidelity, F', between $\kappa' = |\Psi\rangle_f\langle\Psi|$ and κ as our main performance metric, as shown in Eq. (4.6). In this chapter, κ' is the theoretical density matrix of the output of the QRAM with eight memory cells, and κ is the experimental density matrix of $|\Psi\rangle_f$ reconstructed by QST. In our experiments, U is the QRAM circuit which excludes QST. For the execution of QST (see Subsection 2.1.3), 81 tomography circuits with distinct measurement operators are generated. These measurement operators are $\{O_g\}_{g=1}^{81} = \{O_1 = X \otimes X \otimes X \otimes X, O_2 = X \otimes X \otimes X \otimes Y, \cdots, O_{81} = Z \otimes Z \otimes Z \otimes Z\}$, and each O_g has 16 eigenvectors (*i.e.*, 16 P_x) as four qubits are measured. Transpilation is necessary to execute the tomography circuits on the quantum device (see details in Subsection 2.2.2.2). The 81 tomography circuits are then transformed to 81 transpiled tomography circuits ($\mathbb{U}_1$ to $\mathbb{U}_{81}$).

In contrast to ZNE, which applies a chosen extrapolation function to noisy expectation values, the modified version we introduce here, sZNE, considers multiple extrapolation functions to obtain zero-noise probabilities of a measurement producing a specific eigenvalue, a_x, of a quantum operator possessing 2^n eigenvectors. The main steps of sZNE are as follows.

(i) Generate J noise-scaled circuits with $\boldsymbol{\lambda}$, based on $\mathbb{U}_1$ (for example) using global or local folding.

(ii) Execute the J noise-scaled circuits on the quantum device and collect their measurement results, which are $\boldsymbol{P_s^{\lambda}}$.

(iii) Choose an extrapolation function for each $\boldsymbol{P_x^{\lambda}}$ and perform the extrapolation accordingly, as shown in Fig. 7.1(a) and Fig. 7.1(b). Note that the extrapolation function selected for $\boldsymbol{P_1^{\lambda}}$ and $\boldsymbol{P_2^{\lambda}}$ (for example) can be different.

(iv) From the different extrapolated probabilities, determine a final zero-noise probability for each eigenvector.

(v) Using the calculated zero-noise probabilities, $\boldsymbol{P_s^{\lambda_0}}$, compute a performance metric of choice suited to the application under study.

As already indicated, for step (v) our application will be QRAM and our metric will be fidelity (other applications and metrics could also be studied). In principle, an infinite number of extrapolation functions can be used, but in practice, only a limited number can be accessed. In our experiments, we attempt Richardson extrapolation, linear extrapolation, and polynomial extrapolation with orders two and three. Richardson extrapolation is a special case of polynomial extrapolation with order $J-1$ [31].

The fundamental idea of sZNE involves exploring various extrapolation functions for each $\boldsymbol{P_x^{\lambda}}$, with different functions selected to calculate them. In contrast, ZNE exclusively employs the same extrapolation function for each $\boldsymbol{P_x^{\lambda}}$. However, using the same extrapolation function may result in the introduction of additional errors. Addressing this limitation of ZNE is the main aim of the proposed sZNE. Since the expectation value is computed based on P_x, as shown in Eq. (5.1), it is intuitive that minimizing errors in each P_x should improve any performance metric of an application that involves the use of these probabilities. Defining that the error between $P_x^{\lambda_0}$ and noiseless simulation results P_x^{sim} as $e_x = \left|P_x^{\lambda_0} - P_x^{sim}\right|$, we seek to understand how application performance metrics scale with e_x.

The remaining task is to identify the method utilized to determine the zero-noise probabilities in step (iv). There are many possibilities for this. Here, we focus on two different methods: the first method involves selecting each zero-noise probability based

on a noisy estimate of the noiseless probability (termed the noisy estimator algorithm), and the second method uses a filter function to eliminate over-fitted solutions and calculate the zero-noise probabilities based on the solutions that pass the filter (termed the filter function algorithm). We describe these two methods in more detail.

7.2.1 Noisy Estimator Algorithm

Consider the availability of a noisy estimate, denoted as $P_{g,x}^{est}$, of the noiseless probability associated with measurement operator O_g and eigenvalue a_x. This estimate could arise from several means, sources and techniques unrelated to ZNE - for our purpose it does not matter. We simply assume its availability and adopt no knowledge of its reliability (error). This represents a generic method of encapsulating a solution from a technique independent of ZNE into a new solution partially based on ZNE. For each O_g, we propose to select the zero-noise extrapolated probability for each P_x as given by

$$P_{g,x}^{\text{sZNE}} = \arg\min_{P \in L} \left| P - P_{g,x}^{est} \right|, \tag{7.4}$$

where $P_{g,x}^{\text{sZNE}}$ is the extrapolated probability with the selected extrapolation function, and $L = \{P_{g,x}^{\lambda_1}, P_{g,x}^{\lambda_0,f_1}, P_{g,x}^{\lambda_0,f_2}, P_{g,x}^{\lambda_0,f_3}, P_{g,x}^{\lambda_0,f_4}\}$, where f_1 to f_4 indicate linear, polynomial extrapolation of orders 2 and 3, and Richardson extrapolation functions, respectively. Note that for each O_g, the values in the set $\{P_{g,x}^{\lambda_0,f_1}\}_{x=1}^{16}$ are normalized (the same applies to other sets with different extrapolation functions), and the values in the set $\{P_{g,x}^{\text{sZNE}}\}_{x=1}^{16}$ are normalized again before reconstructing ρ'. We further refer to the method with the case where L excludes $P_{g,x}^{\lambda_1}$ as sZNE$'$ to distinguish it from sZNE. Various solutions, including Clifford simulators and the CDR method, can be considered to determine P_x^{est}, as discussed in detail in Appendix B.2. However, for simplicity, we generate this estimate by introducing Gaussian noise with variance σ^2 to the noiseless simulation results, $P_{g,x}^{sim}$. That is,

$$P_{g,x}^{est} = P_{g,x}^{sim} + \epsilon, \tag{7.5}$$

where in this chapter, ϵ is a random variable given by a zero-mean Gaussian distribution, *i.e.*, $\epsilon \sim \mathcal{N}(0, \sigma^2)$.

7.2.2 Filter Function Algorithm

For each P_x in every O_g, we obtain the set $\mathbb{T}_{g,x} = \{P_{g,x}^{\lambda_0,f_1}, P_{g,x}^{\lambda_0,f_2}, P_{g,x}^{\lambda_0,f_3}, P_{g,x}^{\lambda_0,f_4}\}$. There are a total of 81×16 $\mathbb{T}_{g,x}$, and the values in each $\mathbb{T}_{g,x}$ are passed through a filter function. The filter function has following requirements: (i) We delete any elements (extrapolated probabilities) in $\mathbb{T}_{g,x}$ that are smaller than zero since probabilities cannot be negative. (ii) If $P_{g,x}^{\lambda_1} \geq P_{g,x}^{\lambda_J}$, then we delete the elements in $\mathbb{T}_{g,x}$ that are smaller than $P_x^{\lambda_1}$. (iii) If $P_{g,x}^{\lambda_1} < P_{g,x}^{\lambda_J}$, then we delete the elements in $\mathbb{T}_{g,x}$ that are larger than $P_{g,x}^{\lambda_1}$. After the filtering, we store the remaining extrapolated probabilities in the set $\mathbb{T}'_{g,x}$. Finally, we calculate the zero-noise extrapolated probabilities following

$$P_{g,x}^{\text{filter}} = \left(\max L' + \min L'\right)/2. \tag{7.6}$$

Note that the value of $P_{g,x}^{\text{filter}}$ is obtained by averaging the maximum and minimum values in the set L', where $L' = \{P_{g,x}^{\lambda_1}, \mathbb{T}'_{g,x}\}$. After obtaining $P_{g,x}^{\text{filter}}$ for each x, the values in the set $\{P_{g,x}^{\text{filter}}\}_{x=1}^{16}$ are normalized. Finally, we use the 81×16 normalized zero-noise extrapolated probabilities to reconstruct ρ' and then calculate F' (see Subsection 2.1.3).

7.3 Experimental Results

We embed ZNE and sZNE into the tomography application containing QRAM to investigate their performance when implemented on *ibm_cairo*. To be executed on this quantum device directly, the 81 tomography circuits are transpiled to the transpiled tomography circuits first. In our experiments, $\boldsymbol{\lambda} = [1, 1.4, 1.7, 2.1, 2.5]$ and we fold gates locally at random to generate the noise-scaled circuits, where each transpiled tomography circuit is converted to five transpiled noise-scaled tomography circuits. The transpilation process

Table 7.1: Detailed Information of the Memory Data

Quantum State	α	β
$\|\eta_1\rangle$	$0.82 + 0.26i$	$0.43 - 0.28i$
$\|\eta_2\rangle$	$-0.62 + 0.51i$	$-0.15 - 0.57i$
$\|\eta_3\rangle$	$0.25 + 0.74i$	$0.31 + 0.54i$
$\|\eta_4\rangle$	$0.44 + 0.56i$	$-0.59 - 0.38i$

is realized via Qiskit, and Mitiq [155] is utilized to generate the noise-scaled circuits and to implement extrapolation functions. Each transpiled noise-scaled tomography circuit is executed $C_{tot} = 10,000$ times on the quantum device.

Note, the eight qubits corresponding to the memory cells D_{000} to D_{111} of Fig. 7.2, must be initialized. In the results shown here we have adopted a memory allocation given by $|\eta_1\rangle$, $|1\rangle$, $|0\rangle$, $|\eta_2\rangle$, $|\eta_3\rangle$, $|0\rangle$, $|\eta_4\rangle$, and $|1\rangle$ (as shown in Fig. 7.3), where $|\eta_1\rangle$ to $|\eta_4\rangle$ are four random quantum states. Each one of these four quantum states can be represented by $\alpha|0\rangle + \beta|1\rangle$: the selected α and β of the four quantum states stored in the memory cells are given in Table 7.1.

7.3.1 Noisy Estimator Results

We consider the results from the noisy estimator algorithm. We first consider the $\epsilon = 0$ case in sZNE. Clearly, this case holds no value for mitigation (if we knew the zero-noise probability exactly, there is no need for mitigation). However, we use it here merely to evaluate the significance of employing proper extrapolation functions to the noisy probabilities. The fidelity results of the tomography application that includes the QRAM with eight memory cells are illustrated in Fig. 7.4, and we see that sZNE$'$ and sZNE provide for enhancement in F', it being increased from 0.4 to 0.79 and 0.85, respectively. The fidelity result of sZNE indicates the optimal performance of the QRAM tomography application that ZNE can achieve if a proper extrapolation function is applied to each P_x.

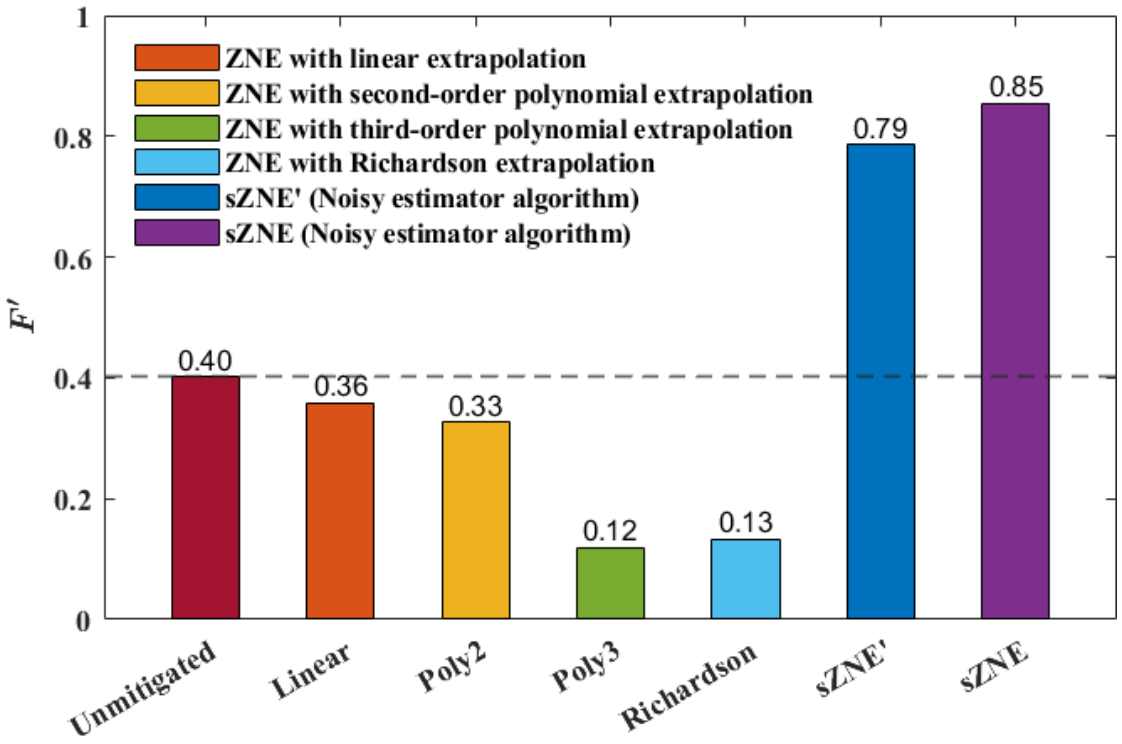

Figure 7.4: F' of the QRAM with eight memory cells with or without quantum error mitigation obtained from *ibmq_cairo*. The sZNE$'$ and sZNE results are calculated with $\epsilon = 0$ and in effect only show the importance of selecting the correct extrapolation function - in reality, the performance shown cannot be achieved since ϵ is always non-zero. Note that the horizontal dashed line indicates the unmitigated F' for reference.

We next conduct sZNE$'$ and sZNE with $P_{g,x}^{est}$, which is generated by introducing the Gaussian noise to the noiseless simulation results. This represent a more real-world scenario in which an independent estimate of the noiseless probability value is made available. We wish to explore what constraints must be imposed on the noisy estimation in order for our mitigation method to offer advantages in QRAM fidelity. The results are shown in Fig. 7.5, where each circle represents a fidelity result averaged from $1,000$ repetitions. We see that sZNE provides improved fidelity results if σ is smaller than approximately 0.03.

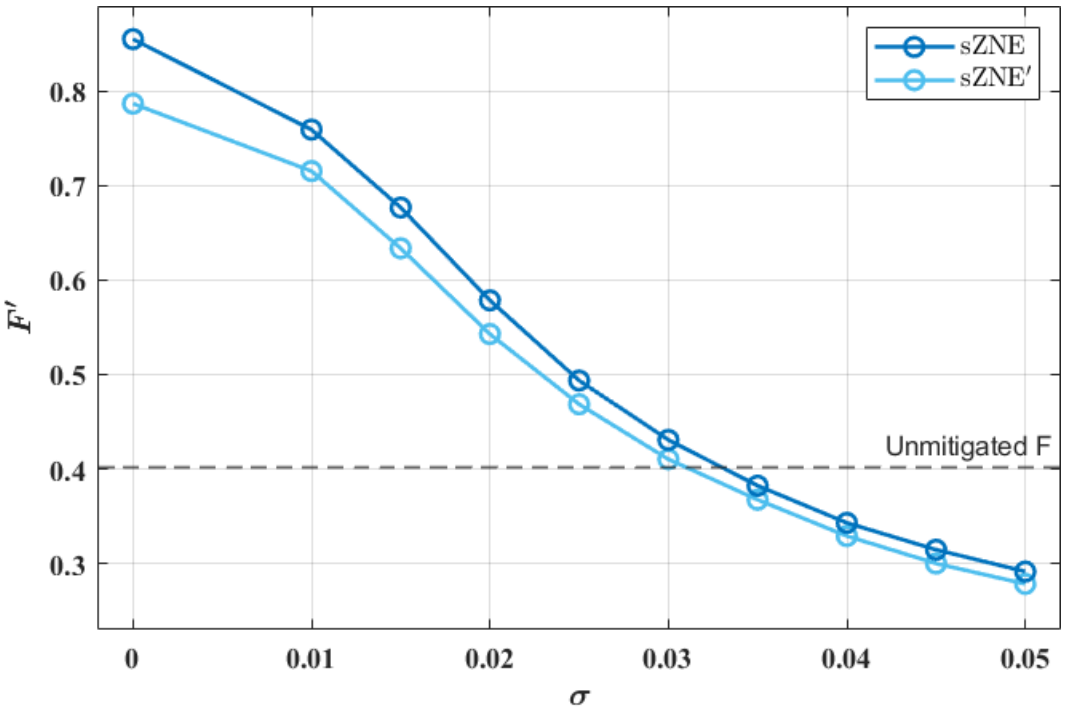

Figure 7.5: F' of the QRAM with eight memory cells as a function of the standard deviation, σ, of the Gaussian noise for sZNE′ and sZNE. These results represent a more realistic scenario with $\epsilon \neq 0$. The dashed line shows the unmitigated results.

Table 7.2: Experimental Results of the Filter Function Algorithm

	Fidelity	$\{\langle O_g \rangle\}_{g=1}^{81}$ Performance
Filter Function Algorithm	0.48	19%

7.3.2 Filter Function Results

We consider the results from the filter function algorithm, as shown in Table 7.2. We see that this algorithm improves the fidelity result of the QRAM tomography application from 0.4 to 0.48, which is the main result of this paper. This represents a 20% improvement in the key metric of our application, and shows the merit of our approach. Since the expectation value of an observable is the typical performance metric used in quantum error mitigation, we also demonstrate the performance of the filter function algorithm in terms of $\langle O_g \rangle$, compared to the unmitigated values. Using the filter function algorithm,

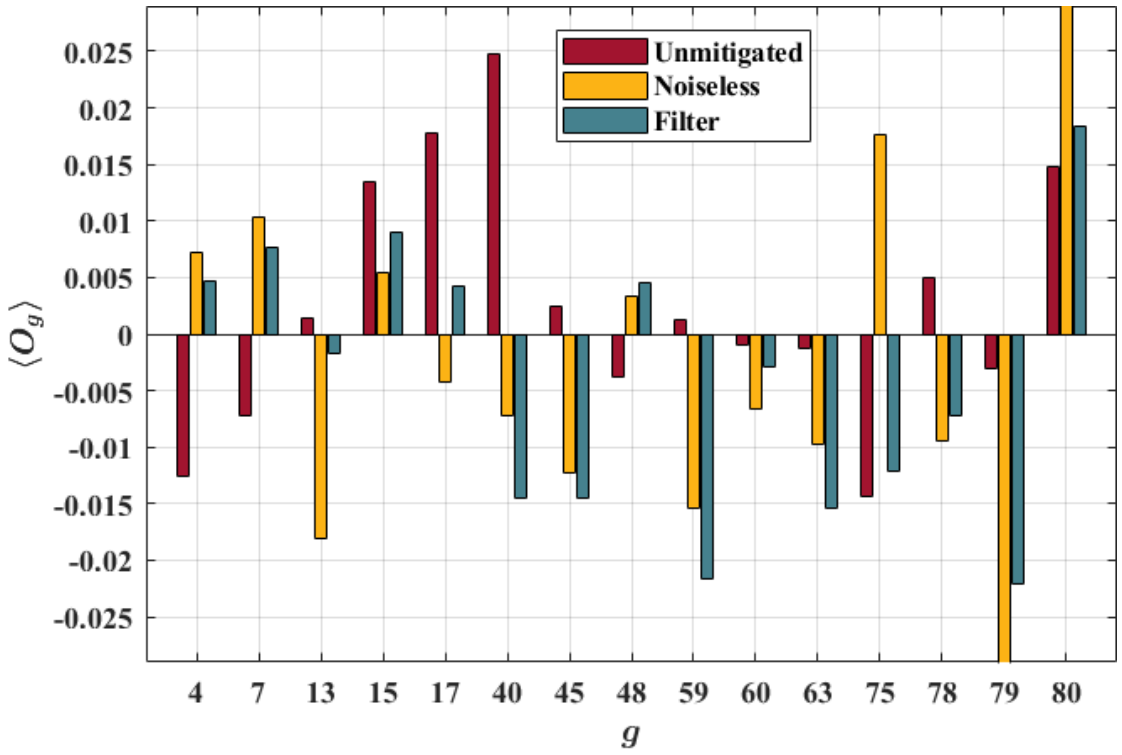

Figure 7.6: Expectation values of O_g with and without the filter function algorithm. The noiseless expectation values calculated via $P_{g,x}^{sim}$ are shown for reference. Only 15 of the 81 expectation values, where the error-mitigated values (using the filter function algorithm) are closer to the corresponding noiseless ones compared to the unmitigated values, are illustrated.

we find only 15 error-mitigated expectation values (see Fig. 7.6) among the 81 $\langle O_g \rangle$ are closer to their corresponding noiseless values - a 19% performance level.

From the above discussion, we learn that using the unmitigated $\langle O_g \rangle$ directly produces better results overall in determining expectation values, relative to our new filter function algorithm. This is in contrast to the result achieved when looking at the performance metric of our application directly, the fidelity. This counter-intuitive result illustrates the advantage of our algorithm. Negating the traditional use of ZNE and its focus on expectation values of observables, but rather bypassing these values and focusing on the performance metric of the application instead can produce useful outcomes.

7.4 Summary

In this chapter, we introduced a modified ZNE, referred to as sZNE, and applied it to a QRAM application with quantum state tomography on a NISQ device. Novel in our approach was a focus on application performance metrics in the design process rather than on expectation values as in standard ZNE. A specific new element was our direct use of extrapolated zero-noise probabilities, which are directly coupled to QRAM fidelity, thereby circumventing the need for expectation values of operators. To implement a QRAM with multiple memory cells on a 27-qubit quantum device, we first conducted sZNE coupled to an algorithm based on a noisy estimate of the noiseless probability available from an independent technique. As the error in that estimate approached zero, our calculations reduced to a study in how a judicious choice of extrapolation function on a per measurement basis can dramatically improve the ZNE technique. Additional experimental results demonstrated the noise threshold below which this form of sZNE is effective. We then coupled our sZNE method to an algorithm that did not require an independent noisy estimate on the noiseless probability, but rather one based on avoidance of over-fitting and subsequent use of the remaining extrapolated probabilities, showing how significant fidelity gain in our QRAM application can be found.

Chapter 8

Conclusions

In this thesis, we investigated the performance of quantum error correction and mitigation methods when applied to quantum routing applications with state tomography on current superconducting quantum devices. Specifically, the quantum routing applications include quantum routers and QRAM, which are important elements for building near-term quantum networks.

In Chapter 3, we investigated the performance of quantum-error-corrected routing with the consideration of a specific noisy channel. Our experimental results first verified the quantum nature of the router, and then demonstrated the viability of error-corrected quantum routing with use of statistical information. Note that the quantum error correction method utilized in this chapter can only correct particular errors, as it was designed for the specific noisy channel, which was artificially added to mimic the noisy transmission of quantum signals.

In Chapter 4, we considered a general scenario for quantum error correction: a five-qubit QECC capable of correcting any single-qubit errors was embedded into the quantum router. We benchmarked the quantum router's performance considering only the intrinsic errors of the quantum device; that is, no artificial noisy channels were

added. Our experimental results highlighted the challenges encountered by such error correction when implemented on NISQ devices. In this chapter, we also demonstrated the feasibility of QRAM, which is an application of quantum routing.

Given the unsatisfied performance of quantum error correction on current quantum devices, we started to investigate quantum error mitigation in Chapter 5. Two promising quantum error mitigation methods, ZNE and PEC, and their concatenation were embedded within the quantum router. The experimental result of the concatenation of ZNE and PEC demonstrated that the fidelity of the quantum router was impressively increased to effectively unity. Although additional executions of ancillary quantum circuits and classical post-processing are required by quantum error mitigation methods, our results showed the critical role such methods can play for quantum applications executed on current noisy devices.

In Chapter 6, we conceptually combined the characteristics of two well-known error mitigation methods, ZNE and CDR, by proposing a new quantum error mitigation method, denoted as eCDR. We investigated the performance of ZNE, CDR, and eCDR methods by embed them into the 1, 2, and 3-layer quantum routers. The three methods demonstrated similar positive mitigated results for the 1-layer quantum router, whereas for the 2-layer quantum router, the eCDR method demonstrated superior performance compared to the other two methods. We found that error mitigation was ineffective for the 3-layer quantum router, which has a larger circuit depth compared to the circuits of the other two layers. Our results indicate the circuit depth below which error mitigation will be effective for multi-layer quantum routers implemented on current hardware.

In Chapter 7, we investigated the performance of QRAM, a quantum routing application, and introduced a modified ZNE, referred to as sZNE. We applied sZNE to a QRAM with eight memory cells with QST on a 27-qubit quantum device. We considered two different algorithms inside sZNE to select the preferred extrapolation function. One algorithm was based on a noisy estimate of the noiseless probability, and another

was designed to use extrapolated probabilities after excluding overfitted ones. Our results demonstrated the effect of a judicious choice of extrapolation function for each measurement basis on the performance of ZNE.

Our work implicates that the performance and scalability of quantum routing applications are limited by the intrinsic errors of quantum hardware. Quantum error mitigation is an effective approach for overcoming this limitation in the implementation of quantum routers on NISQ devices. Therefore, the additional resources and time consumption required by quantum error mitigation should be considered in the design of quantum routing applications. Moreover, quantum devices with improved characteristics are essential for the reliable implementation of large-scale quantum routers and QRAMs.

In this thesis, quantum error mitigation methods demonstrated their effectiveness for quantum routing applications on current quantum devices. However, quantum error mitigation is generally unfeasible for quantum circuits with large circuit depths and/or a significant number of qubits. To resolve this issue, several future directions could be considered. One potential direction for implementing workable quantum applications on NISQ devices is the integration of quantum error mitigation with error correction techniques. This approach could reduce the requirement of ancillary qubits and additional executions of ancillary circuits. Additionally, machine learning [145, 162] could be employed to build the noise models of current quantum devices and optimize quantum error mitigation methods designed for specific quantum applications. Moreover, compared to superconducting qubits, photons exhibit longer coherence times [51–53]. Among photonic qubits, dual-rail qubits [163, 164] are considered robust candidates for encoding quantum information. Therefore, employing photonic systems with dual-rail qubits for quantum routing applications could also be a potential approach to improving performance.

In the NISQ era, quantum error mitigation is likely to remain a critical method for

near-term quantum applications. Improving and benchmarking error mitigation methods will remain important tasks and will ensure near-term quantum devices continue to play a constructive role in the path towards full fault-tolerant quantum computing. We believe the results shown in this thesis illustrate that deviations from established pathways for error mitigation still hold promise in this regard, especially if the focus is on the application metrics of interest.

Appendix A

Quantum State Tomography on Noisy Devices

QST is a fundamental technique to reconstruct the density matrix of a quantum state based on experimentally measurements [165] and is also considered the gold conventional for benchmarking NISQ devices that are now available [102]. In this appendix, we present a modification of the conventional QST algorithm (introduced in Subsection 2.1.3) to improve the efficiency of QST execution. We experimentally apply the conventional QST to several quantum states on *ibmq_jakarta*, a seven-qubit superconducting quantum device provided by the IBM Quantum platform [66]. We compare the performance of the conventional and modified QST algorithms in terms of fidelity by applying them to a 3-qubit maximally entangled state, denoted as the $|\text{GHZ}\rangle_3$ state, on the quantum device. We further apply QST to a practical quantum application, an entanglement distillation protocol [166] - a protocol designed to convert a set of noisy entangled states to a smaller set of less-noisy states (using local operations and classical communication only). This provides additional focus on the actual use of QST as well as additional performance insights. Note that, unless otherwise specified, all experimental results in this appendix are first processed by the MEM method introduced in Subsection 2.3.2.1.

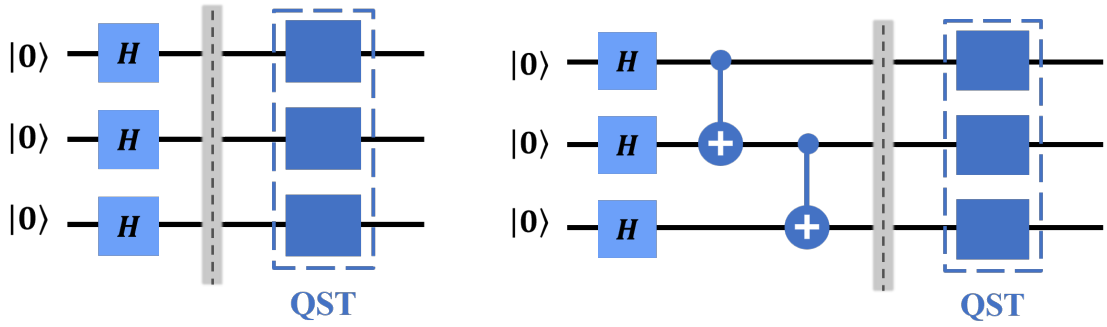

(a) (b)

Figure A.1: Quantum circuits for building the $|+\rangle_3$ state (a) and the $|\mathrm{GHZ}\rangle_3$ state (b) with QST. All qubits start from the $|0\rangle$ state, H stands for the Hadamard gate, the two-qubit gate is the CX gate, and the blue boxes with a blue dashed line represent QST.

A.1 Quantum States with State Tomography

To test the performance of QST on the quantum device, we first conduct an experiment with five well-known states, namely, $|+\rangle$, $|+\rangle_2 = |+\rangle|+\rangle$, $|+\rangle_3 = |+\rangle|+\rangle|+\rangle$, $|\Phi^+\rangle = (|00\rangle + |11\rangle)/\sqrt{2}$, and $|\mathrm{GHZ}\rangle_3 = (|000\rangle + |111\rangle)/\sqrt{2}$. Quantum circuits constructing $|+\rangle_3$ and $|\mathrm{GHZ}\rangle_3$ with QST are demonstrated in Fig. A.1. Similar diagrams can be drawn for the other states. Note that the first three states ($|+\rangle$, $|+\rangle_2$, and $|+\rangle_3$) are product states (non-entangled states), and the other two states ($|\Phi^+\rangle$ and $|\mathrm{GHZ}\rangle_3$) are entangled states. We define ρ' to be a density matrix of a quantum state under a noise-free environment, and ρ for the density matrix of the same quantum state in the quantum device reconstructed by QST. We refer to ρ' and ρ as the theoretical density matrix and the experimental density matrix, respectively.[1] We chose the fidelity $F = \left(\mathrm{Tr}\sqrt{\sqrt{\rho}\,\rho'\sqrt{\rho}}\right)^2$ as our performance metric, which can be considered a measure of the similarity between ρ' and ρ.

[1]Note that ρ' and ρ previously represented the density matrices of the quantum router output (see Eq. (3.10)). In this appendix, however, ρ' and ρ stand for the theoretical and experimental density matrices for one of the five states or as specifically defined for the entanglement distillation protocol.

To reconstruct a n-qubit state, we need a minimum of 3^n projective measurements, which are the tensor products of the Pauli measurement operators (see more details in Subsection 2.1.3). In our experiments, each of the 3^n projective measurements of the QST is conducted $N' = \{1 \times 10^3, 1 \times 10^4, 1 \times 10^5\}$ times first.[2] We refer to the procedure of conducting QST with $3^n N'$ shots[3] and calculating F as one "run." Because *ibmq_jakarta* has the shots limit of 10^5, we implement five runs and take the average for each chosen N' value, which means that each of the 3^n projective measurements is implemented $N = 5N'$ times in total. In summary, we conduct a total of $T = 3^n N$ shots for reconstructing ρ.

To conduct the modified QST algorithm, we first run the conventional QST for a limited number of shots (say 1,000), and identify from these initial runs the matrix elements associated with a value less than some small value, ε. We then remove all measurements associated with those matrix elements. Next, we run the QST process again for a large number of shots to provide a first estimate of ρ. We then further optimize ρ by seeking a solution in the vicinity of our first estimate (a solution with each modified element within some absolute perturbation-value either side of the initial element, the value randomly selected from the range $0 - \varepsilon'$; some elements manually set to satisfy state conditions). Although not formally the optimal solution, we shall see that for many states this provides an adequate QST solution on a NISQ device, in a reduced time-frame relative to full optimization.

We first utilize the conventional QST algorithm to calculate F of the five states, and the experimental results are demonstrated in Fig. A.2 with solid lines (all curves flatten out after a shot number beyond those shown). The error bar shown here is simply a representation of the deviation of the results typically determined from each of the five runs. It is included simply for informative purposes, and should not be considered to

[2]In this appendix, we redefine N, N', and T as different positive integers, representing the repetitions of a single projective measurement.

[3]We refer to one single projective measurement as one "shot."

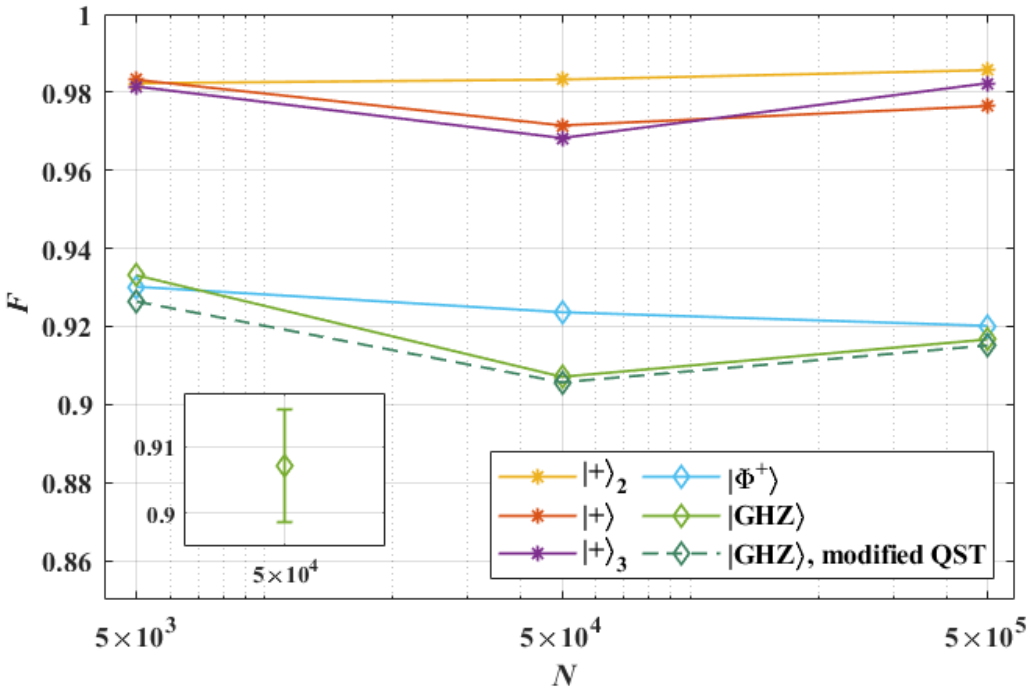

Figure A.2: F as a function of N. The solid lines are obtained via the conventional QST algorithm. The green-dashed line represents F for $|\text{GHZ}\rangle_3$ obtained by the modified QST algorithm. For the $|\text{GHZ}\rangle_3$ state, the conventional QST algorithm requires 27 projective measurements, each repeated N times. However, the modified QST algorithm involves only 11 projective measurement that is repeated N times.

represent formal error statistics on the F values. For the $|+\rangle$, $|+\rangle_2$, and $|+\rangle_3$ states, the F values are all approximately equal to one, independent of N. The two entangled states, $|\Phi^+\rangle$ and $|\text{GHZ}\rangle_3$, obtain relatively lower F values, approximately 0.9. The green-dashed curve represents F calculated for $|\text{GHZ}\rangle_3$ using our modified QST with $\varepsilon = \varepsilon' = 0.01$. In the modified QST algorithm, all 27 projective measurements are performed $1,000$ times to construct an approximate density matrix. Subsequently, only 11 projective measurements are each performed N times, whereas for the conventional QST algorithm, all 27 projective measurements are each performed N times.

The importance in reducing the shot number arises through the run-time on the NISQ device. For 10^5 shots on a three-qubit state this run-time using the conventional QST was found to be of order 12 minutes. Our modified QST resulted in a savings

in run-time on the NISQ device of approximately a factor two - an excellent trade-off given the small discrepancy in the F values the modified QST provides. We also note our modified QST provides for faster optimization (albeit a process run offline from the NISQ device) due to the use of a good initial guess, which in gradient descent methods leads to a linear convergence rate. Speed up factors of more than 20% can be expected relative to arbitrary initial starting points.

A.2 Entanglement Distillation with State Tomography

We now put QST, as run on our NISQ device, in the context of an application implemented on the device. We believe this shows further context, and illustrates the importance of QST for an actual application. We choose an entanglement distillation protocol to this end - a process that can be considered a form of quantum error correction. Although we know quantum error correction is not feasible on current NISQ devices as shown in Chapters 3 and 4, we still illustrate the important role QST will play when such correction techniques do become feasible. A schematic diagram of the working principle of the entanglement distillation protocol is illustrated in Fig. A.3. Suppose Alice and Bob are two parties separated by a large distance and share two maximum entangled pairs, which are represented by

$$|\Phi^+\rangle_a = |\Phi^+\rangle = \frac{1}{\sqrt{2}}(|0\rangle_{Alice}|0\rangle_{Bob} + |1\rangle_{Alice}|1\rangle_{Bob}), \tag{A.1}$$

where the subscripts *Alice* and *Bob* denote that Alice and Bob hold the corresponding qubit. In practice, the two entangled pairs are noisy, and the purpose of the entanglement distillation protocol is to improve the fidelity of $|\Phi^+\rangle$ by sacrificing $|\Phi^+\rangle_a$.

The distillation protocol requires local operations and classical messaging with a post-selection. The local operations implemented by each party include a CX gate and a Z-basis measurement, and after these operations Alice and Bob send their measurement results to each other via a classical communication channel. If Alice and Bob find

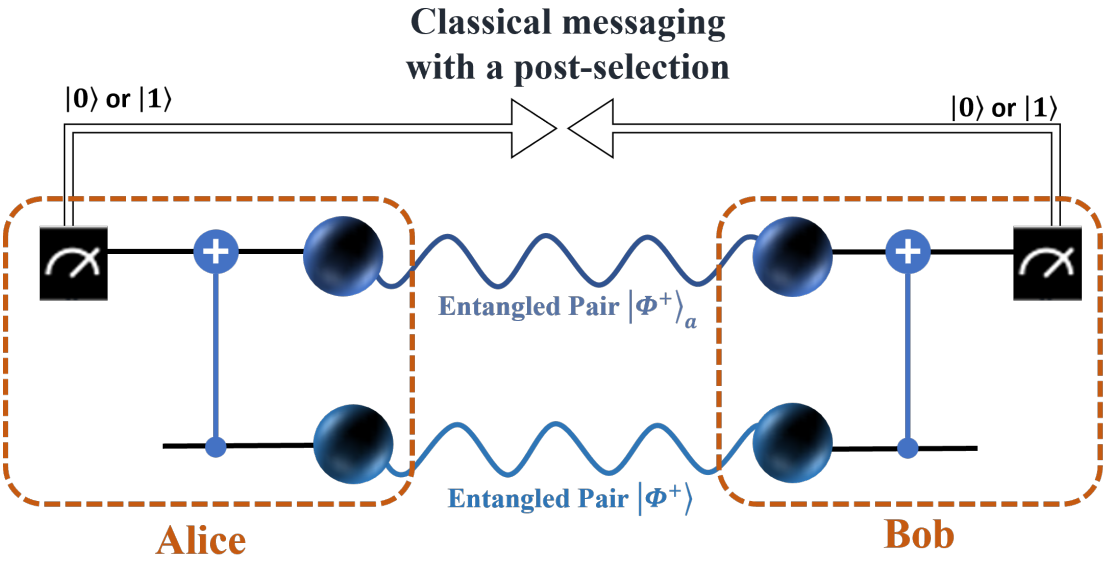

Figure A.3: The entanglement distillation protocol. Alice and Bob share two entangled pairs $|\Phi^+\rangle_a$ and $|\Phi^+\rangle$. The black boxes indicate the Z-basis measurements. The post-selection discards the two entangled pairs if the measurement results differ. If the measurement results are the same, $|\Phi^+\rangle$ will be kept with improved fidelity.

that they have the same measurement result, $|\Phi^+\rangle$ will be kept with improved fidelity. Otherwise, $|\Phi^+\rangle$ is discarded, and the whole protocol needs to be started again.

We apply the conventional QST algorithm to the entanglement distillation protocol, whose quantum circuit is demonstrated in Fig. A.4. The top two qubits shown are prepared as $|\Phi^+\rangle_a$ by a Hadamard gate followed by a CX gate. These two qubits are measured by the Z-basis measurements at the end of the circuit for the classical messaging and post-selection. The last two qubits are prepared as $|\Phi^+\rangle$, and QST is applied to them. Note that the top two qubits (the last two qubits) are physically separated and shared by Alice and Bob. In this protocol we have two performance metrics. One is F again, but this time between $\rho' = |\Phi^+\rangle\langle\Phi^+|$ and ρ, where ρ is the experimental density matrix associated with $|\Phi^+\rangle$ (i.e. the matrix derived from QST). The second metric is the success probability $P = D/T$ of the post-selection, where given T shots ($T = 3^2N$ in this case), D is the number of times the Z-basis measurements

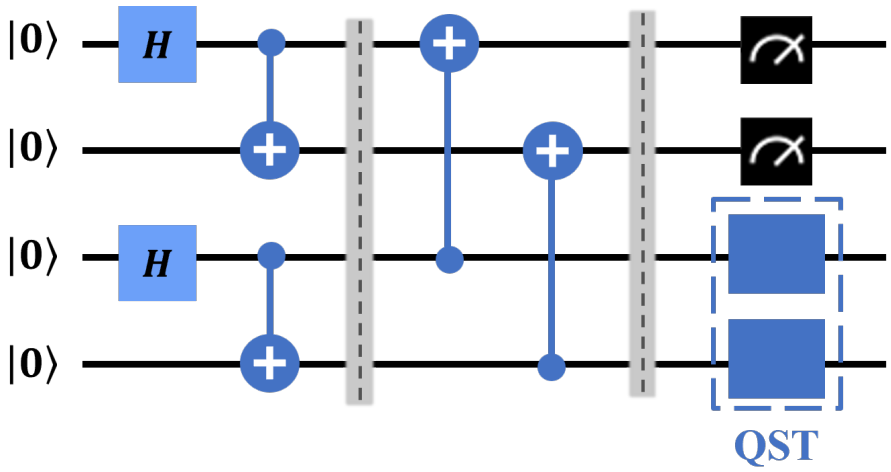

Figure A.4: Quantum circuit of entanglement distillation protocol. The QST is done with local operations and classical communication between Alice and Bob.

mentioned above result in equal values. The shot is only used in the reconstruction of ρ when the Z-basis measurements results are the same (i.e. QST is realized with a shot number less than T).

Our results at running the protocol on the device are shown in Fig. A.5. We caution that the initial fidelity of each entangled pair (with a perfect pair) initialized on the device was 0.92, so the distillation protocol on the device is not working - an outcome consistent with other attempts at full quantum error correction on current NISQ devices. However, the issue we are focused on here is the QST process. Here, we see the importance in determining the matrix ρ via the QST. In the figure it manifests itself in the determination of the fidelity of the "corrected" entangled state (after distillation) with the perfect entangled state. Again, we see the actual improvement does not show up until a large number of shots has occurred (again these curves flatten out after a shot number beyond those shown). The improvement in run-time on the NISQ device and optimization in ρ (offline) for our modified protocol would equally apply to this protocol. As an aside, we compare in Fig. A.5, QST with and without the MEM protocol, showing an improvement in F of order 0.05.

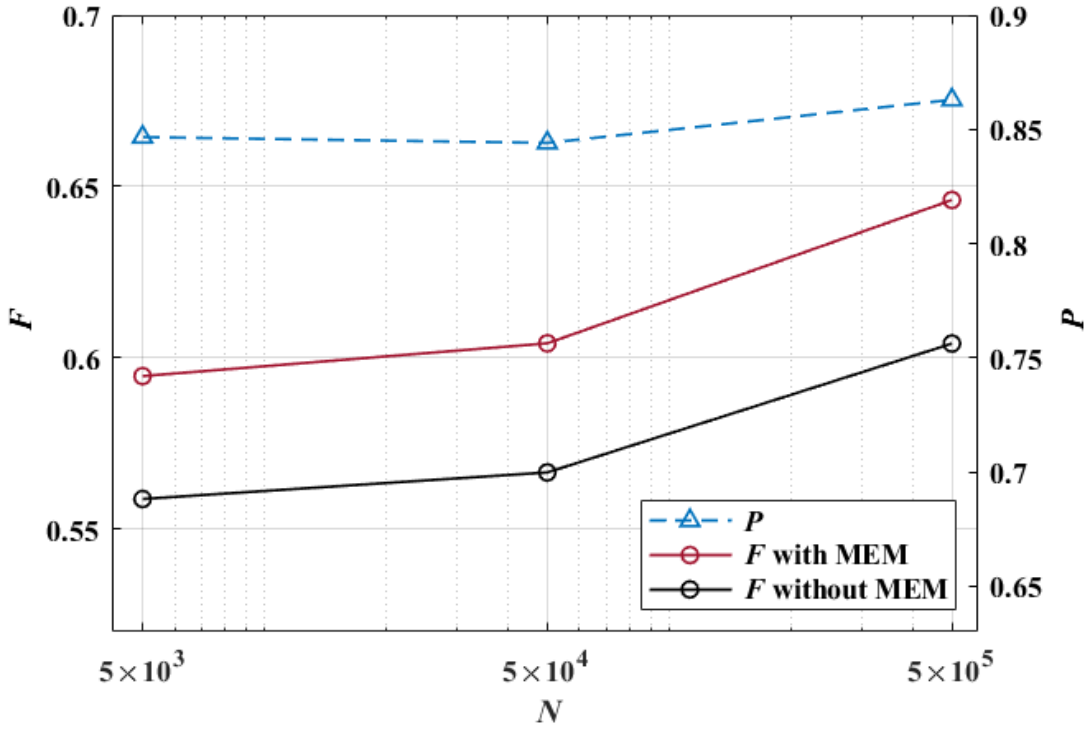

Figure A.5: F and P as a function of N for the entanglement distillation protocol.

A.3 Summary

In this work, we considered QST and its implementation on a 7-qubit superconducting device, *ibmq_jakarta*. The important issue regarding the number of repeated quantum measurements required to construct several states density matrices within some required tolerance was discussed and implemented. Our work highlights the importance of QST, the fact that it can be implemented on real NISQ devices, and that further optimizations that can save run-time on the devices are likely.

Appendix B

Supplementary Materials

B.1 Motivation for Linear Functions in Extrapolated CDR

Consider a global depolarizing channel is applied to σ, which we redefined as the output state of U in this subsection, followed by a measurement of the observable O. This depolarizing channel $\mathcal{E}$ is given by

$$\mathcal{E}(\sigma) = (1-\epsilon)\,\sigma + \epsilon I/d, \tag{B.1}$$

where $d = 2^{n'}$ is the Hilbert-space dimension and ϵ is a parameter that describes the noise, ranging from 0 to 1. In terms of expectation value, the effect of the depolarizing channel leads to

$$\mathrm{Tr}\left[\mathcal{E}(\sigma)O\right] = (1-\epsilon)\,\mathrm{Tr}\left[\sigma O\right] + \epsilon\frac{\mathrm{Tr}[O]}{d}. \tag{B.2}$$

The noisy expectation value of O after executing U is $\langle\tilde{O}\rangle = \mathrm{Tr}\left[\mathcal{E}(\sigma)O\right]$ and the corresponding noiseless expectation value is $\langle O\rangle = \mathrm{Tr}\left[\sigma O\right]$, leading to

$$\langle\tilde{O}\rangle = (1-\epsilon)\,\langle O\rangle + \epsilon\frac{\mathrm{Tr}[O]}{d}. \tag{B.3}$$

The error-mitigated result of eCDR in terms of expectation value is given by

$$\langle \hat{O} \rangle^{ecdr} = a_{\lambda_0} \langle \tilde{O} \rangle + b_{\lambda_0} = \sum_{j=1}^{J} \gamma_j a_{\lambda_j} \langle \tilde{O} \rangle + \sum_{j=1}^{J} \gamma_j b_{\lambda_j}, \tag{B.4}$$

where $\langle \hat{O} \rangle^{ecdr}$ is the eCDR error-mitigated expectation value. To completely mitigate the effect of the global depolarizing channel, *i.e.*, to achieve $\langle \hat{O} \rangle^{ecdr} = \langle O \rangle$, eCDR needs to satisfy

$$a_{\lambda_0} = \sum_{j=1}^{J} \gamma_j a_{\lambda_j} = \frac{1}{1-\epsilon} \quad \text{and} \quad b_{\lambda_0} = \sum_{j=1}^{J} \gamma_j b_{\lambda_j} = -\frac{\epsilon \mathrm{Tr}[O]}{(1-\epsilon)d}. \tag{B.5}$$

Assuming the global depolarizing channel is applied to the original circuit, U, ι times, the output state, σ, then becomes

$$\mathcal{E}^{\iota}(\sigma) = (1-\epsilon)^{\iota} \sigma + [1 - (1-\epsilon)^{\iota}] I/d. \tag{B.6}$$

In terms of expectation value, the above expression can also be expressed as

$$\mathrm{Tr}\left[\mathcal{E}^{\iota}(\sigma) O\right] = (1-\epsilon)^{\iota} \mathrm{Tr}\left[\sigma O\right] + [1 - (1-\epsilon)^{\iota}] \frac{\mathrm{Tr}[O]}{d}, \tag{B.7}$$

which is equivalent to

$$\langle \tilde{O} \rangle = (1-\epsilon)^{\iota} \langle O \rangle + [1 - (1-\epsilon)^{\iota}] \frac{\mathrm{Tr}[O]}{d}. \tag{B.8}$$

Therefore, the eCDR error-mitigated expectation value is given by

$$\langle \hat{O} \rangle^{ecdr} = \sum_{j=1}^{J} \gamma_j \left[a_{\lambda_j} (1-\epsilon)^{\iota} \langle O \rangle + a_{\lambda_j} [1 - (1-\epsilon)^{\iota}] \frac{\mathrm{Tr}[O]}{d} + b_{\lambda_j} \right]. \tag{B.9}$$

We see that $\langle \hat{O} \rangle^{ecdr}$ is equivalent to $\langle O \rangle$ when

$$\begin{aligned} &\sum_{j=1}^{J} \gamma_j a_{\lambda_j} (1-\epsilon)^{\iota} = 1 \quad \text{and} \\ &\sum_{j=1}^{J} \gamma_j \left[a_{\lambda_j} [1 - (1-\epsilon)^{\iota}] \frac{\mathrm{Tr}[O]}{d} + b_{\lambda_j} \right] = 0. \end{aligned} \tag{B.10}$$

Therefore, we can state that eCDR is capable of completely mitigating global depolarizing noise across distinct noise levels. Note that the above analysis is provided based on Refs. [34, 35]. However, our restrictions of the parameters, as shown in Eqs. (B.5) and (B.10), are derived based on the eCDR method.

B.2 Generation of Noisy Estimated Probabilities

In the above, we have simulated P_x^{est} by adding Gaussian noise to the noiseless value obtained from noiseless classical simulations. Other noise models could be considered, such as Gaussian noise with the addition of a bias term and non-Gaussian noise. Clearly, if we could always classically simulate an accurate value for all probabilities we use, there would be no requirement for ZNE (or its variants). We emphasize again that in our calculations, we have assumed P_x^{est} is available from an independent technique. When the error in P_x^{est} approaches zero, our calculation reduce to a study in how a judicious choice of extrapolation function on a per measurement basis can dramatically improve the ZNE method. We offer this algorithm as a means to integrate different mitigation methods with ZNE. This is the main message of the initial part of our study.

We have left open how to find such a reliable P_x^{est} in practice from other methods. A potential method is via the execution of a near-Clifford circuit that is approximately equal to the circuit of interest, U. With fewer non-Clifford gates, the near-Clifford circuit can be executed on the simulator, even when U cannot [35, 167]. The simulation results of the near-Clifford circuit will be regarded as $\{P_x^{est}\}_{x=1}^{2^n}$ and provide guidance for selecting appropriate extrapolation functions.

Another method is CDR (mentioned in the Introduction) - a learning-based error mitigation method using near-Clifford circuits to generate a linear regression model to mitigate errors - an approach that has previously delivered some useful outcomes [34–36, 123]. The linear regression model will be applied to each $P_x^{\lambda_1}$ to obtain P_x^{est}. If CDR can provide a P_x^{est} in practice with reasonable accuracy (*e.g.*, P_x^{est} may not always allow us to select the best extrapolation function but can help eliminate the least effective ones), then the noisy estimator algorithm outlined here can provide for enhanced performance. We suggest this approach as a possible future study not only for QRAM but also for any application running on a NISQ device.

Clearly, many other independent methods can be directly used in our algorithm. It is likely that, when it comes to pragmatic quantum error mitigation, no method will always prevail in providing the optimal outcome. Rather, a combination of different independent algorithms are likely to be of more value.

References

[1] M. Brooks, "Beyond quantum supremacy: The hunt for useful quantum computers," *Nature*, vol. 574, no. 7776, pp. 19–22, 2019.

[2] K. Bharti, A. Cervera-Lierta, T. H. Kyaw, T. Haug, S. Alperin-Lea, A. Anand, M. Degroote, H. Heimonen, J. S. Kottmann, T. Menke *et al.*, "Noisy intermediate-scale quantum algorithms," *Reviews of Modern Physics*, vol. 94, no. 1, 015004, 2022.

[3] W. Lavrijsen, A. Tudor, J. Müller, C. Iancu, and W. de Jong, "Classical optimizers for noisy intermediate-scale quantum devices," in *2020 IEEE International Conference on Quantum Computing and Engineering (QCE)*, 2020, pp. 267–277.

[4] J. Sun, X. Yuan, T. Tsunoda, V. Vedral, S. C. Benjamin, and S. Endo, "Mitigating realistic noise in practical noisy intermediate-scale quantum devices," *Physical Review Applied*, vol. 15, 034026, 2021.

[5] L. Funcke, T. Hartung, K. Jansen, S. Kühn, M. Schneider, P. Stornati, and X. Wang, "Towards quantum simulations in particle physics and beyond on noisy intermediate-scale quantum devices," *Philosophical Transactions of the Royal Society A*, vol. 380, no. 2216, 20210062, 2022.

[6] P. W. Shor, "Scheme for reducing decoherence in quantum computer memory," *Physical Review A*, vol. 52, pp. R2493–R2496, 1995.

[7] N. H. Nguyen, M. Li, A. M. Green, C. Huerta Alderete, Y. Zhu, D. Zhu, K. R. Brown, and N. M. Linke, "Demonstration of Shor encoding on a trapped-ion quantum computer," *Physical Review Applied*, vol. 16, 024057, 2021.

[8] R. Zhang, L.-Z. Liu, Z.-D. Li, Y.-Y. Fei, X.-F. Yin, L. Li, N.-L. Liu, Y. Mao, Y.-A. Chen, and J.-W. Pan, "Loss-tolerant all-photonic quantum repeater with generalized Shor code," *Optica*, vol. 9, no. 2, pp. 152–158, 2022.

[9] E. Knill and R. Laflamme, "Theory of quantum error-correcting codes," *Physical Review A*, vol. 55, pp. 900–911, 1997.

[10] Y. Li and M. P. A. Fisher, "Statistical mechanics of quantum error correcting codes," *Physical Review B*, vol. 103, 104306, 2021.

[11] K. Guenda, S. Jitman, and T. A. Gulliver, "Constructions of good entanglement-assisted quantum error correcting codes," *Designs, Codes and Cryptography*, vol. 86, pp. 121–136, 2018.

[12] J. P. Bonilla Ataides, D. K. Tuckett, S. D. Bartlett, S. T. Flammia, and B. J. Brown, "The XZZX surface code," *Nature Communications*, vol. 12, no. 1, 2172, 2021.

[13] A. G. Fowler, D. S. Wang, C. D. Hill, T. D. Ladd, R. Van Meter, and L. C. L. Hollenberg, "Surface code quantum communication," *Physical Review Letters*, vol. 104, 180503, 2010.

[14] A. G. Fowler, M. Mariantoni, J. M. Martinis, and A. N. Cleland, "Surface codes: Towards practical large-scale quantum computation," *Physical Review A*, vol. 86, 032324, 2012.

[15] A. deMarti iOlius, P. Fuentes, R. Orús, P. M. Crespo, and J. Etxezarreta Martinez, "Decoding algorithms for surface codes," *Quantum*, vol. 8, 1498, 2024.

[16] S. Brandhofer, S. Devitt, T. Wellens, and I. Polian, "Special session: Noisy Intermediate-Scale Quantum (NISQ) computers—How they work, how they fail,

how to test them?" in *2021 IEEE 39th VLSI Test Symposium (VTS)*, 2021, pp. 1–10.

[17] M. Beisel, J. Barzen, F. Leymann, F. Truger, B. Weder, and V. Yussupov, "Configurable readout error mitigation in quantum workflows," *Electronics*, vol. 11, no. 19, 2983, 2022.

[18] D. Qin, X. Xu, and Y. Li, "An overview of quantum error mitigation formulas," *Chinese Physics B*, vol. 31, no. 9, 090306, 2022.

[19] A. Kandala, K. Temme, A. D. Córcoles, A. Mezzacapo, J. M. Chow, and J. M. Gambetta, "Error mitigation extends the computational reach of a noisy quantum processor," *Nature*, vol. 567, no. 7749, pp. 491–495, 2019.

[20] R. Takagi, S. Endo, S. Minagawa, and M. Gu, "Fundamental limits of quantum error mitigation," *NPJ Quantum Information*, vol. 8, no. 1, 114, 2022.

[21] Z. Cai, R. Babbush, S. C. Benjamin, S. Endo, W. J. Huggins, Y. Li, J. R. McClean, and T. E. O'Brien, "Quantum error mitigation," *Reviews of Modern Physics*, vol. 95, no. 4, 045005, 2023.

[22] Y. Suzuki, S. Endo, K. Fujii, and Y. Tokunaga, "Quantum error mitigation as a universal error reduction technique: Applications from the NISQ to the fault-tolerant quantum computing eras," *PRX Quantum*, vol. 3, 010345, 2022.

[23] Z. Cai, "Quantum error mitigation using symmetry expansion," *Quantum*, vol. 5, 548, 2021.

[24] R. Takagi, H. Tajima, and M. Gu, "Universal sampling lower bounds for quantum error mitigation," *Physical Review Letters*, vol. 131, 210602, 2023.

[25] B. McDonough, A. Mari, N. Shammah, N. T. Stemen, M. Wahl, W. J. Zeng, and P. P. Orth, "Automated quantum error mitigation based on probabilistic error reduction," in *2022 IEEE/ACM Third International Workshop on Quantum Computing Software (QCS)*, 2022, pp. 83–93.

[26] A. Seif, Z.-P. Cian, S. Zhou, S. Chen, and L. Jiang, "Shadow distillation: Quantum error mitigation with classical shadows for near-term quantum processors," *PRX Quantum*, vol. 4, 010303, 2023.

[27] M. S. J. Tepaske and D. J. Luitz, "Compressed quantum error mitigation," *Physical Review B*, vol. 107, L201114, 2023.

[28] K. Temme, S. Bravyi, and J. M. Gambetta, "Error mitigation for short-depth quantum circuits," *Physical Review Letters*, vol. 119, 180509, 2017.

[29] S. McArdle, X. Yuan, and S. Benjamin, "Error-mitigated digital quantum simulation," *Physical Review Letters*, vol. 122, 180501, 2019.

[30] S. Endo, S. C. Benjamin, and Y. Li, "Practical quantum error mitigation for near-future applications," *Physical Review X*, vol. 8, 031027, 2018.

[31] T. Giurgica-Tiron, Y. Hindy, R. LaRose, A. Mari, and W. J. Zeng, "Digital zero noise extrapolation for quantum error mitigation," in *2020 IEEE International Conference on Quantum Computing and Engineering (QCE)*, 2020, pp. 306–316.

[32] A. He, B. Nachman, W. A. de Jong, and C. W. Bauer, "Zero-noise extrapolation for quantum-gate error mitigation with identity insertions," *Physical Review A*, vol. 102, 012426, 2020.

[33] A. Mari, N. Shammah, and W. J. Zeng, "Extending quantum probabilistic error cancellation by noise scaling," *Physical Review A*, vol. 104, 052607, 2021.

[34] P. Czarnik, A. Arrasmith, P. J. Coles, and L. Cincio, "Error mitigation with Clifford quantum-circuit data," *Quantum*, vol. 5, 592, 2021.

[35] A. Lowe, M. H. Gordon, P. Czarnik, A. Arrasmith, P. J. Coles, and L. Cincio, "Unified approach to data-driven quantum error mitigation," *Physical Review Research*, vol. 3, 033098, 2021.

[36] J. Pérez-Guijarro, A. Pagès-Zamora, and J. R. Fonollosa, "Extension of Clifford data regression methods for quantum error mitigation," in *2024 IEEE International Conference on Acoustics, Speech and Signal Processing (ICASSP)*, 2024, pp. 9691–9695.

[37] P. D. Nation, H. Kang, N. Sundaresan, and J. M. Gambetta, "Scalable mitigation of measurement errors on quantum computers," *PRX Quantum*, vol. 2, 040326, 2021.

[38] S. Bravyi, S. Sheldon, A. Kandala, D. C. Mckay, and J. M. Gambetta, "Mitigating measurement errors in multiqubit experiments," *Physical Review A*, vol. 103, 042605, 2021.

[39] M. R. Geller, "Conditionally rigorous mitigation of multiqubit measurement errors," *Physical Review Letters*, vol. 127, 090502, 2021.

[40] R. Hicks, B. Kobrin, C. W. Bauer, and B. Nachman, "Active readout-error mitigation," *Physical Review A*, vol. 105, 012419, 2022.

[41] P. Turk and A. Ozaki, "Learning zero noise extrapolation for deterministic quantum circuits," in *2022 IEEE International Conference on Quantum Computing and Engineering (QCE)*, 2022, pp. 265–274.

[42] R. Majumdar, P. Rivero, F. Metz, A. Hasan, and D. S. Wang, "Best practices for quantum error mitigation with digital zero-noise extrapolation," in *2023 IEEE International Conference on Quantum Computing and Engineering (QCE)*, vol. 01, 2023, pp. 881–887.

[43] E. Van Den Berg, Z. K. Minev, A. Kandala, and K. Temme, "Probabilistic error cancellation with sparse Pauli - Lindblad models on noisy quantum processors," *Nature Physics*, vol. 19, no. 8, pp. 1116–1121, 2023.

[44] H.-L. Huang, D. Wu, D. Fan, and X. Zhu, "Superconducting quantum computing: A review," *Science China Information Sciences*, vol. 63, no. 8, 180501, 2020.

[45] M. Kjaergaard, M. E. Schwartz, J. Braumüller, P. Krantz, J. I.-J. Wang, S. Gustavsson, and W. D. Oliver, "Superconducting qubits: Current state of play," *Annual Review of Condensed Matter Physics*, vol. 11, no. 1, pp. 369–395, 2020.

[46] I. Siddiqi, "Engineering high-coherence superconducting qubits," *Nature Reviews Materials*, vol. 6, no. 10, pp. 875–891, 2021.

[47] X. Mi, M. Sonner, M. Y. Niu, K. W. Lee, B. Foxen, R. Acharya, I. Aleiner, T. I. Andersen, F. Arute, K. Arya, A. Asfaw, J. Atalaya, J. C. Bardin, J. Basso, A. Bengtsson, G. Bortoli, A. Bourassa, L. Brill, M. Broughton, B. B. Buckley, D. A. Buell, B. Burkett, N. Bushnell, Z. Chen, B. Chiaro, R. Collins, P. Conner, W. Courtney, A. L. Crook, D. M. Debroy, S. Demura, A. Dunsworth, D. Eppens, C. Erickson, L. Faoro, E. Farhi, R. Fatemi, L. Flores, E. Forati, A. G. Fowler, W. Giang, C. Gidney, D. Gilboa, M. Giustina, A. G. Dau, J. A. Gross, S. Habegger, M. P. Harrigan, M. Hoffmann, S. Hong, T. Huang, A. Huff, W. J. Huggins, L. B. Ioffe, S. V. Isakov, J. Iveland, E. Jeffrey, Z. Jiang, C. Jones, D. Kafri, K. Kechedzhi, T. Khattar, S. Kim, A. Y. Kitaev, P. V. Klimov, A. R. Klots, A. N. Korotkov, F. Kostritsa, J. M. Kreikebaum, D. Landhuis, P. Laptev, K.-M. Lau, J. Lee, L. Laws, W. Liu, A. Locharla, O. Martin, J. R. McClean, M. McEwen, B. M. Costa, K. C. Miao, M. Mohseni, S. Montazeri, A. Morvan, E. Mount, W. Mruczkiewicz, O. Naaman, M. Neeley, C. Neill, M. Newman, T. E. O'Brien, A. Opremcak, A. Petukhov, R. Potter, C. Quintana, N. C. Rubin, N. Saei, D. Sank, K. Sankaragomathi, K. J. Satzinger, C. Schuster, M. J. Shearn, V. Shvarts, D. Strain, Y. Su, M. Szalay, G. Vidal, B. Villalonga, C. Vollgraff-Heidweiller, T. White, Z. Yao, P. Yeh, J. Yoo, A. Zalcman, Y. Zhang, N. Zhu, H. Neven, D. Bacon, J. Hilton, E. Lucero, R. Babbush, S. Boixo, A. Megrant, Y. Chen, J. Kelly, V. Smelyanskiy, D. A. Abanin, and P. Roushan, "Noise-resilient edge modes on a chain of superconducting qubits," *Science*, vol. 378, no. 6621, pp. 785–790, 2022.

[48] C. D. Bruzewicz, J. Chiaverini, R. McConnell, and J. M. Sage, "Trapped-ion quantum computing: Progress and challenges," *Applied Physics Reviews*, vol. 6,

no. 2, 2019.

[49] H. Häffner, C. Roos, and R. Blatt, "Quantum computing with trapped ions," *Physics Reports*, vol. 469, no. 4, pp. 155–203, 2008.

[50] J. T. Barreiro, M. Müller, P. Schindler, D. Nigg, T. Monz, M. Chwalla, M. Hennrich, C. F. Roos, P. Zoller, and R. Blatt, "An open-system quantum simulator with trapped ions," *Nature*, vol. 470, no. 7335, pp. 486–491, 2011.

[51] S. Slussarenko and G. J. Pryde, "Photonic quantum information processing: A concise review," *Applied Physics Reviews*, vol. 6, no. 4, 041303, 2019.

[52] P. Kok, W. J. Munro, K. Nemoto, T. C. Ralph, J. P. Dowling, and G. J. Milburn, "Linear optical quantum computing with photonic qubits," *Reviews of Modern Physics*, vol. 79, pp. 135–174, 2007.

[53] C. Liu, T.-X. Zhu, M.-X. Su, Y.-Z. Ma, Z.-Q. Zhou, C.-F. Li, and G.-C. Guo, "On-demand quantum storage of photonic qubits in an on-chip waveguide," *Physical Review Letters*, vol. 125, 260504, 2020.

[54] L. R. Schreiber and H. Bluhm, "Toward a silicon-based quantum computer," *Science*, vol. 359, no. 6374, pp. 393–394, 2018.

[55] M. Friesen, P. Rugheimer, D. E. Savage, M. G. Lagally, D. W. van der Weide, R. Joynt, and M. A. Eriksson, "Practical design and simulation of silicon-based quantum-dot qubits," *Physical Review B*, vol. 67, 121301, 2003.

[56] A. S. Dzurak, "Silicon-based quantum computing: High-density, high-temperature qubits," in *2021 IEEE International Electron Devices Meeting (IEDM)*, 2021, pp. 14.4.1–14.4.4.

[57] W. J. Gallagher, E. P. Harris, and M. B. Ketchen, "Superconductivity at IBM - a centennial review: Part I - superconducting computer and device applications," in *Proceedings of the IEEE/CSC ESAS European Superconductivity News Forum*, vol. 21, 2012, pp. 1–34.

[58] M. Steffen, D. P. DiVincenzo, J. M. Chow, T. N. Theis, and M. B. Ketchen, "Quantum computing: An IBM perspective," *IBM Journal of Research and Development*, vol. 55, no. 5, pp. 13:1–13:11, 2011.

[59] N. Klco and M. J. Savage, "Minimally entangled state preparation of localized wave functions on quantum computers," *Physical Review A*, vol. 102, 012612, 2020.

[60] N. Klco, E. F. Dumitrescu, A. J. McCaskey, T. D. Morris, R. C. Pooser, M. Sanz, E. Solano, P. Lougovski, and M. J. Savage, "Quantum-classical computation of Schwinger model dynamics using quantum computers," *Physical Review A*, vol. 98, 032331, 2018.

[61] N. Klco, M. J. Savage, and J. R. Stryker, "SU(2) non-abelian gauge field theory in one dimension on digital quantum computers," *Physical Review D*, vol. 101, 074512, 2020.

[62] A. Ciavarella, N. Klco, and M. J. Savage, "Trailhead for quantum simulation of SU(3) Yang-Mills lattice gauge theory in the local multiplet basis," *Physical Review D*, vol. 103, 094501, 2021.

[63] R. C. Farrell, M. Illa, A. N. Ciavarella, and M. J. Savage, "Scalable circuits for preparing ground states on digital quantum computers: The Schwinger model vacuum on 100 qubits," *PRX Quantum*, vol. 5, 020315, 2024.

[64] ——, "Quantum simulations of hadron dynamics in the Schwinger model using 112 qubits," *Physical Review D*, vol. 109, 114510, 2024.

[65] E. F. Dumitrescu, A. J. McCaskey, G. Hagen, G. R. Jansen, T. D. Morris, T. Papenbrock, R. C. Pooser, D. J. Dean, and P. Lougovski, "Cloud quantum computing of an atomic nucleus," *Physical Review Letters*, vol. 120, 210501, 2018.

[66] (2024, Nov.) IBM Quantum. [Online]. Available: https://quantum.ibm.com/

[67] A. Javadi-Abhari, M. Treinish, K. Krsulich, C. J. Wood, J. Lishman, J. Gacon, S. Martiel, P. D. Nation, L. S. Bishop, A. W. Cross, B. R. Johnson, and J. M. Gambetta, "Quantum computing with Qiskit," *arXiv:2405.08810*, 2024.

[68] D. Gross, Y.-K. Liu, S. T. Flammia, S. Becker, and J. Eisert, "Quantum state tomography via compressed sensing," *Physical Review Letters*, vol. 105, 150401, 2010.

[69] J. B. Altepeter, E. R. Jeffrey, and P. G. Kwiat, "Photonic state tomography," *Advances in Atomic, Molecular, and Optical Physics*, vol. 52, pp. 105–159, 2005.

[70] A. Acharya, T. Kypraios, and M. Guţă, "Statistically efficient tomography of low rank states with incomplete measurements," *New Journal of Physics*, vol. 18, no. 4, 043018, 2016.

[71] K. Lemr, K. Bartkiewicz, A. Černoch, and J. Soubusta, "Resource-efficient linear-optical quantum router," *Physical Review A*, vol. 87, 062333, 2013.

[72] W. Kozlowski and S. Wehner, "Towards large-scale quantum networks," in *Proceedings of the Sixth Annual ACM International Conference on Nanoscale Computing and Communication*. Association for Computing Machinery, 2019.

[73] K. Bartkiewicz, A. Černoch, and K. Lemr, "Implementation of an efficient linear-optical quantum router," *Scientific Reports*, vol. 8, no. 1, 13480, 2018.

[74] B. K. Behera, T. Reza, A. Gupta, and P. K. Panigrahi, "Designing quantum router in IBM quantum computer," *Quantum Information Processing*, vol. 18, pp. 1–13, 2019.

[75] V. Bužek and M. Hillery, "Quantum copying: Beyond the no-cloning theorem," *Physical Review A*, vol. 54, pp. 1844–1852, 1996.

[76] X. Yuan, J.-J. Ma, P.-Y. Hou, X.-Y. Chang, C. Zu, and L.-M. Duan, "Experimental demonstration of a quantum router," *Scientific Reports*, vol. 5, no. 1, 12452, 2015.

[77] J. Li, M. Wang, K. Xue, R. Li, N. Yu, Q. Sun, and J. Lu, "Fidelity-guaranteed entanglement routing in quantum networks," *IEEE Transactions on Communications*, vol. 70, no. 10, pp. 6748–6763, 2022.

[78] M. Pant, H. Krovi, D. Towsley, L. Tassiulas, L. Jiang, P. Basu, D. Englund, and S. Guha, "Routing entanglement in the quantum internet," *NPJ Quantum Information*, vol. 5, no. 1, 25, 2019.

[79] V. Giovannetti, S. Lloyd, and L. Maccone, "Quantum random access memory," *Physical Review Letters*, vol. 100, 160501, 2008.

[80] K. Phalak, A. Chatterjee, and S. Ghosh, "Quantum random access memory for dummies," *Sensors*, vol. 23, no. 17, 7462, 2023.

[81] V. Giovannetti, S. Lloyd, and L. Maccone, "Architectures for a quantum random access memory," *Physical Review A*, vol. 78, 052310, 2008.

[82] C. T. Hann, G. Lee, S. Girvin, and L. Jiang, "Resilience of quantum random access memory to generic noise," *PRX Quantum*, vol. 2, 020311, 2021.

[83] M. Zidan, A.-H. Abdel-Aty, A. Khalil, M. Abdel-Aty, and H. Eleuch, "A novel efficient quantum random access memory," *IEEE Access*, vol. 9, pp. 151 775–151 780, 2021.

[84] C. T. Hann, C.-L. Zou, Y. Zhang, Y. Chu, R. J. Schoelkopf, S. M. Girvin, and L. Jiang, "Hardware-efficient quantum random access memory with hybrid quantum acoustic systems," *Physical Review Letters*, vol. 123, 250501, 2019.

[85] S. Zhou, T. Loke, J. A. Izaac, and J. Wang, "Quantum Fourier transform in computational basis," *Quantum Information Processing*, vol. 16, no. 3, 82, 2017.

[86] P. Shor, "Algorithms for quantum computation: Discrete logarithms and factoring," in *Proceedings 35th Annual Symposium on Foundations of Computer Science*, 1994, pp. 124–134.

[87] R. Schützhold, "Pattern recognition on a quantum computer," *Physical Review A*, vol. 67, 062311, 2003.

[88] L. K. Grover, "A fast quantum mechanical algorithm for database search," in *Proceedings of the Twenty-Eighth Annual ACM Symposium on Theory of Computing*. New York, NY, USA: Association for Computing Machinery, 1996, p. 212–219.

[89] M. A. Khan, M. N. Aman, and B. Sikdar, "Beyond bits: A review of quantum embedding techniques for efficient information processing," *IEEE Access*, 2024.

[90] E. Moreno-Pineda, D. O. T. A. Martins, and F. Tuna, "Molecules as qubits, qudits and quantum gates," in *Electron Paramagnetic Resonance: Volume 27*. The Royal Society of Chemistry, 2020.

[91] J. S. Bell, "On the Einstein Podolsky Rosen paradox," *Physics Physique Fizika*, vol. 1, pp. 195–200, 1964.

[92] S. Ghosh, G. Kar, A. Roy, A. Sen(De), and U. Sen, "Distinguishability of bell states," *Physical Review Letters*, vol. 87, 277902, 2001.

[93] N. Gisin and H. Bechmann-Pasquinucci, "Bell inequality, bell states and maximally entangled states for n qubits," *Physics Letters A*, vol. 246, no. 1, pp. 1–6, 1998.

[94] D. M. Greenberger, M. A. Horne, A. Shimony, and A. Zeilinger, "Bell's theorem without inequalities," *American Journal of Physics*, vol. 58, no. 12, pp. 1131–1143, 1990.

[95] P. W. Shor and J. Preskill, "Simple proof of security of the BB84 quantum key distribution protocol," *Physical Review Letters*, vol. 85, pp. 441–444, 2000.

[96] J. Barrett, L. Hardy, and A. Kent, "No signaling and quantum key distribution," *Physical Review Letters*, vol. 95, 010503, 2005.

[97] K. Mattle, H. Weinfurter, P. G. Kwiat, and A. Zeilinger, "Dense coding in experimental quantum communication," *Physical Review Letters*, vol. 76, pp. 4656–4659, 1996.

[98] Y. Guo, B.-H. Liu, C.-F. Li, and G.-C. Guo, "Advances in quantum dense coding," *Advanced Quantum Technologies*, vol. 2, 1900011, 2019.

[99] D. Bouwmeester, J.-W. Pan, K. Mattle, M. Eibl, H. Weinfurter, and A. Zeilinger, "Experimental quantum teleportation," *Nature*, vol. 390, no. 6660, pp. 575–579, 1997.

[100] S. Pirandola, J. Eisert, C. Weedbrook, A. Furusawa, and S. L. Braunstein, "Advances in quantum teleportation," *Nature photonics*, vol. 9, no. 10, pp. 641–652, 2015.

[101] M. A. Nielsen and I. L. Chuang, *Quantum computation and quantum information*. Cambridge university press Cambridge, 2001, vol. 2.

[102] M. Cramer, M. Plenio, S. Flammia, R. Somma, D. Gross, S. Bartlett, O. Landon-Cardinal, D. Poulin, and Y. Liu, "Efficient quantum state tomography," *Nature Communications*, vol. 1, no. 1, 149, 2010.

[103] O. Ezratty, "Perspective on superconducting qubit quantum computing," *The European Physical Journal A*, vol. 59, no. 5, 94, 2023.

[104] L. N. Cooper, "Bound electron pairs in a degenerate Fermi gas," *Physical Review*, vol. 104, no. 4, 1189, 1956.

[105] J. Koch, T. M. Yu, J. Gambetta, A. A. Houck, D. I. Schuster, J. Majer, A. Blais, M. H. Devoret, S. M. Girvin, and R. J. Schoelkopf, "Charge-insensitive qubit design derived from the Cooper pair box," *Physical Review A*, vol. 76, 042319, 2007.

[106] J. M. Kreikebaum, K. P. O'Brien, A. Morvan, and I. Siddiqi, "Improving wafer-scale Josephson junction resistance variation in superconducting quantum coherent circuits," *Superconductor Science and Technology*, vol. 33, no. 6, 06LT02, 2020.

[107] (2024, Nov.) Introduction to transpilation. [Online]. Available: https://docs.quantum.ibm.com/guides/transpile

[108] (2024, Nov.) Transpiler. [Online]. Available: https://qiskit.org/documentation/apidoc/transpiler.html

[109] S. J. Devitt, W. J. Munro, and K. Nemoto, "Quantum error correction for beginners," *Reports on Progress in Physics*, vol. 76, no. 7, 076001, 2013.

[110] W. K. Wootters and W. H. Zurek, "A single quantum cannot be cloned," *Nature*, vol. 299, no. 5886, pp. 802–803, 1982.

[111] M. D. Reed, L. DiCarlo, S. E. Nigg, L. Sun, L. Frunzio, S. M. Girvin, and R. J. Schoelkopf, "Realization of three-qubit quantum error correction with superconducting circuits," *Nature*, vol. 482, no. 7385, pp. 382–385, 2012.

[112] J. M. Günther, F. Tacchino, J. R. Wootton, I. Tavernelli, and P. K. Barkoutsos, "Improving readout in quantum simulations with repetition codes," *Quantum Science and Technology*, vol. 7, 015009, no. 1, 2021.

[113] L. Tornberg, M. Wallquist, G. Johansson, V. S. Shumeiko, and G. Wendin, "Implementation of the three-qubit phase-flip error correction code with superconducting qubits," *Physical Review B*, vol. 77, 214528, 2008.

[114] I. Sohn, S. Tarucha, and B.-S. Choi, "Analysis of physical requirements for simple three-qubit and nine-qubit quantum error correction on quantum-dot and superconductor qubits," *Physical Review A*, vol. 95, 012306, 2017.

[115] J. Roffe, "Quantum error correction: An introductory guide," *Contemporary Physics*, vol. 60, no. 3, pp. 226–245, 2019.

[116] K. Li, V. Chaudhary, and K. R. Chowdhury, "Bip: Bit-phase-flip error mitigation in quantum communications," in *ICC 2023 - IEEE International Conference on Communications*, 2023, pp. 4182–4187.

[117] Z. Chen, K. J. Satzinger, J. Atalaya, A. N. Korotkov, A. Dunsworth, D. Sank, C. Quintana, M. McEwen, R. Barends, P. V. Klimov, S. Hong, C. Jones,

A. Petukhov, D. Kafri, S. Demura, B. Burkett, C. Gidney, A. G. Fowler, A. Paler, H. Putterman, I. Aleiner, F. Arute, K. Arya, R. Babbush, J. C. Bardin, A. Bengtsson, A. Bourassa, M. Broughton, B. B. Buckley, D. A. Buell, N. Bushnell, B. Chiaro, R. Collins, W. Courtney, A. R. Derk, D. Eppens, C. Erickson, E. Farhi, B. Foxen, M. Giustina, A. Greene, J. A. Gross, M. P. Harrigan, S. D. Harrington, J. Hilton, A. Ho, T. Huang, W. J. Huggins, L. B. Ioffe, S. V. Isakov, E. Jeffrey, Z. Jiang, K. Kechedzhi, S. Kim, A. Kitaev, F. Kostritsa, D. Landhuis, P. Laptev, E. Lucero, O. Martin, J. R. McClean, T. McCourt, X. Mi, K. C. Miao, M. Mohseni, S. Montazeri, W. Mruczkiewicz, J. Mutus, O. Naaman, M. Neeley, C. Neill, M. Newman, M. Y. Niu, T. E. O'Brien, A. Opremcak, E. Ostby, B. Pató, N. Redd, P. Roushan, N. C. Rubin, V. Shvarts, D. Strain, M. Szalay, M. D. Trevithick, B. Villalonga, T. White, Z. J. Yao, P. Yeh, J. Yoo, A. Zalcman, H. Neven, S. Boixo, V. Smelyanskiy, Y. Chen, A. Megrant, J. Kelly, and G. Q. AI, "Exponential suppression of bit or phase errors with cyclic error correction," *Nature*, vol. 595, no. 7867, pp. 383–387, 2021.

[118] S. Wu, X. Zhang, X. Yu, and F. Gao, "Mitigating bit-flip and phase-flip noise in quantum teleportation by adding ancillary particles," in *2023 International Conference on Data Security and Privacy Protection (DSPP)*, 2023, pp. 121–127.

[119] D. P. DiVincenzo and P. W. Shor, "Fault-tolerant error correction with efficient quantum codes," *Physical Review Letters*, vol. 77, pp. 3260–3263, 1996.

[120] A. Mondal and K. K. Parhi, "Quantum circuits for stabilizer error correcting codes: A tutorial," *IEEE Circuits and Systems Magazine*, vol. 24, no. 1, pp. 33–51, 2024.

[121] C.-H. Wu, Y.-C. Tsai, and H.-L. Tsai, "Quantum circuits for stabilizer codes," in *2005 IEEE International Symposium on Circuits and Systems (ISCAS)*, vol. 3, 2005, pp. 2333–2336.

[122] M. Krebsbach, B. Trauzettel, and A. Calzona, "Optimization of Richardson extrapolation for quantum error mitigation," *Physical Review A*, vol. 106, no. 6, 062436, 2022.

[123] A. Strikis, D. Qin, Y. Chen, S. C. Benjamin, and Y. Li, "Learning-based quantum error mitigation," *PRX Quantum*, vol. 2, no. 4, 040330, 2021.

[124] G. Acampora, M. Grossi, and A. Vitiello, "Genetic algorithms for error mitigation in quantum measurement," in *2021 IEEE Congress on Evolutionary Computation (CEC)*, 2021, pp. 1826–1832.

[125] L. Funcke, T. Hartung, K. Jansen, S. Kühn, P. Stornati, and X. Wang, "Measurement error mitigation in quantum computers through classical bit-flip correction," *Physical Review A*, vol. 105, 062404, 2022.

[126] Qiskit Development Team. (2024, Nov.) Readout mitigation. [Online]. Available: https://qiskit-community.github.io/qiskit-experiments/manuals/measurement/readout_mitigation

[127] A. Jahn and J. Eisert, "Holographic tensor network models and quantum error correction: A topical review," *Quantum Science and Technology*, vol. 6, no. 3, 033002, 2021.

[128] C.-Y. Lu, W.-B. Gao, J. Zhang, X.-Q. Zhou, T. Yang, and J.-W. Pan, "Experimental quantum coding against qubit loss error," *Proceedings of the National Academy of Sciences*, vol. 105, no. 32, pp. 11 050–11 054, 2008.

[129] M. A. Amri, M. O. Scully, and M. S. Zubairy, "Reversing the weak measurement on a qubit," *Journal of Physics B: Atomic, Molecular and Optical Physics*, vol. 44, no. 16, 165509, 2011.

[130] A. S. Fletcher, P. W. Shor, and M. Z. Win, "Channel-adapted quantum error correction for the amplitude damping channel," *IEEE Transactions on Information Theory*, vol. 54, no. 12, pp. 5705–5718, 2008.

[131] M. Grassl, L. Kong, Z. Wei, Z.-Q. Yin, and B. Zeng, "Quantum error-correcting codes for qudit amplitude damping," *IEEE Transactions on Information Theory*, vol. 64, no. 6, pp. 4674–4685, 2018.

[132] M. Gong, X. Yuan, S. Wang, Y. Wu, Y. Zhao, C. Zha, S. Li, Z. Zhang, Q. Zhao, Y. Liu, F. Liang, J. Lin, Y. Xu, H. Deng, H. Rong, H. Lu, S. C. Benjamin, C.-Z. Peng, X. Ma, Y.-A. Chen, X. Zhu, and J.-W. Pan, "Experimental exploration of five-qubit quantum error-correcting code with superconducting qubits," *National Science Review*, vol. 9, no. 1, 2021.

[133] A. Jayashankar and P. Mandayam, "Quantum error correction: Noise-adapted techniques and applications," *Journal of the Indian Institute of Science*, vol. 103, no. 2, pp. 497–512, 2023.

[134] D. Biswas, G. M. Vaidya, and P. Mandayam, "Noise-adapted recovery circuits for quantum error correction," *Physical Review Research*, vol. 6, 043034, 2024.

[135] R. Srikanth and S. Banerjee, "Squeezed generalized amplitude damping channel," *Physical Review A*, vol. 77, 012318, 2008.

[136] A. S. Fletcher, P. W. Shor, and M. Z. Win, "Channel-adapted quantum error correction for the amplitude damping channel," *IEEE Transactions on Information Theory*, vol. 54, no. 12, pp. 5705–5718, 2008.

[137] M. Zhao, T. Ma, and Y. Ma, "Coherence evolution in two-qubit system going through amplitude damping channel," *Science China Physics, Mechanics and Astronomy*, vol. 61, pp. 1–6, 2018.

[138] S. Markmann, C. Reichl, W. Wegscheider, and G. Salis, "Universal nuclear focusing of confined electron spins," *Nature Communications*, vol. 10, no. 1, 1097, 2019.

[139] M. Enríquez, F. Delgado, and K. Życzkowski, "Entanglement of three-qubit random pure states," *Entropy*, vol. 20, no. 10, 745, 2018.

[140] T. Paul, "Quantum computation and quantum information," *Mathematical Structures in Computer Science*, vol. 17, no. 6, p. 1115–1115, 2007.

[141] S. Arunachalam, V. Gheorghiu, T. Jochym-O'Connor, M. Mosca, and P. V. Srinivasan, "On the robustness of bucket brigade quantum RAM," *New Journal of Physics*, vol. 17, no. 12, 123010, 2015.

[142] R. Laflamme, C. Miquel, J. P. Paz, and W. H. Zurek, "Perfect quantum error correcting code," *Physical Review Letters*, vol. 77, pp. 198–201, 1996.

[143] (2024, Nov.) Quantum teleportation. [Online]. Available: https://github.com/qiskit-community/qiskit-community-tutorials/blob/master/Coding_With_Qiskit/ep5_Quantum_Teleportation.ipynb

[144] B. Park and D. Ahn, "Optimizing the number of CNOT gates in one-dimensional nearest-neighbor quantum Fourier transform circuit," *arXiv:2208.14249*, 2022.

[145] D. Ferrari and M. Amoretti, "Efficient and effective quantum compiling for entanglement-based machine learning on IBM Q devices," *International Journal of Quantum Information*, vol. 16, no. 08, 1840006, 2018.

[146] C. H. Bennett, G. Brassard, S. Popescu, B. Schumacher, J. A. Smolin, and W. K. Wootters, "Purification of noisy entanglement and faithful teleportation via noisy channels," *Physical Review Letters*, vol. 76, pp. 722–725, 1996.

[147] C. H. Bennett, D. P. DiVincenzo, J. A. Smolin, and W. K. Wootters, "Mixed-state entanglement and quantum error correction," *Physical Review A*, vol. 54, no. 5, pp. 3824–3851, 1996.

[148] M. Urbanek, B. Nachman, V. R. Pascuzzi, A. He, C. W. Bauer, and W. A. de Jong, "Mitigating depolarizing noise on quantum computers with noise-estimation circuits," *Physical Review Letters*, vol. 127, 270502, 2021.

[149] S. A Rahman, R. Lewis, E. Mendicelli, and S. Powell, "Self-Mitigating Trotter Circuits for SU(2) Lattice Gauge Theory on a Quantum Computer," *Physical Review D*, vol. 106, 074502, 2022.

[150] R. C. Farrell, I. A. Chernyshev, S. J. M. Powell, N. A. Zemlevskiy, M. Illa, and M. J. Savage, "Preparations for quantum simulations of quantum chromodynamics in $1+1$ dimensions. I. Axial gauge," *Physical Review D*, vol. 107, 054512, 2023.

[151] Y. Li and S. C. Benjamin, "Efficient variational quantum simulator incorporating active error minimization," *Physical Review X*, vol. 7, 021050, 2017.

[152] M. C. Tran, K. Sharma, and K. Temme, "Locality and error mitigation of quantum circuits," *arXiv:2303.06496*, 2023.

[153] H. Pashayan, J. J. Wallman, and S. D. Bartlett, "Estimating outcome probabilities of quantum circuits using quasiprobabilities," *Physical Review Letters*, vol. 115, 070501, 2015.

[154] R. Takagi, "Optimal resource cost for error mitigation," *Physical Review Research*, vol. 3, 033178, 2021.

[155] R. LaRose, A. Mari, S. Kaiser, P. J. Karalekas, A. A. Alves, P. Czarnik, M. El Mandouh, M. H. Gordon, Y. Hindy, A. Robertson, P. Thakre, M. Wahl, D. Samuel, R. Mistri, M. Tremblay, N. Gardner, N. T. Stemen, N. Shammah, and W. J. Zeng, "Mitiq: A software package for error mitigation on noisy quantum computers," *Quantum*, vol. 6, 774, 2022.

[156] (2024, Nov.) Configure error mitigation. [Online]. Available: https://docs.quantum.ibm.com/guides/configure-error-mitigation

[157] D. Bultrini, M. H. Gordon, P. Czarnik, A. Arrasmith, M. Cerezo, P. J. Coles, and L. Cincio, "Unifying and benchmarking state-of-the-art quantum error mitigation techniques," *Quantum*, vol. 7, 1034, 2023.

[158] V. R. Pascuzzi, A. He, C. W. Bauer, W. A. de Jong, and B. Nachman, "Computationally efficient zero-noise extrapolation for quantum-gate-error mitigation," *Physical Review A*, vol. 105, 042406, 2022.

[159] T. Kurita, H. Qassim, M. Ishii, H. Oshima, S. Sato, and J. Emerson, "Synergetic quantum error mitigation by randomized compiling and zero-noise extrapolation for the variational quantum eigensolver," *Quantum*, vol. 7, 1184, 2023.

[160] I.-C. Chen, B. Burdick, Y. Yao, P. P. Orth, and T. Iadecola, "Error-mitigated simulation of quantum many-body scars on quantum computers with pulse-level control," *Physical Review Research*, vol. 4, 043027, 2022.

[161] G. J. Hahn, "The hazards of extrapolation in regression analysis," *Journal of Quality Technology*, vol. 9, no. 4, pp. 159–165, 1977.

[162] S. J. Nawaz *et al.*, "Quantum machine learning for 6G communication networks: State-of-the-art and vision for the future," *IEEE Access*, vol. 7, pp. 46 317–46 350, 2019.

[163] S. K. Ranu, A. Prabhakar, and P. Mandayam, "QKD in the NISQ era: Enhancing secure key rates via quantum error correction," *arXiv:2210.05297*, 2022.

[164] J. D. Teoh, P. Winkel, H. K. Babla, B. J. Chapman, J. Claes, S. J. de Graaf, J. W. O. Garmon, W. D. Kalfus, Y. Lu, A. Maiti, K. Sahay, N. Thakur, T. Tsunoda, S. H. Xue, L. Frunzio, S. M. Girvin, S. Puri, and R. J. Schoelkopf, "Dual-rail encoding with superconducting cavities," *Proceedings of the National Academy of Sciences*, vol. 120, no. 41, e2221736120, 2023.

[165] K. Vogel and H. Risken, "Determination of quasiprobability distributions in terms of probability distributions for the rotated quadrature phase," *Physical Review A*, vol. 40, pp. 2847–2849, 1989.

[166] C. H. Bennett, G. Brassard, S. Popescu, B. Schumacher, J. A. Smolin, and W. K. Wootters, "Purification of noisy entanglement and faithful teleportation via noisy channels," *Physical Review Letters*, vol. 76, pp. 722–725, 1996.

[167] K. N. Smith, M. A. Perlin, P. Gokhale, P. Frederick, D. Owusu-Antwi, R. Rines, V. Omole, and F. Chong, "Clifford-based circuit cutting for quantum simulation," in *Proceedings of the 50th Annual International Symposium on Computer Architecture*, 2023, pp. 1–13.